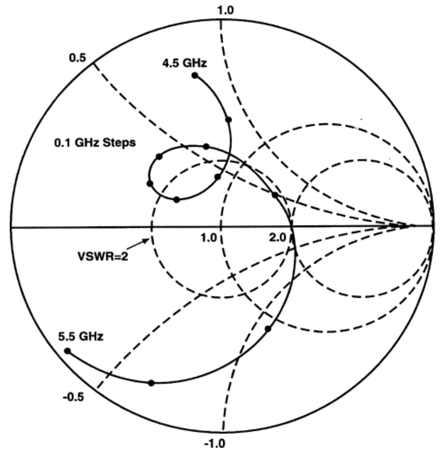

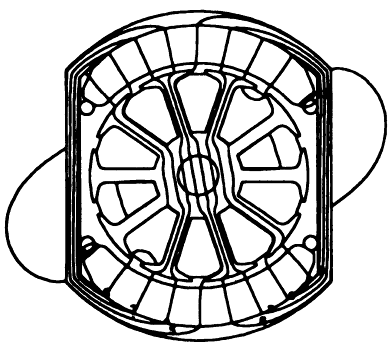

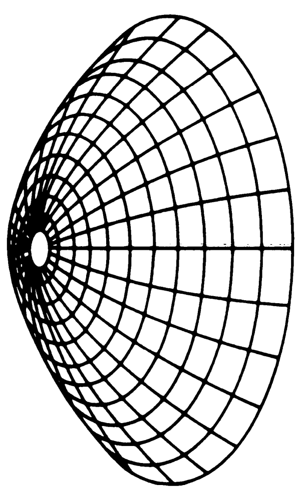

Applied Computational Electromagnetics Society Journal

Editor-in-Chief
Atef Z. Elsherbeni

October 2010
Vol. 25 No. 10
ISSN 1054-4887

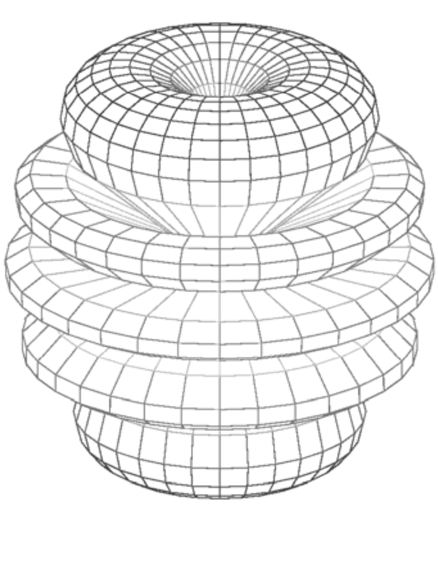

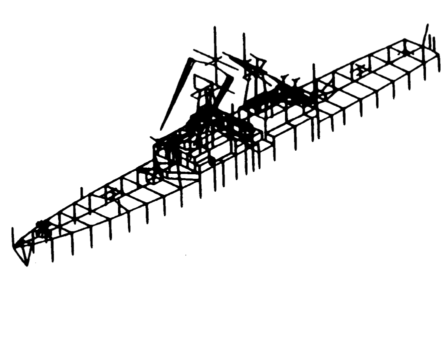

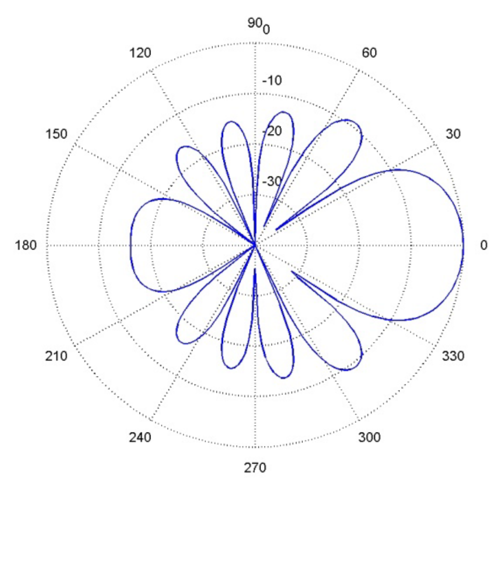

GENERAL PURPOSE AND SCOPE: The Applied Computational Electromagnetics Society ***(ACES)*** Journal hereinafter known as the ***ACES Journal*** is devoted to the exchange of information in computational electromagnetics, to the advancement of the state-of-the art, and the promotion of related technical activities. A primary objective of the information exchange is the elimination of the need to "re-invent the wheel" to solve a previously-solved computational problem in electrical engineering, physics, or related fields of study. The technical activities promoted by this publication include code validation, performance analysis, and input/output standardization; code or technique optimization and error minimization; innovations in solution technique or in data input/output; identification of new applications for electromagnetics modeling codes and techniques; integration of computational electromagnetics techniques with new computer architectures; and correlation of computational parameters with physical mechanisms.

SUBMISSIONS: The ***ACES Journal*** welcomes original, previously unpublished papers, relating to applied computational electromagnetics. Typical papers will represent the computational electromagnetics aspects of research in electrical engineering, physics, or related disciplines. However, papers which represent research in applied computational electromagnetics itself are equally acceptable.

Manuscripts are to be submitted through the upload system of ***ACES*** web site http://aces.ee.olemiss.edu See "Information for Authors" on inside of back cover and at ***ACES*** web site. For additional information contact the Editor-in-Chief:

Dr. Atef Elsherbeni
Department of Electrical Engineering
The University of Mississippi
University, MS 386377 USA
Phone: 662-915-5382 Fax: 662-915-7231
Email: atef@olemiss.edu

SUBSCRIPTIONS: All members of the Applied Computational Electromagnetics Society who have paid their subscription fees are entitled to receive the ***ACES Journal*** with a minimum of three issues per calendar year and are entitled to download any published journal article available at http://aces.ee.olemiss.edu.

Back issues, when available, are $15 each. Subscriptions to ***ACES*** is through the web site. Orders for back issues of the ***ACES Journal*** and changes of addresses should be sent directly to ***ACES***:

Dr. Allen W. Glisson
302 Anderson Hall
Dept. of Electrical Engineering
Fax: 662-915-7231
Email: aglisson@olemiss.edu

Allow four week's advance notice for change of address. Claims for missing issues will not be honored because of insufficient notice or address change or loss in mail unless the Executive Officer is notified within 60 days for USA and Canadian subscribers or 90 days for subscribers in other countries, from the last day of the month of publication. For information regarding reprints of individual papers or other materials, see "Information for Authors".

LIABILITY. Neither ***ACES***, nor the ***ACES Journal*** editors, are responsible for any consequence of misinformation or claims, express or implied, in any published material in an ***ACES Journal*** issue. This also applies to advertising, for which only camera-ready copies are accepted. Authors are responsible for information contained in their papers. If any material submitted for publication includes material which has already been published elsewhere, it is the author's responsibility to obtain written permission to reproduce such material.

APPLIED COMPUTATIONAL ELECTROMAGNETICS SOCIETY JOURNAL

Editor-in-Chief
Atef Z. Elsherbeni

October 2010
Vol. 25 No. 10
ISSN 1054-4887

The ACES Journal is abstracted in INSPEC, in Engineering Index, DTIC, Science Citation Index Expanded, the Research Alert, and to Current Contents/Engineering, Computing & Technology.

The first, fourth, and sixth illustrations on the front cover have been obtained from the Department of Electrical Engineering at the University of Mississippi.

The third and fifth illustrations on the front cover have been obtained from Lawrence Livermore National Laboratory.

The second illustration on the front cover has been obtained from FLUX2D software, CEDRAT S.S. France, MAGSOFT Corporation, New York.

THE APPLIED COMPUTATIONAL ELECTROMAGNETICS SOCIETY

JOURNAL

Vol. 25 No. 10 October 2010

TABLE OF CONTENTS

Design and Full-Wave Analysis of Cavity-Backed Resistively Loaded Circular-End Bow-Tie Antennas for GPR Applications – Part I

Diego Caratelli and Alexander Yarovoy

Delft University of Technology, IRCTR
Mekelweg 4 – 2628 CD Delft, the Netherlands
d.caratelli@tudelft.nl

Abstract – In this paper, the design of cavity-backed bow-tie antennas for ground-penetrating radars is presented. Dielectric embedding and resistive loading of the radiating structure are employed to achieve at least $30:1$ relative bandwidth (55 MHz– >1.5 GHz), with a maximum antenna size of $40\ cm$ and stable antenna performance over different types of the ground. The design procedure is described in detail and provides useful guidelines for the considered class of radiators. Antenna parameters are optimized numerically to combine a large operational bandwidth with reasonably high antenna efficiency. To this end, a full-wave locally conformal finite-difference time domain procedure useful to model electromagnetic structures having complex geometrical and electrical characteristics in the vicinity of the ground is adopted.

Index Terms – Bow-tie antenna, dielectric embedding, ground-penetrating radar, locally conformal finite-difference time-domain modeling, resistive loading.

I. INTRODUCTION

Antennas for ground-penetrating radars (GPR) must meet severe specifications regarding low-frequency operation, broadband characteristics, small volume occupation, and reasonable efficiency for good signal-to-noise ratio of the radar image [1]. Due to increase with frequency of the radio wave attenuation in geophysical media, typical GPR operates at the frequencies below $1\ GHz$. The operational frequency range is determined by the particular application and its relation to the nature of the target, soil constitution, desired depth of penetration, and inversion/classification method being used. For example, a desirable frequency range for detecting subsurface utilities (like water and gas pipes, cables, etc.) is thought to be from $100\ MHz$ to $1\ GHz$ [1]. While low frequencies within this frequency range can be used for subsurface utilities detection via near-field coupling, high frequencies can be used for accurate ranging. For either impulse or stepped-frequency continuous-wave ($SFCW$) radio transmission technique, the adoption of broadband antennas with relative bandwidth above 100% is essential. But, the broadband characteristics must not be obtained at the expense of either the efficiency or the antenna volume. Furthermore, it is required that GPR antennas exhibit stable performance over different types of ground keeping the same wavelet and magnitude of the radiated field. In addition, high isolation between transmit and receive antennas is required to reduce the parasitic mutual coupling. In short, large operational bandwidth at low frequencies, ground invariant performance, high efficiency, small size, and good isolation in an antenna pair, which are sometimes mutually conflicting requirements, are all to be satisfied [2].

As known, cavity-backed spiral and bow-tie antennas might be a suitable choice in GPR applications [3–5]. The spiral antennas possess a large fractional bandwidth. However, their dispersion nature results in an extended time response of the radiated electromagnetic field, and consequently either hardware or software deconvolution of the received radio signal is needed. As spiral antenna performance depends on properties of the ground, such deconvolution often fails to provide good results [1]. Furthermore, reflections from the ends of the arms cause both clutters and degradation of the circularity of the polarization, while the proximity of the ground adversely affects the reactive field of the antenna, resulting in a significant degradation of its characteristics in terms of radiation pattern, and input impedance. The bow-tie antennas, which basically are the limiting case of biconical antennas, are attractive mainly due to their construction simplicity and wideband property [3–4], and they are widely employed in *GPR* applications [1], [8– 13]. Bow ties with circular ends and some resistive loading demonstrate reduced late-time ringing [5–7]. Cavity-backing is used to decrease the back-radiation level in the air region [13]. However, the operational bandwidth of cavity-backed bow ties exceeds rarely $30\% - 40\%$, which is considerably below the desired figure of merit (100%).

In this paper, we have designed a novel *GPR* antenna featuring an extremely large fractional bandwidth (more than 100%), good transient behavior, ground invariant performance, reasonably high bandwidth, electrically small size, low mutual coupling in an antenna pair, and low back radiation. The antenna is designed to be used with *SFCW* radar and targeted antenna specifications are: the operational frequency band, based on the reflection coefficient with respect to $50\ \Omega$ feeding line, from $100\ MHz$ to $1\ GHz$ ($10:1$ relative bandwidth); maximal antenna size of $40\ cm$ by $40\ cm$ by $30\ cm$ (length $\times$ width $\times$ height); coupling between Tx and Rx antennas in the radar system below $-30\ dB$. Neither in literature nor in commercial systems, antennas with similar specifications have been found. For the antenna optimization and performance analysis a dedicated locally conformal finite-difference time-domain (*FDTD*) procedure, useful to accurately analyze electromagnetic structures having complex geometrical and electrical characteristics and to take into account the impact of the ground, is adopted. The design procedure is described thoroughly and provides useful guidelines for the considered class of radiators. Detailed analysis of circuital and radiation properties of the antenna is presented in Part II of this paper.

This paper is organized as follows. The proposed antenna structure is briefly described in Section II. The full-wave *FDTD*-based modeling approach for the electromagnetic characterization of the proposed antenna is discussed in Section III. Finally, Section IV describes the optimization and design guidelines of the antenna.

II. THE PROPOSED ANTENNA STRUCTURE AND DESIGN

The proposed antenna is based on a circular-ended bow tie (see Fig. 1). The initial radiator consists of two circularly-ended flairs, whose electrical conductivity σ_f varies with the radial distance ρ from the feeding delta gap. Dielectric embedding and resistive loading of the radiating structure are used to reduce the flair angle while keeping antenna input impedance at $50\ \Omega$ and compacting the antenna size [5]. To reduce parasitic emission to air, the antenna is cavity-backed. Special cavity filling is suggested in order to keep wideband antenna matching. The loading profile is optimized based on numerical simulations.

To design such an antenna we use the following procedure:

1. determine the dielectric embedding;
2. determine the bow-tie flair angle based on the required antenna impedance;
3. determine the optimal resistive loading.

The first two steps are based on analytic techniques while the last one requires numerical simulations.

A. The absorber-filled cavity

To reduce the antenna back-radiation level, potentially resulting in *EMI*s with nearby electronic equipment, a suitable shielding structure is adopted (see Fig. 1). This in turn is useful to meet the severe restrictions of the allowed transmitted power level usually imposed by local authorities.

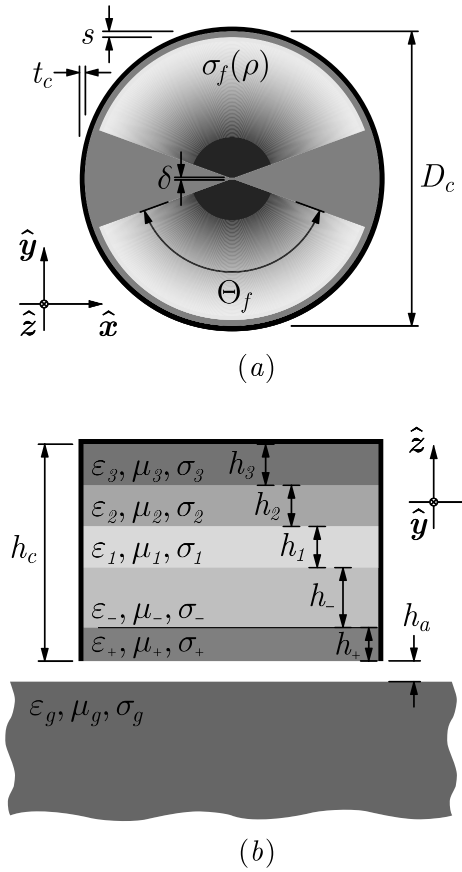

Fig. 1. Bottom (a) and cross-sectional (b) view of the cavity-backed resistively-loaded bow-tie antenna for *GPR* applications. Antenna characteristics: $D_c = 40\ cm$, $s = 1\ cm$, $t_c = 0.5\ cm$, $\Theta_f = 130°$, $\delta = 0.25\ cm$, $h_c = 28.5\ cm$, $h_a = 3\ cm$, $\varepsilon_{r_g} = 6$, $\sigma_g = 0.015\ S/m$, $h_+ = 0.5\ cm$, $\varepsilon_{r_+} = 3$, $\sigma_+ = 0\ S/m$, $h_- = 10\ cm$, $\varepsilon_{r_-} = 10$, $\sigma_- = 0\ S/m$, $h_1 = 6\ cm$, $\varepsilon_{r_1} = 11$, $\sigma_1 = 0.125\ S/m$, $h_2 = 6\ cm$, $\varepsilon_{r_2} = 15$, $\sigma_2 = 0.25\ S/m$, $h_3 = 6\ cm$, $\varepsilon_{r_3} = 20$, $\sigma_3 = 1\ S/m$. The reference system adopted to express the field quantities is shown.

The considered cavity may be regarded as an inhomogeneously filled circular waveguide, terminated on a perfectly conducting wall, where the spatial distribution of the electromagnetic field can be represented as the superposition of an infinite number of modes. The voltage and current relevant to each mode can be conveniently evaluated using the transmission-line formalism [14]. The description of the electromagnetic field within the structure is thereby reduced to the description of the electrical behavior of an infinite set of transmission lines terminated on an ideal short circuit (see Fig. 2). The input impedance of each transmission line can be easily evaluated as

$$Z_- = Z_{c-} \frac{Z_1 \cos k_- h_- + j Z_{c-} \sin k_- h_-}{Z_{c-} \cos k_- h_- + j Z_1 \sin k_- h_-}, \qquad (1)$$

where

$$Z_i = Z_{c_i} \frac{Z_{i+1} \cos k_i h_i + j Z_{c_i} \sin k_i h_i}{Z_{c_i} \cos k_i h_i + j Z_{i+1} \sin k_i h_i}, \qquad (2)$$

for $i = 1, 2, 3$, and $Z_4 = 0$. In (1) and (2) k_-, Z_{c-} and k_i, Z_{c_i} denote the propagation constant and characteristic impedance of the generic mode within the antenna substrate and the $i-$th absorbing layer ($i = 1, 2, 3$), respectively. The thickness and electrical properties of such materials have been determined by imposing, at the central working frequency $f_c = 550\ MHz$, the

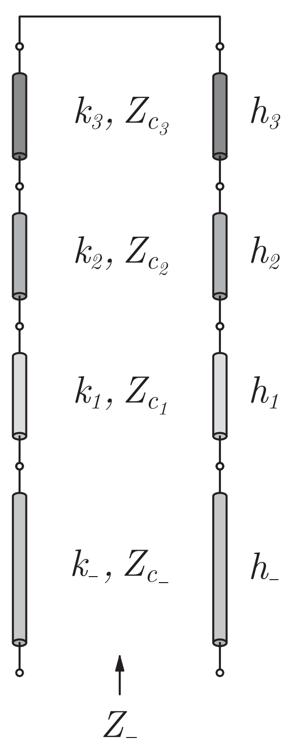

Fig. 2. Transmission-line equivalent circuit of the generic electromagnetic mode propagating in the antenna cavity.

matching condition

$$|\Gamma_-| < 0.05\,, \tag{3}$$

being

$$\Gamma_- = \frac{Z_- - Z_{c_-}}{Z_- - Z_{c_-}} \tag{4}$$

the input reflection coefficient relevant to the transmission-line equivalent circuit relevant to the fundamental mode (TE_{11}) propagating within the cavity. In (3) the manufacturing constraint $\varepsilon_{r_-} \leq 10$ has been also enforced. By doing so, the parameters specified in the caption of Fig. 1 have been obtained. In particular, by selecting the relative permittivity of the superstrate as $\varepsilon_{r_-} = 10$ we set the cut-off frequency of the fundamental mode of the cavity to be equal to about $139\ MHz$. Below such frequency, the cavity essentially behaves like a reactive load for the antenna. It should be pointed out that the absorbing panels to be embedded in the shielding cavity can be realized using suitable filled polymer composites [15–16]. The electrical properties of such materials can be conveniently adjusted by properly setting the volume fraction of the ceramic and ferrite filler.

Finally, the permittivity of the antenna substrate has been selected to be $\varepsilon_{r_+} = 3$ in order to achieve a smooth transition from the antenna feeding line to homogeneous soils with relative dielectric constant $\varepsilon_{r_g} \geq 3$, so minimizing the return-loss level in the operating frequency band.

B. The bow-tie flair angle

A resistively-loaded bow-tie antenna may be regarded as a coplanar fin transmission line, whose characteristic impedance, according to quasi-static theory [17], can be calculated using the relevant static capacitance. A model to evaluate such capacitance by conformal mapping is proposed in [18]. As a result, the above-mentioned characteristic impedance is expressed as follows

$$Z_0 = \frac{\eta_0}{\sqrt{\bar{\varepsilon}_r}} \frac{K(k)}{K(k')}\,, \tag{5}$$

where $K(\cdot)$ is the complete elliptic integral of the first kind [19] with moduli

$$k = \frac{1 - \sin\Theta_f/2}{1 + \sin\Theta_f/2}\,, \tag{6}$$

$$k' = \sqrt{1 - k^2}\,, \tag{7}$$

η_0 denotes the free-space characteristic impedance, and $\bar{\varepsilon}_r = \left(\varepsilon_{r_+} + \varepsilon_{r_-}\right)/2$ is the effective relative permittivity value at the dielectric interface (see Fig. 1), where the antenna flairs are realized. Consequently, by imposing the impedance matching condition $Z_0 = R_g$, the flairs angle Θ_f can be easily determined. So, in order to achieve the input impedance of $50\ \Omega$, we have to select the antenna flair angle of 150°.

III. THE FULL-WAVE ANTENNA MODELING

The analysis and design of complex radiating structures requires accurate electromagnetic field prediction models. One such widely used technique is the finite-difference time-domain ($FDTD$) algorithm. However, in the conventional formulation proposed by Yee [20–21], each cell in the computational grid is implicitly supposed to be filled by a homogeneous material. For this reason, the adoption of Cartesian meshes could result in reduced numerical accuracy when structures having curved boundaries are to be modeled. In this case, the locally conformal $FDTD$ scheme in [22–23] provides clear advantages over the use of the stair-casing approach or unstructured and stretched space lattices, potentially suffering from significant numerical dispersion and/or instability. Such a scheme, necessary to improve the numerical accuracy of the conventional algorithm, is based on the definition of effective material parameters suitable to describe the geometrical and electrical characteristics of complex electromagnetic structures [22]. By using the mentioned subcell method, the design and accurate full-wave analysis of the considered class of ultra-wideband bow-tie antennas have been carried out.

As shown in Fig. 1, the radiating structure is assumed to be elevated to a height $h_a = 3\ cm$ over the ground, modeled as a lossy homogeneous half-space having relative permittivity $\varepsilon_{r_g} = 6$ and electrical conductivity $\sigma_g = 0.015\ S/m$, corresponding to the asphalt. A voltage source of amplitude $V_g = 1\ V$ and internal resistance $R_g = 50\ \Omega$ is employed to excite the structure. The locally conformal *FDTD* characterization of the structure has been performed by making use of a non-uniform computational grid with maximum cell size $\Delta h_{\max} = \lambda_{\min}/16 \simeq 0.5\ cm$, where $\lambda_{\min}$ is the operating wavelength inside the ground at the maximum frequency $f_{\max} = 1.5\ GHz$ in the excitation signal, which is a Gaussian pulse of the form

$$\mathcal{P}(t) = \exp\left[-\left(\frac{t-t_0}{\tau_g}\right)^2\right], \tag{8}$$

where $t_0 = 10\tau_g$, and

$$\tau_g = \frac{\sqrt{\ln 10}}{\pi f_{\max}}. \tag{9}$$

The selection of τ_g according to (9) gives the source pulse significant energy in the frequency band up to $f_{\max}$. The pulse is coupled into the finite-difference equations used to update the electric field distribution within the feeding delta gap. As usual, the antenna input voltage $V_{in}(t)$ and current $I_{in}(t)$ are related to the normalized incident and reflected waves by

$$a(t) = \frac{1}{2}\left[\frac{V_{in}(t)}{\sqrt{Z_0}} + I_{in}(t)\sqrt{Z_0}\right], \tag{10}$$

$$b(t) = \frac{1}{2}\left[\frac{V_{in}(t)}{\sqrt{Z_0}} - I_{in}(t)\sqrt{Z_0}\right]. \tag{11}$$

Therefore, the antenna input reflection coefficient can be easily determined as

$$\Gamma_{in}(f) = \frac{\mathsf{F}[b(t)]}{\mathsf{F}[a(t)]}, \tag{12}$$

where $\mathsf{F}[\cdot]$ denotes the Fourier transform operator.

In all calculations presented in this paper, a ten-cell uniaxial perfectly matched layer (*UPML*) absorbing boundary condition for lossy media [24] has been used at the outer *FDTD* mesh boundary to simulate the extension of the space lattice to infinity. As outlined in [21], the *UPML* is indeed perfectly matched to the inhomogeneous medium formed by the upper air region and the lossy material half space modeling the ground. So, no spurious numerical reflections take place at the air-ground interface. In particular, a quartic polynomial grading of the *UPML* conductivity profile has been selected in order to have a nominal reflection error $R_{PML} \simeq e^{-16}$.

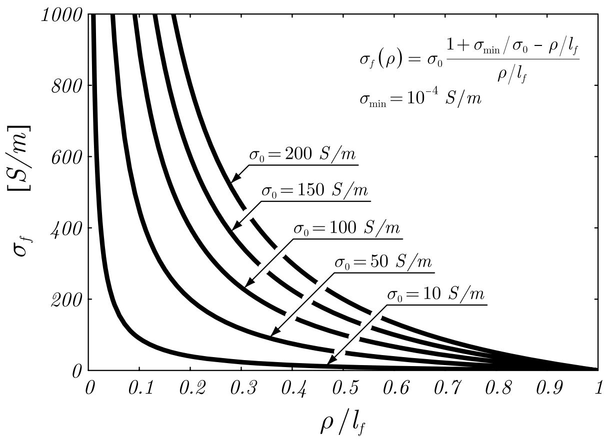

Fig. 3. Resistive loading profile of the cavity-backed circular-end bow-tie antenna flairs.

For the individual antenna elevated above ground, the total *FDTD* mesh dimensions are $282 \times 283 \times 253$ in the x, y, z directions respectively, and the computational time is approximately $1.4\ s$ per step on a workstation provided with a $2.33\ GHz$ Intel Xeon processor.

IV. THE ANTENNA OPTIMIZATION

It is commonly understood that in *GPR* applications for detection of buried objects, it is essential that the probing pulse exhibits reduced late-time *ringing* in order to prevent masking of the targets. Late-time *ringing* is caused mainly by the multiple reflections between the antenna open ends and the feed point, which are responsible for the narrowband behavior of the radiating structure. To properly enlarge the antenna bandwidth (thus reducing the late-time *ringing*), we apply to the flairs of the proposed radiator a resistive loading with distribution

$$\sigma_f(\rho) = \sigma_0 \frac{1 + \sigma_{\min}/\sigma_0 - \rho/l_f}{\rho/l_f}, \tag{13}$$

similar to the ideal *Wu-King* profile (see Fig. 3). In (13), $l_f = D_c/2 - s_c = 19\ cm$ is the flair length, which is determined from the maximal allowed size of the antenna, and $\sigma_{\min} = \sigma_f(l_f)$ is the electrical conductivity value at the antenna end sections. In particular, the considered resistive loading can be easily realized by means of well-established technologies extensively used in printed circuit board (PCB) manufacturing and lithographic processes, such as thick film printing on ceramic, etched printed circuit technology, and screen printed ink technology [25]. Among these, screen printed ink technology appears to be the most robust and flexible. In fact, inks can be mixed to any required resistance within bounds, and the profile can be built up from many layers, thus eliminating the possibility of inter-segment discontinuities.

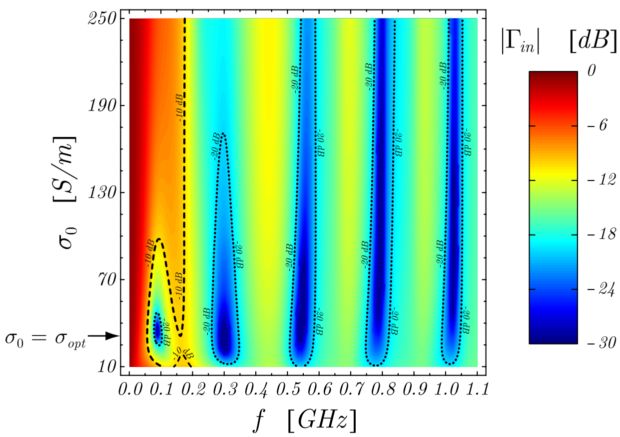

Fig. 4. Frequency behavior of the antenna input reflection coefficient for different loading profiles. The antenna is elevated $3\ cm$ over the ground, modeled as a lossy homogeneous half-space having relative permittivity $\varepsilon_{r_g} = 6$ and electrical conductivity $\sigma_g = 0.015\ S/m$.

A specific parametric analysis has been carried out to determine an optimal value of the parameter σ_0 appearing in (13) which results in achieving the lowest operational frequency, the operational bandwidth above $1\,GHz$, and a reasonably high efficiency (see Fig. 4). The total antenna efficiency is given by

$$e_a(f) = e_r(f)\, e_{in}(f)\ , \tag{14}$$

where

$$e_r(f) = \frac{P_{rad}(f)}{P_{in}(f)}\,, \tag{15}$$

$$e_{in}(f) = 1 - |\Gamma_{in}(f)|^2 \tag{16}$$

are the radiation and input mismatch efficiency terms, respectively. In (15), $P_{in}(f) = \frac{1}{2}\mathrm{Re}\{V_{in}(f)\, I_{in}^*(f)\}$ is the real input power accepted by the antenna, while the total radiated power $P_{rad}(f)$ can be determined by integrating the real part of the Poynting vector over a surface S_a in the air region, enclosing the radiating structure, namely

$$P_{rad}(f) = \frac{1}{2}\mathrm{Re}\left\{\iint_{S_a} \underline{E}(\underline{r}, f) \times \underline{H}^*(\underline{r}, f)\cdot \underline{dS}\right\}. \tag{17}$$

It has been numerically found that the value $\sigma_0 = \sigma_{opt} \simeq 30\ S/m$ provides a good compromise between impedance matching and efficiency. In particular, with the specified resistive loading profile, the antenna exhibits an extremely large operational bandwidth (based on the reflection coefficient) from $55\ MHz$ to at least $1.5\ GHz$. Inspection of Fig. 5 also reveals that $e_a(f)$ assumes reasonably high values ($> 15\%$) in the low-frequency band, but rapidly decreases at higher frequencies because of the

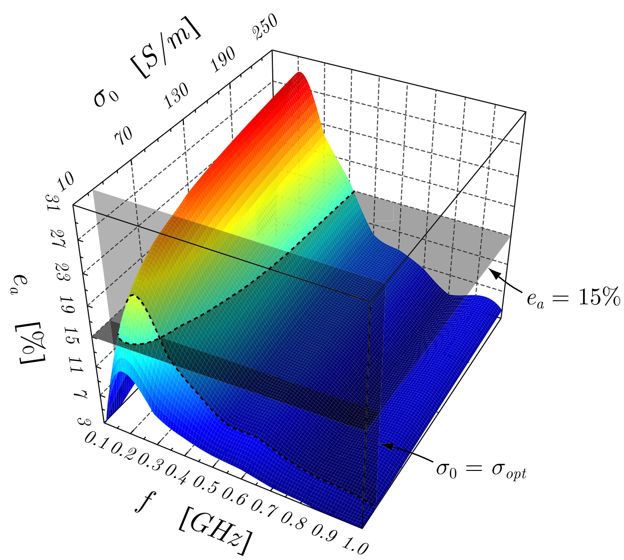

Fig. 5. Frequency behavior of the antenna efficiency for different loading profiles. The antenna is elevated $3\ cm$ over the ground, modeled as a lossy homogeneous half-space having relative permittivity $\varepsilon_{r_g} = 6$ and electrical conductivity $\sigma_g = 0.015\ S/m$.

loading effect of the cavity, and the proximity effect of the ground. In particular, by increasing the conductivity parameter σ_0, the total efficiency becomes larger, since the material forming the antenna flairs tends to behave like a perfect electric conductor, so leading to an overall reduction of the ohmic losses level. Unfortunately, a significant low-frequency degradation of the antenna return-loss occurs for $\sigma_0 \gtrsim \sigma_{opt}$, or $\sigma_0 \lesssim \frac{3}{4}\sigma_{opt}$. From a physical point of view, this means that the radio waves due to the field reflection from the antenna ends, as well as from the air-ground interface and the metallic cavity walls, contain significant energy when returning to the feed point. It's worth noting that a non-flat frequency behavior of the antenna radiation efficiency can be responsible for a spreading of the electromagnetic pulse transmitted by the radiator. However, since the proposed structure is mainly intended for $SFCW$ radar applications, a suitable power equalization technique can be conveniently adopted to guarantee a uniform level of radiated energy [26].

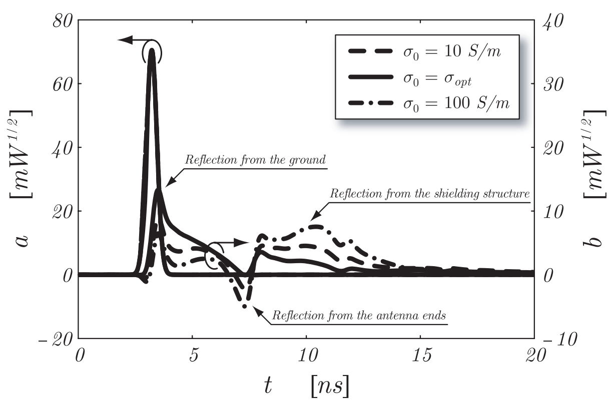

Fig. 6. Time-domain behavior of the normalized incident and reflected waves at the antenna input terminals for different loading profiles. The antenna is elevated $3\ cm$ over the ground, modeled as a lossy homogeneous half-space having relative permittivity $\varepsilon_{r_g} = 6$ and electrical conductivity $\sigma_g = 0.015\ S/m$.

Figure 6 clearly illustrates some key effects of the resistive loading distribution along the antenna flairs. Shown is the time-domain behavior of the normalized waves $a(t)$, $b(t)$ at the input terminals of the radiator. In particular, the peak at $\sim 3.2\ ns$ represents the incident voltage pulse. Those at $\sim 3.5\ ns$, $\sim 7.2\ ns$, and $\sim 10\ ns$ correspond, respectively, to reflections from the ground, the antenna ends, and the shielding structure, which should be minimal for a well-designed GPR system. As it appears, highly conducting loading profiles ($\sigma_0 > \sigma_{opt}$) reduce the reflections from the ground, whereas increasing the resistivity ($\sigma_0 < \frac{3}{4}\sigma_{opt}$) is an effective means to lower reflections from the edges of the antenna panels and the shielding structure. So, the optimal loading distribution ($\sigma_0 = \sigma_{opt}$) represents a trade-off between the above-mentioned operation modes.

V. CONCLUSION

We have designed a cavity-backed loaded bow-tie antenna for ground-penetrating radars. Dielectric embedding and resistive loading of the radiating structure are used to reduce the flair angle and the antenna size, as well as to assure stable antenna performance over different types of the ground. In order to reduce parasitic emission to air, the antenna is cavity-backed. Special cavity filling is suggested in order to keep wideband antenna matching. The antenna exhibits an extremely large operational bandwidth (based on the reflection coefficient) from $55\ MHz$ to at least $1.5\ GHz$, radiation efficiency level comparable with Wu-King dipoles, electrically small size of $40\ cm$ by $40\ cm$ by $29\ cm$ (length $\times$ width $\times$ height). Furthermore (as it is shown in Part II), the antenna has ground invariant performance and mutual coupling below $-30\ dB$ in a pair configuration.

The antenna optimization and circuital performance investigation have been carried out numerically by means of a dedicated full-wave technique based on a locally conformal $FDTD$ scheme, which does not require the stair-case approximation and, thus, ultimatively suits for accurate modeling of structures with cylindrical shape. From the numerical optimization, it has been found that the conductivity value $\sigma_{opt} \simeq 30\ S/m$ results in an optimal resistive loading distribution in terms of the lowest operating frequency, the largest absolute operational bandwidth and reasonable efficiency. For this loading profile, the antenna with maximum size of about $40\ cm$ is matched to the $50\ \Omega$ feeding line starting from the frequency $f_\ell \simeq 55\ MHz$.

At the lowest operational frequency, the normalized volume featured by the antenna is given by $V/\lambda_0^3 \simeq 0.025\%$, being λ_0 the relevant free-space wavelength. Thus, the proposed antenna exhibits a strongly reduced volume occupation. Despite that, it has been numerically demonstrated that the antenna efficiency assumes reasonably high values ($> 15\%$) in the low-frequency band, while it decreases at higher frequencies because of the loading effect of the cavity and the proximity effect of the ground. It should be noticed that the efficiency of a dipole of similar dimensions with the ideal *Wu-King* loading profile in free space is below 15%. Thus, the efficiency of the proposed antenna is comparable with that of an ideal *Wu-King* dipole antenna.

Finally, it has been shown that starting from $f \simeq 200\ MHz$ variations of the loading profile do not cause considerable differences in the antenna efficiency which means that the efficiency is not much affected by the resistive loading of the radiating flairs.

ACKNOWLEDGMENT

This research has been carried out in the framework of *EU*-sponsored project *ORFEUS* (contract number: *FP6-2005-Global-4-036856*). The authors would like to thank anonymous reviewers for their suggestions and comments.

REFERENCES

[1] D. Daniels, *Ground Penetrating Radar*, 2^{nd} ed., IEE Press, 2004.

[2] A. G. Yarovoy and L. P. Ligthart, "Theoretical and experimental analysis of GPR antennas," in *Proc. URSI EMTS International Symposium on Electromagnetic Theory*, Pisa, Italy, vol. 1, pp. 108–110, May 23-27, 2004.

[3] W. L. Stutzman and G. A. Thiele, *Antenna Theory and Design*, 2^{nd} ed., Wiley-Interscience, 1998.

[4] C. A. Balanis, *Antenna Theory: Analysis and Design*, 3^{rd} ed., Wiley-Interscience, 2005.

[5] D. Caratelli, "Design and analysis of antennas for ground penetrating radar applications," Delft University of Technology, the Netherlands, Tech. Rep. IRCTR–S–041–07, Sept. 11, 2007.

[6] D. Caratelli, "Full-wave analysis of cavity-backed resistively loaded bow-tie antennas for GPR applications," Delft University of Technology, the Netherlands, Tech. Rep. IRCTR–S–001–08, Jan. 11, 2008.

[7] D. Caratelli, A. Yarovoy, and L. P. Ligthart, "Full-wave analysis of cavity-backed resistively-loaded bow-tie antennas for GPR applications," *European Microwave Conference 2008*, Amsterdam, the Netherlands, pp. 204-207, October 27-31, 2008.

[8] G. H. Brown and O. M. Woodward Jr., "Experimentally determined radiation characteristics of conical and triangular antennas," *RCA Rev.*, vol. 13, pp. 425–452, Dec. 1952.

[9] K. L. Shlager, G. S. Smith, and J. G. Maloney, "Optimization of bow-tie antennas for pulse radiation," *IEEE Trans. Antennas Propagat.*, vol. 42, pp. 975–982, July 1994.

[10] A. A. Lestari, A. G. Yarovoy, and L. P. Ligthart, "RC-loaded bow-tie antenna for improved pulse radiation," *IEEE Trans. Antennas Propagat.*, vol. 52, pp. 2555–2563, Oct. 2004.

[11] A. A. Lestari, A. G. Yarovoy, and L. P. Ligthart, "Adaptive wire bow-tie antenna for GPR applications," *IEEE Trans. Antennas Propagat.*, vol. 53, pp. 1745–1754, May 2005.

[12] B. Lampe and K. Holliger, "Resistively loaded antennas for ground-penetrating radar: A modeling approach," *Geophysics*, vol. 70, pp. 23–32, May-June 2005.

[13] Y. Nishioka, O. Maeshima, T. Uno, and S. Adachi, "FDTD analysis of resistor-loaded bow-tie antennas covered with ferrite-coated conducting cavity for subsurface radar," *IEEE Trans. Antennas Propagat.*, vol. 47, pp. 970-977, June 1999.

[14] R. E. Collin, *Foundations for Microwave Engineering* , 2^{nd} ed., Wiley-IEEE Press, 2000.

[15] D. R. Saini, V. M. Nadkarni, P. D. Grover, and K. D. P. Nigam, "Dynamic mechanical, electrical and magnetic properties of ferrite filled styrene-isoprene-styrene," *Journal of Materials Science*, vol. 21, pp. 3710-3716, Oct. 1986.

[16] Emerson & Cuming microwave products. Eccostock HiK500F technical datasheet. Avail-

able online at: http://www.eccosorb.com/file/861/ek-025%20eccostock%20hik500f%20.pdf

[17] K. C. Gupta, R. Garg, and I. J. Bahl, *Microstrip Lines and Slotlines*, Artech House, 1979.

[18] R. L. Carrel, "The characteristic impedance of two infinite cones of arbitrary cross section," *IRE Trans. Antennas Propagat.*, vol. 6, pp. 197–201, Apr. 1958.

[19] M. Abramovich and I. A. Stegun, *Handbook of Mathematical Functions*, Dover Publications, 1968.

[20] K. S. Yee, "Numerical solution of initial boundary value problems involving Maxwell's equations," *IEEE Trans. Antennas Propagat.*, vol. 14, pp. 302–307, May 1966.

[21] A. Taflove and S. C. Hagness, *Computational Electrodynamics: The Finite-Difference Time-Domain Method*, 3^{rd} ed., Artech House, 2005.

[22] D. Caratelli and R. Cicchetti, "A full-wave analysis of interdigital capacitors for planar integrated circuits," *IEEE Trans. Magnetics*, vol. 39, pp. 1598–1601, May 2003.

[23] D. Caratelli, R. Cicchetti, G. Bit-Babik, and A. Faraone, "A perturbed E-shaped patch antenna for wideband WLAN applications," *IEEE Trans. Antennas Propagat.*, vol. 54, pp. 1871-1874, June 2006.

[24] S. D. Gedney, "An anisotropic perfectly matched layer-absorbing medium for the truncation of FDTD lattices," *IEEE Trans. Antennas Propagat.*, vol. 44, pp. 1630-1639, Dec. 1996.

[25] DEMINE partners. Public Report D16, European Project 29902 DEMINE, 2002. Available online at: http://www.eudem.vub.ac.be/files/demine_final_ report.pdf

[26] R. Persico and G. Prisco, "A reconfigurative approach for SF-GPR prospecting," *IEEE Trans. Antennas Propagat.*, vol. 56, pp. 2673-2680, Aug. 2008.

Diego Caratelli was born in Latina, Italy on May 2, 1975. He received the Laurea (summa cum laude) and Ph.D. degrees in Electronic Engineering from "La Sapienza" University of Rome, Italy in 2000 and 2004, respectively. In 2005, he joined as a Contract Researcher the Department of Electronic Engineering, "La Sapienza" University of Rome. Since 2007, he is with the International Research Centre for Telecommunications and Radar (*IRCTR*) of Delft University of Technology, the Netherlands, as a Senior Researcher.

His main research activities include the design, analysis and experimental verification of printed microwave and millimeter-wave passive devices and wideband antennas for satellite, *WLAN* and *GPR* applications, the development of analytically based numerical techniques devoted to the modeling of electromagnetic field propagation and diffraction processes, as well as the analysis of *EMC*/*EMI* problems in sensitive electronic equipment.

Dr. Caratelli was the recipient of the 2010 Young Antenna Engineer Prize at the 32th European Space Agency Antenna Workshop. He is a member of the Italian Electromagnetic Society (*SIEm*).

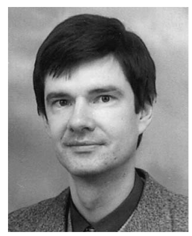

Alexander G. Yarovoy (M'96-SM'04) graduated from the Kharkov State University, Ukraine, in 1984 with the Diploma with honor in radiophysics and electronics. He received the Candidate Phys. & Math. Sci. (Ph.D. equivalent) and Doctor Phys. & Math. Sci. (D.Sc. equivalent) degrees in radiophysics in 1987 and 1994, respectively.

In 1987, he joined the Department of Radiophysics at the Kharkov State University as a Researcher and became a Professor there in 1997. From September 1994 through 1996, he was with Technical University of Ilmenau, Germany as a Visiting Researcher. Since 1999, he is with the International Research Centre for Telecommunications-Transmission and Radar (*IRCTR*) at the Delft University of Technology, the Netherlands. Since 2009, he leads there a chair of Microwave Technology and Systems for Radar. His main research interests are in ultra-wideband (*UWB*) microwave technology and its applications (in particular, *UWB* radars) and applied electromagnetics (in particular, *UWB* antennas).

Prof. Yarovoy is the recipient of a 1996 International Union of Radio Science (*URSI*) "Young Scientists Award" and the European Microwave Week Radar Award in 2001 for the paper that best advances the state-of-the-art in radar technology (together with L.P. Ligthart and P. van Genderen). Prof. Yarovoy served as the Chair of the 5th European Radar Conference (*EuRAD'08*), Amsterdam, The Netherlands, and Co-Chairman and the Technical Program Committee Chair of the Tenth International Conference on Ground Penetrating Radar (*GPR2004*), Delft.

Design and Full-Wave Analysis of Cavity-Backed Resistively Loaded Circular-End Bow-Tie Antennas for GPR Applications – Part II

Diego Caratelli and Alexander Yarovoy

Delft University of Technology, IRCTR
Mekelweg 4 – 2628 CD Delft, the Netherlands
d.caratelli@tudelft.nl

Abstract – In this paper, a comprehensive analysis of a novel GPR antenna featuring almost $30:1$ relative bandwidth ($55\ MHz - >1.5\ GHz$), with a maximum antenna size of $40\ cm$ is performed. Antenna transient behavior, near-field radiation, and impact of the ground are analyzed in details. It has been shown that the antenna exhibits reduced and short ringing, low spurious energy emission in the air region, as well as stable circuital and radiation properties over different types of soil. Furthermore, the analysis of buried pipe detection using two such antennas has been performed. Novelty of such investigation lies in the fact that at the lowest operational frequency both the receive antenna and buried pipe are situated in the near-field region, whilst at the highest operational frequency only the far field is playing the role. From this analysis, antenna coupling level and waveforms of the target return, which are of crucial importance for GPR system design, are determined.

Index Terms – Antenna coupling, antenna transient behavior, bow-tie antenna, buried pipe, ground-penetrating radar, near-field radiation.

I. INTRODUCTION

In Part II of this paper, the detailed full-wave analysis of the ultra-wideband cavity-backed resistively loaded bow-tie antenna for ground penetrating radars (GPR) presented by the authors in [1] and exhibiting almost $30:1$ relative bandwidth ($55\ MHz - >1.5\ GHz$), with a maximum antenna size of $40\ cm$ is carried out. Dielectric embedding and resistive loading of the radiating structure are used to reduce the flair angle and the antenna size, as well as to assure stable antenna performance over different types of the ground. To reduce parasitic emission to air, the antenna is cavity backed [2–3]. Special cavity filling is suggested in order to keep wideband antenna matching. The specially developed locally conformal finite-difference time-domain ($FDTD$) procedure [1] is used for numerical optimization of the antenna loading profile.

In the case of stepped-frequency continuous-wave ($SFCW$) radar applications (for which the antenna is designed), the synthesis of a pulse in time domain requires the deconvolution of the antenna impulse response [4]. So, antenna features such as the transient behavior and near-field radiation properties have a relevant impact on the performance of a complete GPR system, and thus analyzed in details. The proximity effect of the ground may adversely affect the radiation properties and circuital performance of the antenna [5] and directly affect the antenna impulse response. Thus, ground influence on all antenna characteristics have been studied carefully.

An extensive analysis of the subsurface radar consisting of two identical cavity-backed resistively-loaded bow-tie antennas located above a lossy homogeneous half space where an infinitely-long dielectric pipe is buried is carried out. Novelty of such investigation lies in the fact that at the lowest operational frequency both the receive antenna and the buried pipe are situated in the near-field region, whilst at the highest operational frequency only the far field is playing the role. The obtained numerical results, also, provide a physical insight into the underlying mechanisms of subsurface diffraction and antenna mutual coupling processes. This information in turn is important to specify the requirements of a complete *GPR* system such as maximal level of the received signal [9–10], system dynamic range, and radiation level in the air region (subject to e.g. *FCC* regulations), as well as to optimize the performance of detection algorithms in terms of clutter rejection.

This paper is organized as follows. Transient behavior of the antenna and its near-field radiation properties are investigated in Sections II and III, respectively. The impact of the ground on the electromagnetic characteristics of the radiator is deeply discussed in Section IV. Finally, Section V presents a thorough analysis of the *GPR* unit in realistic operative scenarios.

II. THE ANTENNA TRANSIENT BEHAVIOR

The time-domain behavior of the electromagnetic field radiated by the structure has been investigated to gain a physical insight into transient emission phenomena responsible for the antenna properties.

Shown in Fig. 1 is the distribution of the $y-$ component of the electric field excited along the $H-$plane of the antenna ($xz-$plane), where the other $E-$field components are vanishing due to the symmetry of the radiating element. The observation points are located at different polar angles θ, along a circle of radius $r_o = 40\ cm$, centered at the projection of the feeding point on the air-ground interface. The field component E_y is graphed positive on the side of the time axis for which $\hat{\theta}$ points away from the axis (clockwise direction). The dashed curves marked W_{g_i} $(i = 0, 1, 2, ...)$ and W_{a_j} $(j = 1, 2, ...)$ connect the times of arrival for different wavefronts in the ground and air region, respectively (see Fig. 2). In particular, the curve W_{g_0} related to the radiation process occurring at the feeding point is roughly a circle meaning that, at every observation point in the ground, the radio wave

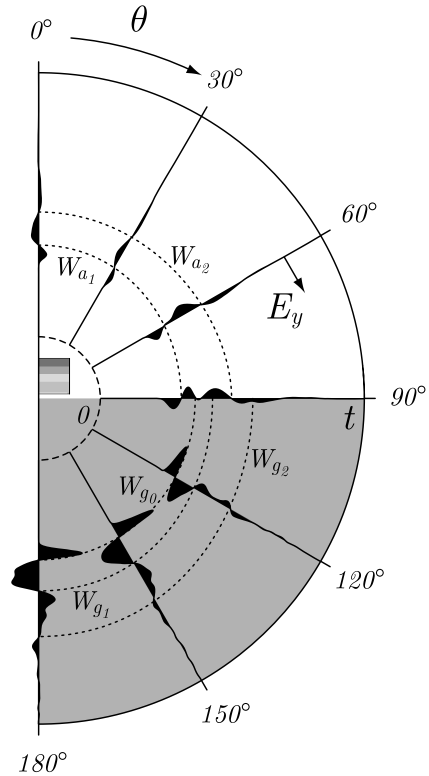

Fig. 1. Time-domain behavior of the electric field radiated along the $H-$plane of the antenna. The observation points are located at different polar angles θ, along a circle of radius $r_o = 40\ cm$, centered at the projection of the feeding point on the air-ground interface.

contribution from the feed arrives at the same time

$$t_{g_0} \simeq t_0 + \frac{r}{c_0}\sqrt{\varepsilon_{r_g}}\,, \tag{1}$$

where c_0 denotes the speed of light in free space. As it appears from Fig. 2, the interaction of this wave with the metallic walls forming the shielding structure is responsible for the excitation of a diffracted field contribution, resulting in two different wavefronts W_{g_1} and W_{a_1}. The time of arrival of such radio signal changes with the angle of observation in the ground and air regions, as

$$t_{g_1} \simeq t_0 + \frac{D_c}{2c_0}\sqrt{\varepsilon_{r_+}} + \frac{\sqrt{r^2 + \frac{D_c^2}{4} - rD_c\cos\theta}}{c_0}\sqrt{\varepsilon_{r_g}} \tag{2}$$

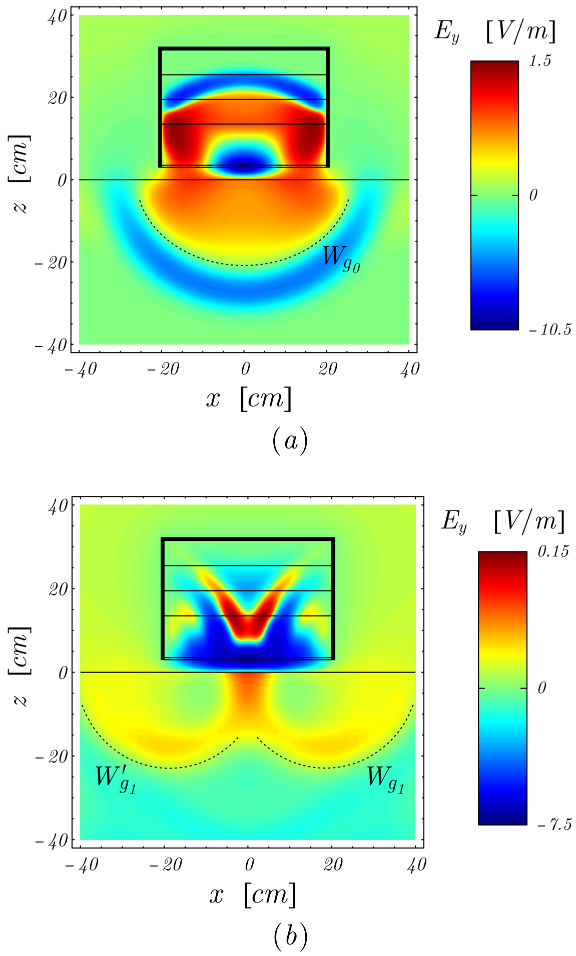

Fig. 2. Spatial distribution of the electric field excited along the $H-$plane of the cavity-backed resistively-loaded bow-tie antenna at the normalized time $t/\tau_g = 17.5$ (a), and $t/\tau_g = 35$ (b). The antenna is elevated over a homogeneous ground with electrical properties $\varepsilon_{r_g} = 6$ and $\sigma_g = 0.015$ S/m. The radiation process from the feed, as well as the diffraction phenomena arising from the field interaction with the cavity can be noticed.

and

$$t_{a_1} \simeq t_0 + \frac{D_c}{2c_0}\sqrt{\varepsilon_{r_+}} + \frac{\sqrt{r^2 + \frac{D_c^2}{4} - rD_c\cos\theta}}{c_0}, \tag{3}$$

respectively. The diffracted field then propagates back to the feed point, generating secondary undesired emission/diffraction phenomena with wavefronts W_{g_2} and W_{a_2}. This process repeats and results in the well-known *ringing* effect. This information can be usefully employed to optimize the antenna performance in realistic GPR surveys in terms of clutter rejection.

III. THE NEAR-FIELD ANTENNA PERFORMANCE

The goal of this study is to analyze antenna radiation properties in the near-field region, and the spatial distribution of the radiated electromagnetic field in the ground. Furthermore, the impact of different loading profiles on the total radiation level is analyzed.

Field radiation processes from the antenna in the near-zone have been investigated for three different loading profiles: $\sigma_0 = 10$ $S/m < \frac{3}{4}\sigma_{opt}$, $\sigma_0 = \sigma_{opt}$, and $\sigma_0 = 100$ $S/m > \sigma_{opt}$. The goal of this study was to analyze the impact of different loading profiles on the total radiation level and the focusing of the electromagnetic field into the ground. From Fig. 3, it appears that at low frequencies (e.g., $f = 100$ MHz) variations of the loading profile parameter result in considerable variations of the radiated downwards electric field (differences are of about 10 dB). However, starting from $f \simeq 200$ MHz, variations of the loading profile do not cause significant differences in the magnitude of the radiated field. It, also, means that the antenna efficiency is not considerably affected by the resistive loading profile that, on the other hand, plays an important role in the impedance matching property of the antenna. As it appears in Fig. 3, the surface waves level excited at the air-ground interface decreases with frequency. Consequently, the parasitic coupling processes in the antenna pair configuration may be expected to be maximum at low frequency because of the reduced electrical size of the radiating structure.

In the higher frequency band, several higher-order modes can propagate inside the metallic cavity, and each mode is characterized by a specific guided wavelength and, consequently, radiation angle into the ground. Such phenomenon can be observed in the field map shown in Fig. $3c$. Furthermore, Fig. 4 clearly demonstrates the effectiveness of the shielding structure in reducing the spurious energy emission level in the air region, as well as enhancing the antenna performance in terms of near-field front-to-back radiation ratio, defined as follows

$$FBR\,(r_o) = 20 \log \frac{|\underline{E}\,(0, 0, -r_o)|}{|\underline{E}\,(0, 0, r_o)|}\,, \qquad (4)$$

denoting r_o the observation distance from the projection of the feeding point on the air-ground interface. As it can be inferred, such parameter is conveniently introduced to quantify electromagnetic field focusing properties of the antenna. In Fig. 4, we can notice that the shielded antenna is characterized by a reduced back-radiation level, which is at least $9\ dB$ be-

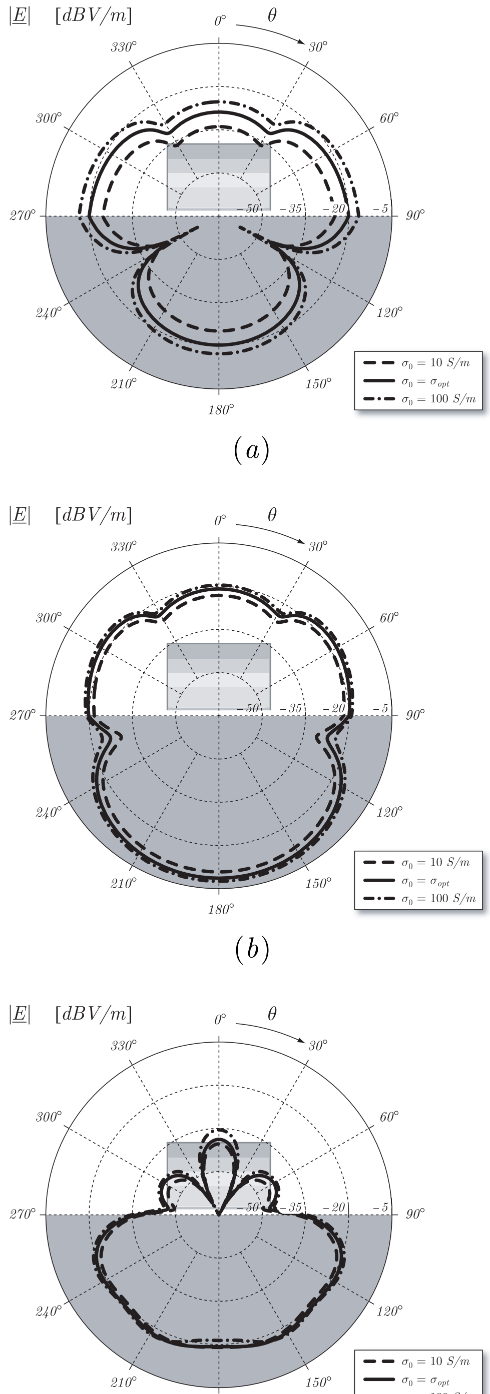

Fig. 3. $H-$ plane near-field radiation pattern of the cavity-backed resistively-loaded bow-tie antenna at frequency $f = 100\ MHz$ (a), $f = 200\ MHz$ (b), $f = 1\ GHz$ (c). The observation points are located along a circle of radius $r_o = 40\ cm$ centered at the projection of the feeding point on the air-ground interface.

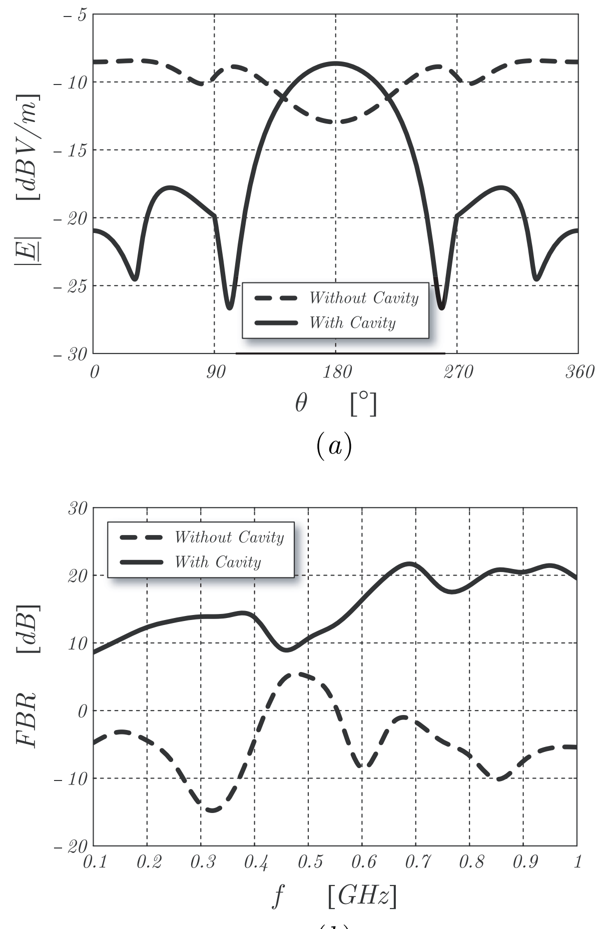

Fig. 4. Effect of the shielding cavity on the $H-$ plane radiation pattern at $200\ MHz$ (a), and the front-to-back radiation ratio (b) of the antenna. The observation distance from the projection of the feeding point on the air-ground interface is $r_o = 40\ cm$.

low the peak value of the radio signal propagating in the soil over the whole operational frequency band. This in turn is useful to reduce potential electromagnetic interferences with nearby sensitive electronic equipment.

To analyze the electromagnetic field transmitted into the ground, the subsurface antenna footprint at a depth of $15\ cm$ has been also computed at frequencies $f = 100\ MHz$, $f = 200\ MHz$, and $f = 1\ GHz$. The antenna footprint, representing the spot illuminated by the antenna on the ground surface or subsurface, plays an important role in GPR applications, In fact, as indicated by Daniels [4], radar imaging can be improved when the shape and size of footprint are comparable to those of the targets. When a footprint is too large it gives rise to subsurface clutter. On the other hand, a too small footprint makes the detection of buried objects difficult because of the reduced strength of the target response in a radar survey ($B-$ scan). An optimal footprint is, also, important to improve target localization. For long targets like buried pipes or cables, it is desired to have a footprint with elongated shape, whereas for circular targets such as landmines, a footprint with circular shape would be preferred.

Figure 5 demonstrates that the electric field transmitted by the antenna in the ground is mainly polarized along the $y-$ axis (in $E-$ plane of the antenna). In particular, the peak level of the normalized cross-polar field component $E_x/|\underline{E}_\tau|_{\max}$ at a depth of $15\ cm$ is found to be below $-9.5\ dB$ over the whole operational frequency band, from $100\ MHz$ to $1\ GHz$. In Fig. 5, one can also notice that the $-3dB$ subsurface footprint of the considered antenna features a quasi-elliptical shape with semi-axes a_x, a_y directed along the coordinate axes. It results that $a_x < a_y$ at low frequency ($f \lesssim 200\ MHz$), meaning that the footprint exhibits an elongated shape along the $y-$ axis, which would be suitable for detecting and locating long objects. The effective footprint assumes a nearly circular shape ($a_x \simeq a_y$) at $f \simeq 200\ MHz$, where the antenna efficiency and the energy level transmitted by the radiating element into the ground are maximum. Such mode of operation is to be preferred for detection of circular-symmetric targets. Moreover, as in this case the largest size of the footprint is obtained, the mentioned operating frequency is well suited to perform a quick scan over a large area. In the high-frequency band ($f \gtrsim 200\ MHz$) a_x tends to be greater than a_y, mainly due to the effect of higher-order modes excited in the metallic cavity. As a result, the footprint tends to become elongated along the $x-$ axis, which is useful to improve localization of long objects as in the low-frequency operation mode. In conclusion, Fig. 5 shows the footprint adaptation capability of the proposed antenna in the frequency domain with respect to the size and shape of the targets. Moreover, it's worth noting that higher operating frequency causes the radar footprint to concentrate in a reduced area near the feeding point. This information can be usefully employed to optimize the localization of small buried objects, as well as to improve the performance of detection algorithms in terms of clutter rejection.

IV. THE IMPACT OF THE GROUND

The goal of this study is to analyze the impact of the ground on circuital and radiation properties of the antenna. This, also, includes analysis of the antenna performance for different elevations above the air-ground interface.

The circuital characteristics of the antenna with optimal loading profile ($\sigma_0 = \sigma_{opt}$) have been analyzed in detail for different subsurface conditions (see Fig. 6). In particular, the proposed radiating element has been assumed to be elevated over sandy soil ($\varepsilon_{r_g} = 4$, $\sigma_g = 0.004\ S/m$), asphalt ($\varepsilon_{r_g} = 6$, $\sigma_g = 0.015\ S/m$), and dry clay ($\varepsilon_{r_g} = 16$, $\sigma_g = 0.03\ S/m$). It can be noticed that the antenna is well matched to the feeding line starting from the frequency $f_\ell \simeq 55\ MHz$. Due to resistive loading and dielectric embedding, the antenna input impedance as well as the lowest operational frequency f_ℓ are only slightly affected by the very different operative conditions (see Fig. 6). On the other hand, the ground is responsible for a minor loading effect of the antenna in the low-frequency band,

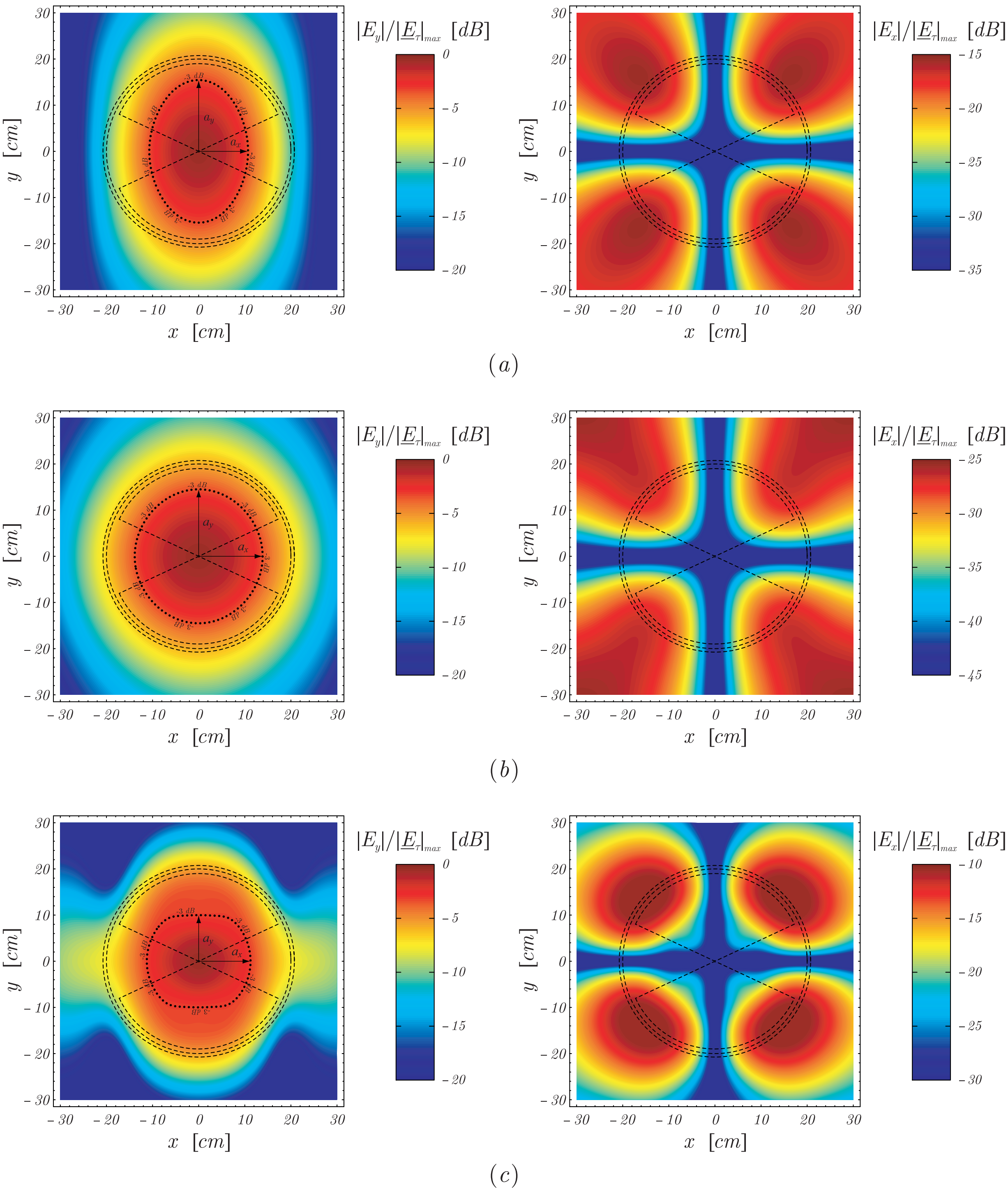

Fig. 5. Normalized subsurface antenna footprints at $15\ cm$ depth inside the ground. Frequency: $f = 100\ MHz$ (a), $f = 200\ MHz$ (b), $f = 1\ GHz$ (c). The antenna is elevated over a ground modeled as a homogeneous half space with electrical properties $\varepsilon_{r_g} = 6$ and $\sigma_g = 0.015\ S/m$.

where the absorbing property of soil plays a significant role to reduce the level of spurious reflections and, consequently, the fluctuations in the impedance curves. Moreover, when the soil changes from *soft* ground (e.g. sand) to *hard* ground (e.g. clay), the footprint tends to become more compact in the $H-$plane of the antenna ($x-$direction), as it clearly appears from Fig. 7.

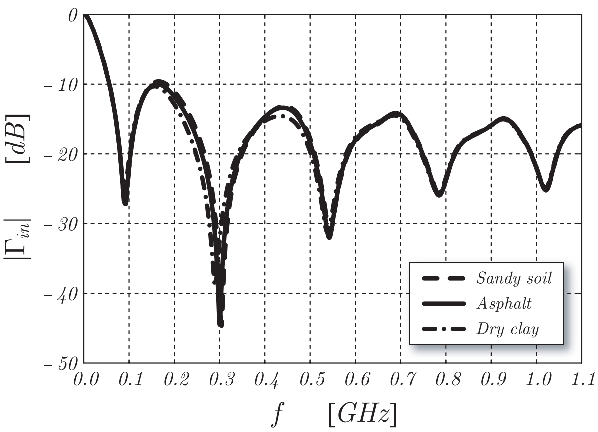

Fig. 6. Frequency behavior of the input reflection coefficient of the cavity-backed resistively-loaded bow-tie antenna for different electrical properties of the ground. The antenna is elevated 3 cm over the air-ground interface.

The input impedance of the considered radiating structure as function of the elevation above ground has been also evaluated. The computed results are given in Figs. 8 and 9. As it can be noticed in Fig. 8, the influence of the antenna elevation on the frequency behavior of the relevant input reflection coefficient is very significant only for close proximity to the interface. In particular, the smaller the distance from the interface, the better the impedance matching of the antenna to the feeding line due to the additional resistive loading effect of the lossy ground. The antenna elevation, also, has impact on the structure performance in terms of radiated power level, and radar footprint. In Fig. 9, one can observe that decreasing the distance of the radiator from the air-ground interface generally leads to a flattening of the subsurface footprint in the $E-$plane of the antenna ($y-$direction). Moreover, as it appears from Fig. 10, the amount of energy coupled into the ground tends to increase as the elevation over the soil becomes smaller, while reducing the parasitic back-radiation level in the air region. This information should be properly taken into account in a *GPR* survey in order to enhance the radar detection of buried targets.

V. THE RADAR DETECTION OF BURIED DIELECTRIC PIPES

In this section, emphasis is devoted to the analysis of detectability of an infinitely-long buried dielectric pipe by the subsurface radar unit consisting of two identical cavity-backed resistively-loaded bow-tie antennas (see Fig. 11). The coupling level between the transmit and receive antennas is a critical parameter in *GPR* design limiting detectability of buried targets. In the considered configuration, the transmit (Tx) antenna, denoted as antenna *#1*, emits a Gaussian electromagnetic pulse that propagates into the ground, where it interacts with the target, modeled as a $y-$directed circular cylin-

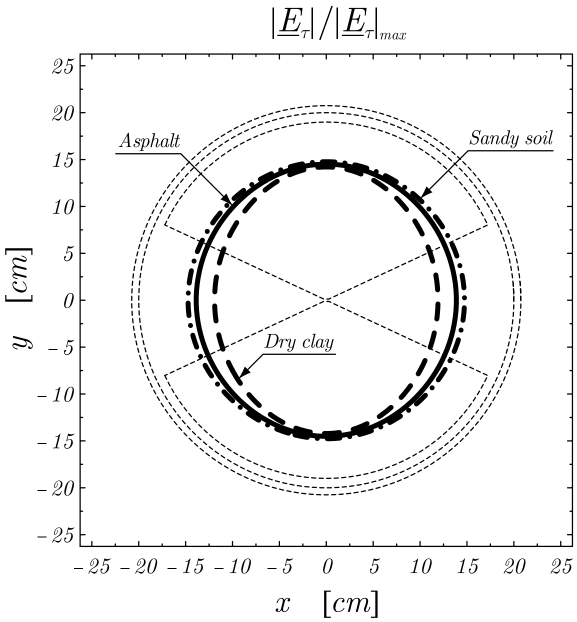

Fig. 7. Normalized $-3\ dB$ subsurface antenna footprint at 15 cm depth for different ground characteristics. The operating frequency is $f = 200\ MHz$, where the antenna efficiency and the energy level transmitted into the ground are maximum. The antenna is elevated 3 cm over the air-ground interface.

der having diameter $D_p = 20\ cm$, buried at a depth $h_p = 50\ cm$. This interaction results in a diffracted electromagnetic field which is measured by the receive element (Rx) of the radar, denoted as antenna *#2*. By changing the location of the radar on the soil interface and recording the output of the receive antenna as function of time (or frequency) and radar location, one obtains the scattering data, which can be processed to get an image of the subsurface.

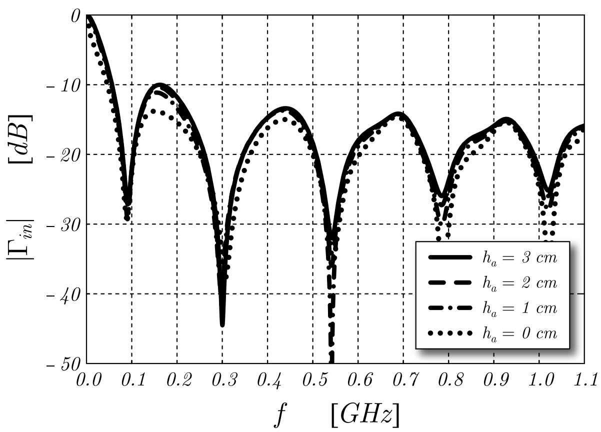

Fig. 8. Frequency behavior of the input reflection coefficient of the cavity-backed resistively-loaded bow-tie antenna as function of the elevation above ground, modelled as a lossy homogeneous half-space having relative permittivity $\varepsilon_{r_g} = 6$ and electrical conductivity $\sigma_g = 0.015\ S/m$.

Since the considered structure is reciprocal and symmetrical (see Fig. 11), the relevant scattering matrix $\underline{\underline{S}}$ is completely described in terms of the S_{11} and S_{21} parameters, whose evaluation is carried out by feeding the radiating element *#1*, and setting the excitation signal of the antenna *#2* equal to zero.

As it appears from Fig. 12, the return loss of the transmit antenna is negligibly affected by the buried target that, at the same time, has a reduced impact on the S_{21} parameter. This means that the antenna coupling is mainly responsible for the received signal. It is worth mentioning that the maximum coupling level is a decreasing function of antenna separation, d_a, and tends to become larger as the relative permittivity of the pipe ε_{r_p} increases

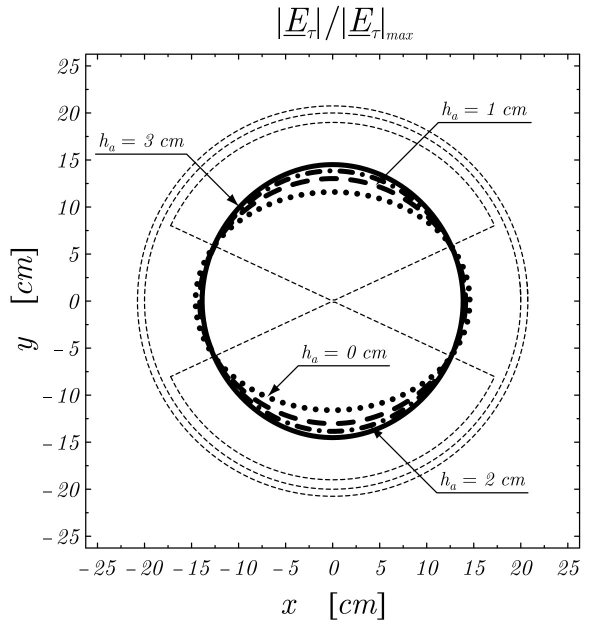

Fig. 9. Normalized $-3\ dB$ subsurface antenna footprint at $15\ cm$ depth for different elevations above ground. The operating frequency is $f = 200\ MHz$.

(see Fig. 12). In particular, for an antenna separation $d_a = 5\ cm$, the coupling level is below $-30\ dB$ over the whole operational frequency band $100\ MHz - 1\ GHz$. The effect of the antenna elevation above the ground, h_a, has been also investigated, although the relevant analysis is not reported here for sake of brevity. It has been found that, as h_a decreases, the antenna return-loss response is slightly shifted towards lower frequencies because of the proximity effect of the soil. On the other hand, the ground influence on the S_{21} parameter is noticeable only at high frequencies, where the mutual coupling level decreases as the radiating elements approach the air-ground interface.

As it can be noticed in Fig. 13, the peak-to-peak level of the voltage contribution v_{d_2} due to the presence of the pipe, excited at the input terminals of the receive antenna, is essentially function of the difference between relative permittivities of the ground and the pipe, namely the dielectric contrast $\Delta\varepsilon_r = \varepsilon_{r_g} - \varepsilon_{r_p}$, and is about one order of magnitude smaller than the peak-to-peak level of the voltage contribution v_{r_2} due to direct antenna coupling, un-

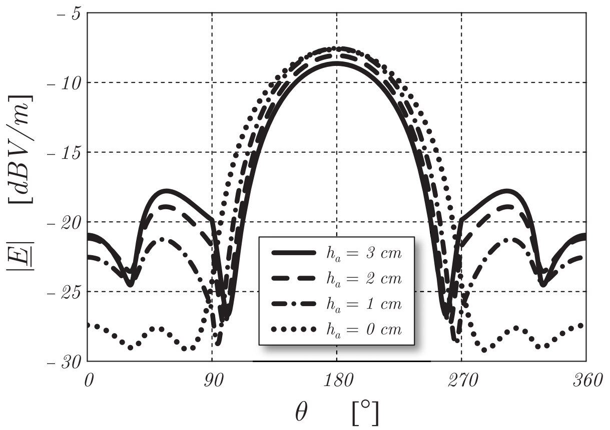

Fig. 10. $H-$ plane radiation pattern at 200 MHz of the resistively-loaded bow-tie antenna for different elevations over the soil. The observation distance from the projection of the feeding point on the air-ground interface is $r_o = 40\ cm$.

der the assumption that the depth of the buried target is $h_p = 50\ cm$. The spectrum of the radio signal arising from the subsurface diffraction is similar to the spectrum of the direct coupling, and the relevant largest spectral contribution is given by the frequency harmonics around 200 MHz, the frequency around which the direct coupling reaches its maximum. It should be noticed that parasitic antenna coupling can potentially result in the early-time masking of the buried target. So, to reduce or possibly prevent such problem, it is of crucial importance in a *GPR* design to adopt an antenna system with a short in time direct coupling response, and reduced decaying factor. In particular, it has been numerically found that the exponential decaying factors of v_{d_2} and v_{r_2} are, for the considered antenna pair configuration, $\tau_{d_2} \simeq 2.766\ ns$ and $\tau_{r_2} \simeq 2.518\ ns$, respectively.

It is worth noting that, where the dielectric contrast of the buried pipe $\Delta\varepsilon_r$ is negative, a phase inversion occur in the diffracted field distribution and, consequently, in the relevant radio signal component detected by the receiver. This results in interference phenomena responsible for a significant downward focalization of the total field, as outlined in Fig. 14. Such information can be usefully employed to optimize the detection of buried pipes in subsurface radar applications, as well as to enhance the performance of detection algorithms in terms of clutter rejection.

VI. CONCLUSION

We have investigated the performance of a novel cavity-backed loaded bow-tie antenna which has been designed for a new ground penetrating radar. The considered radiating structure shows an outstandingly large operational

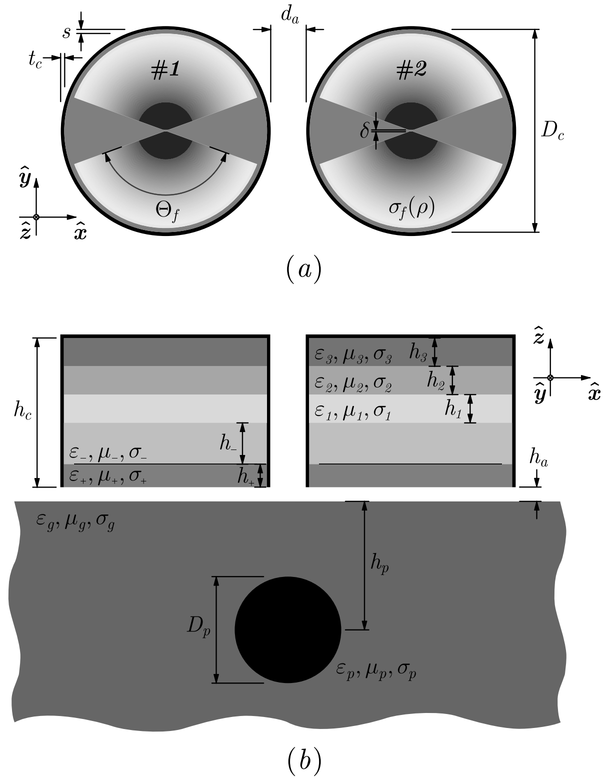

Fig. 11. Bottom (a) and cross-sectional (b) view of a subsurface radar unit consisting of two identical cavity-backed resistively-loaded bow-tie antennas located above a lossy homogeneous half space where an infinitely-long dielectric pipe is buried. Structure characteristics: $D_c = 40\ cm$, $s = 1\ cm$, $t_c = 0.5\ cm$, $\Theta_f = 130°$, $\delta = 0.25\ cm$, $h_c = 28.5\ cm$, $h_a = 3\ cm$, $\varepsilon_{r_g} = 6$, $\sigma_g = 0.015\ S/m$, $h_+ = 0.5\ cm$, $\varepsilon_{r_+} = 3$, $\sigma_+ = 0\ S/m$, $h_- = 10\ cm$, $\varepsilon_{r_-} = 10$, $\sigma_- = 0\ S/m$, $h_1 = 6\ cm$, $\varepsilon_{r_1} = 11$, $\sigma_1 = 0.125\ S/m$, $h_2 = 6\ cm$, $\varepsilon_{r_2} = 15$, $\sigma_2 = 0.25\ S/m$, $h_3 = 6\ cm$, $\varepsilon_{r_3} = 20$, $\sigma_3 = 1\ S/m$, $d_a = 5\ cm$, $h_p = 50\ cm$, $D_p = 20\ cm$.

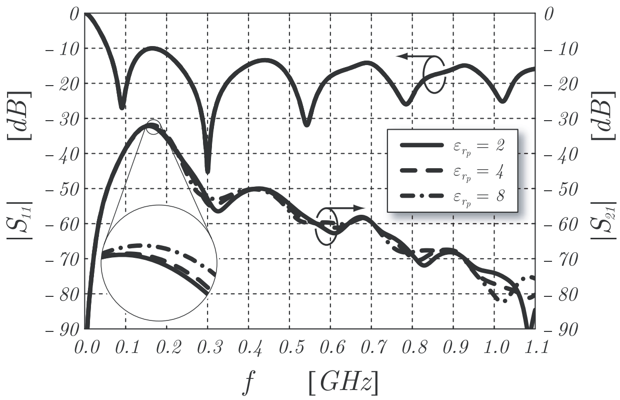

Fig. 12. Frequency behavior of the scattering parameters of the cavity-backed resistively-loaded bow-tie antenna pair for different permittivities of the buried pipe, having electrical conductivity $\sigma_p = 0.01\ S/m$. The antenna separation is assumed to be $d_a = 5\ cm$.

bandwidth from $55\ MHz$ to $>1.5\ GHz$ combined with a maximal size of $40\ cm$.

The circuital and radiation characteristics of the antenna with optimal loading profile have been investigated in detail for different subsurface conditions. The ground is responsible for a minor loading effect of the structure in the low-frequency band, where the absorbing property of soil plays a significant role to reduce the level of spurious reflections and, consequently, the fluctuations in the impedance curves. Similar minor

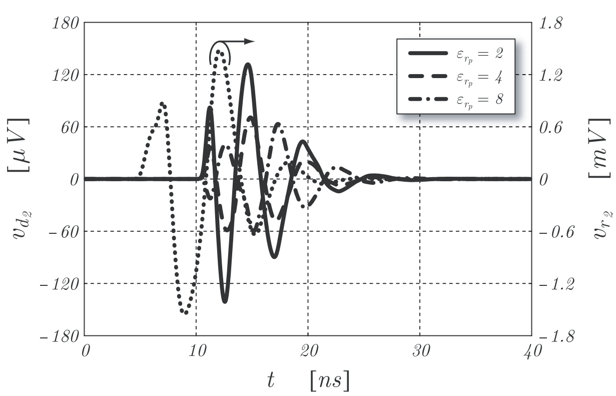

Fig. 13. Transient voltages at the receiver due to the direct coupling between antennas, and scattering from a buried dielectric pipe having relative permittivity ε_{r_p} and electrical conductivity $\sigma_p = 0.01\ S/m$.

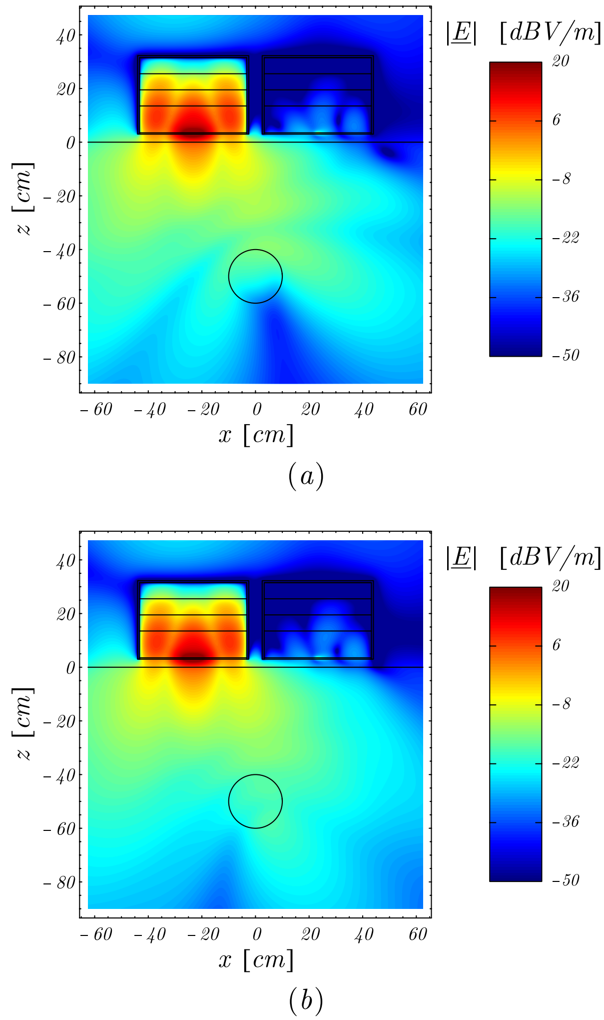

Fig. 14. Spatial distribution of the electric field excited along the vertical cut-plane of the antenna pair operating in presence of a buried dielectric pipe having relative permittivity $\varepsilon_{r_p} = 2$ (a) and $\varepsilon_{r_p} = 8$ (b). Operational frequency: $f = 500\ MHz$.

variations in the impedance curves have been observed by variations of the structure elevation above the ground. Antenna radiation properties in the near-field region are, also, only slightly affected by the ground. In particular, when the soil changes from *soft* ground (e.g. sand) to *hard* ground (e.g. clay), the antenna footprint tends to become slightly more compact. In general, the antenna clearly demonstrates ground invariant behavior, which is of ultimate importance for synthesis of time-domain pulses in *SFCW* radar applications.

The analysis of near-field radiation processes has shown a reasonably good transient behavior of the antenna, which simplifies the task of deconvolution of the antenna impulse response from the measured *SFCW* data. This behavior makes it possible to use the developed antenna in a time-domain radar. An interesting footprint adaptation capability of the proposed antenna in the frequency domain with respect to the size and shape has been observed. Such property can be usefully adopted to improve the radar detection of buried targets in a *GPR* survey. Also, the antenna exhibits relatively high value for the front-to-back radiation ratio and reduced spurious energy emission level in the air region, which allows for increase of the total output power of the radar transmitter without breaching allowed (e.g., by *FCC* regulations) radiation levels.

A particular attention has been devoted to the analysis of detectability of buried pipes by the subsurface radar unit consisting of two identical antennas. It has been found that the direct coupling level between transmit and receive antennas is below $-30\,dB$ over the whole operating frequency band from $100\,MHz$ to $1\,GHz$. In particular, the exponential decaying factor of the radio signal contribution at the receiver end due to the parasitic antenna coupling is reasonably small. Such feature is particularly important in order to reduce the early-time masking of the target in a *GPR* survey. The waveform and magnitude of received signals due to scattering from buried dielectric pipes have been also investigated. The obtained numerical results have provided a useful physical insight into antenna mutual coupling, and scattering from buried targets. This information is required to evaluate the required *GPR* dynamic range where the maximal received signal is due to the antenna coupling and the minimal detectable signal should be smaller than the weakest reflection from a thin dielectric pipe on the maximal expected depth.

ACKNOWLEDGMENT

This research has been carried out in the framework of *EU*-sponsored project *ORFEUS* (contract number: *FP6-2005-Global-4-036856*). The authors would like to thank anonymous reviewers for their suggestions and comments.

REFERENCES

[1] D. Caratelli, A. G. Yarovoy, and L. P. Ligthart, "Design and full-wave analysis of cavity-backed resistively loaded circular-end bow-tie antennas for GPR applications – Part I," accepted for publication in *ACES Journal*, 2010.

[2] D. Caratelli, "Full-wave analysis of cavity-backed resistively loaded bow-tie antennas for GPR applications," Delft University of Technology, the Netherlands, Tech. Rep. IRCTR–S–001–08, Jan. 11, 2008.

[3] D. Caratelli, A. Yarovoy, and L. P. Ligthart, "Full-wave analysis of cavity-backed resistively-loaded bow-tie antennas for GPR applications," *European Microwave Conference 2008*, Amsterdam, the Netherlands, pp. 204-207, October 27-31, 2008.

[4] D. Daniels, *Ground Penetrating Radar*, 2^{nd} ed., IEE Press, 2004.

[5] A. A. Lestari, A. G. Yarovoy, and L. P. Ligthart, "Numerical and experimental analysis of circular-end wire bow-tie antennas over a lossy ground," *IEEE Trans. Antennas Propagat.*, vol. 52, pp. 26-35, Jan. 2004

[6] Y. Nishioka, O. Maeshima, T. Uno, and S. Adachi, "FDTD analysis of resistor-loaded bow-tie antennas covered with ferrite-coated conducting cavity for subsurface radar," *IEEE Trans. Antennas Propagat.*, vol. 47, pp. 970-977, June 1999.

[7] D. Uduwawala, M. Norgren, P. Fuks, and A. W. Gunawardena, "A deep parametric study of resistor-loaded bow-tie antennas for ground-penetrating radar applications using FDTD," *IEEE Trans. Geosci. Remote Sensing*, vol. 42, pp. 732-742, Apr. 2004.

[8] K.-H. Lee, C.-C. Chen, F. L. Teixeira, and R. Lee, "Modeling and investigation of a geometrically complex UWB GPR antenna using FDTD," *IEEE Trans. Antennas Propagat.*, vol. 52, pp. 1983-1991, Aug. 2004.

[9] L. Gürel and U. Oguz, "Simulations of ground-penetrating radars over lossy and heterogeneous grounds," *IEEE Trans. Geosci. Remote Sensing*, vol. 39, pp. 1190-1197, June 2001.

[10] L. Gürel and U. Oguz, "Optimization of the transmitter–receiver separation in the ground-

penetrating radar," *IEEE Trans. Antennas Propagat.*, vol. 51, pp. 362-370, Mar. 2003.

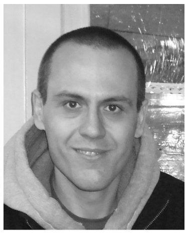

Diego Caratelli was born in Latina, Italy on May 2, 1975. He received the Laurea (summa cum laude) and Ph.D. degrees in Electronic Engineering from "La Sapienza" University of Rome, Italy in 2000 and 2004, respectively. In 2005, he joined as a Contract Researcher the Department of Electronic Engineering, "La Sapienza" University of Rome. Since 2007, he is with the International Research Centre for Telecommunications and Radar (*IRCTR*) of Delft University of Technology, the Netherlands, as a Senior Researcher.

His main research activities include the design, analysis and experimental verification of printed microwave and millimeter-wave passive devices and wideband antennas for satellite, *WLAN* and *GPR* applications, the development of analytically based numerical techniques devoted to the modeling of electromagnetic field propagation and diffraction processes, as well as the analysis of *EMC*/*EMI* problems in sensitive electronic equipment.

Dr. Caratelli was the recipient of the 2010 Young Antenna Engineer Prize at the 32th European Space Agency Antenna Workshop. He is a member of the Italian Electromagnetic Society (*SIEm*).

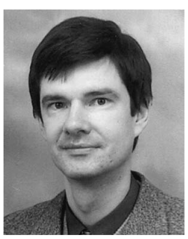

Alexander G. Yarovoy (M'96-SM'04) graduated from the Kharkov State University, Ukraine, in 1984 with the Diploma with honor in radiophysics and electronics. He received the Candidate Phys. & Math. Sci. (Ph.D. equivalent) and Doctor Phys. & Math. Sci. (D.Sc. equivalent) degrees in radiophysics in 1987 and 1994, respectively.

In 1987, he joined the Department of Radiophysics at the Kharkov State University as a Researcher and became a Professor there in 1997. From September 1994 through 1996, he was with Technical University of Ilmenau, Germany as a Visiting Researcher. Since 1999, he is with the International Research Centre for Telecommunications-Transmission and Radar (*IRCTR*) at the Delft University of Technology, the Netherlands. Since 2009, he leads there a chair of Microwave Technology and Systems for Radar. His main research interests are in ultra-wideband (*UWB*) microwave technology and its applications (in particular, *UWB* radars) and applied electromagnetics (in particular, *UWB* antennas).

Prof. Yarovoy is the recipient of a 1996 International Union of Radio Science (*URSI*) "Young Scientists Award" and the European Microwave Week Radar Award in 2001 for the paper that best advances the state-of-the-art in radar technology (together with L.P. Ligthart and P. van Genderen). Prof. Yarovoy served as the Chair of the 5th European Radar Conference (*EuRAD'08*), Amsterdam, The Netherlands, and Co-Chairman and the Technical Program Committee Chair of the Tenth International Conference on Ground Penetrating Radar (*GPR2004*), Delft.

A Partial Solution of MoM Matrices Based on Characteristic Basis Functions and its Application to On-Board Antennas Positioning

Jaime Laviada, Javier Gutiérrez-Meana, Marcos R. Pino, and Fernando Las-Heras

Área de Teoría de la Señal y Comunicaciones (TSC-UNIOVI)
University of Oviedo, Campus de Viesques, 33203 Gijón, Asturias, Spain
jlaviada@tsc.uniovi.es, jmeana@tsc.uniovi.es, mpino@tsc.uniovi.es, flasheras@tsc.uniovi.es

Abstract **─** A new technique, called incomplete Gauss-Jordan elimination (IGJE), is presented and hybridized with the characteristic basis function method (CBFM) to enable the partial solution of the method of moments (MoM) matrix. As a consequence, the goal of this technique is its application to optimization problems in electrically large scenarios where multiple but similar configurations need to be analyzed, since our method performs these analyses with a considerable reduction in the computational time and also memory. The term "similar" refers to the fact that the original structure is split into different blocks and modifications in the geometry (inserting, eliminating, or changing elements) of only a specific set of these blocks are allowed throughout the optimization process. In particular, we take advantage of this technique to analyze the optimum emplacement of an antenna on a given structure (e.g. a ship or airplane) with just one analysis. An example of an airplane antenna positioning is shown to illustrate the procedure.

Index Terms **─** Characteristic basis functions, method of moments, on-board antennas.

I. INTRODUCTION

Many usual simulations in the electromagnetic engineering involve the evaluation of small modifications on certain parts of a given structure. In this paper, this fixed part of the total structure will be referred to as *mother structure*. Among other examples, we can cite the tuning of antennas by systematically changing the dimensions of certain small metallic additions (e. g. a stub or a parasitic element). Another example of the previous situation is the study of the radiation pattern of an on-board antenna. In the latter case, the antenna is placed on multiple positions in order to study if the elements of the environment, such as the fuselage of an airplane or the tower of a ship, affect the radiation characteristics of the antenna. This results in multiple analyses of structures that share most of the geometry. In the method of moments context, several techniques have been proposed to enable the partial solution of the *mother structure* so that the analysis, after changing a part in the rest of the geometry, can be resumed.

The work on this kind of analysis has been dispersed along the years. However, a common step has been to speed up the computation of the entries of the matrix. For this purpose, the matrix with all the possible metallic parts is calculated and stored. Thus, if a substructure with some eliminated parts has to be analyzed, the related matrix is easily computed by removing the rows and columns associated to the removed metallic parts. After this stage, several techniques have been proposed in order to avoid solving the equations system from the scratch for each analysis. Although there is not an exhaustive comparison among these methods in the literature, their performance is expected to be close to each other since they are based on similar foundations.

Among the pioneering works on this field, we can cite the "add-on" method [1–3] that produces an incremental computation of the inverse of the impedance matrix based on the Sherman-Morrison formula and, therefore, enabling the access to partial solutions.

The research on this field has also been focused on modifying common solving techniques for equations systems such as the LU factorization

[4] or the Gaussian elimination [5] yielding schemes very appropriate for the optimization of microwave circuits and antennas [6]. Another efficient partial solver was proposed in [7] for the optimization via genetic algorithms. The work on partial solving has also been continued more recently for the optimization of non-intuitive planar structures [8, 9].

As previously mentioned, an extreme case of small modifications on a large structure is the positioning of on-board antennas. In this problem, the *mother structure* is typically an aircraft or ship where the antenna must be placed. The derived structures to be analyzed would be composed by the airplane or the ship and the antenna located in multiple positions. Since the aforementioned partial solving techniques must deal with the entire MoM matrix, they are typically limited in the electrical size of the *mother structure* and, therefore, their direct application to electrically large structures is not possible.

The analysis of on-board antennas has been traditionally tackled by hybrid methods that combine asymptotic techniques to analyze the *mother structures* with full-wave methods to analyze the antenna and its nearest environment. Among these techniques, we can cite hybridization of the method of moments with the physical optics [10] or with the uniform theory of diffraction [11].

Current tendencies are oriented towards the application of acceleration schemes such as the fast multipole method [12] since they do not require the approximations introduced by the asymptotic methods. These techniques are very powerful and enable the full-wave analysis of antennas on large electromagnetic structures [13–15]. However, they are based on iterative schemes rather than on direct solutions complicating the hybridization with the aforementioned partial-solving techniques.

A remarkable technique to analyze on-board antennas has been proposed in [16]. Authors decompose the geometry into multiple domains, one for the large and fixed structure and the remainder for the on-board antennas. Each domain is analyzed with full-wave methods in order to compute a scattering matrix relating the incident field on its boundary to the radiated field. Thus, if the antenna is changed, the method only has to recompute the scattering matrix of a small domain. However, if the antenna is moved, then the scattering matrix of the large domain must be also recomputed which can be very time-consuming.

Next sections are arranged as follows. Firstly, we present the incomplete Gauss-Jordan elimination (IGJE) that enables a partial solution compatible with the compression techniques that will be treated later. Afterwards, the compression of the matrix with the characteristic basis function method (CBFM) is detailed and its integration for the efficient evaluation of multiple antenna positioning is considered. In the results section, the application of the IGJE to antenna design is illustrated by means of the optimization of a reconfigurable antenna. The study of a VHF dipole at multiple positions on an airplane is considered to illustrate the capabilities of the inclusion of the IGJE into a locally modified CBFM method for dealing with electrically large structures. Finally, the conclusions are summarized and discussed.

II. INCOMPLETE GAUSS-JORDAN ELIMINATION SCHEME

A. Description of the method

The Gauss-Jordan elimination is a simple and well-known scheme to calculate the inverse of matrices. Although its application to solve equations systems is also possible, it is not usual because it requires a higher number of operations than other schemes (e.g., approximately three times more operations than a LU factorization).

This scheme pursues the reduction of the matrix into a row echelon form by means of basic operations row by row. Thus, in the n-th step, the Gauss-Jordan elimination seeks the first non-zero element (pivot element) in the n-th row, normalizes the row with this element and adds multiples of that row to the rest of rows in order to obtain zeros in the column of the pivot element. Equivalent operations are performed on the right hand side (RHS). At the end of the algorithm, the matrix is reduced to a row echelon form and, therefore, the solution of the equations system is straightforward.

In the case of MoM matrices, it will be proved later that the pivot element is always located in the diagonal so that the matrix is progressively transformed into the identity matrix. The Gauss-Jordan elimination without pivoting can be expressed using Matlab notation as:

```
for n = 1 : N
  Z(n,n:end) = Z(n,n:end) / Z(n,n);
  V(n,:) = V(n,:) / Z(n,n);
  for m = 1 : N
     if n == m
       continue;
     end
     Z(m,n:end) = Z(m,n:end) -…
       …Z(m,n)*Z(n,n:end);
     V(m,:) = V(m,:) - Z(m,n)*V(n,:);
  end
end
```

In the above description, Z is the matrix of the equations system with N unknowns and V is a matrix containing the right hand terms. At the end of the algorithm, the matrix V contains the solution to the equations system. After the step n, all the entries of the first n columns of matrix Z are zeros except the entries of the diagonal that are equal to one; so, it is not necessary to operate with these columns when adding row multiples and, therefore, it saves some CPU cycles.

Next, we detail how the conventional Gauss-Jordan elimination can be modified to obtain the incremental solution of a MoM problem. Let us split the geometry under analysis into two parts, one containing the *mother structure*, and the other one containing the possible metallic additions (e.g. parasitic elements) to the *mother structure*, with N_m and N_f unknowns respectively (typically $N_m >> N_f$). The total number of unknowns is given by $N = N_m + N_f$.

We will assume that the matrix is rearranged to place the unknowns related to the *mother structure* in the first rows and columns and the unknowns belonging to each metallic additions are, also, arranged consecutively. After N_m iterations, the matrix will reach the form shown in Fig.1a, i.e., the identity matrix is placed in the first $N_m \times N_m$ entries and the elements under this submatrix are zeros. Since we have carried out exactly the same operations on the initial $N_m \times N_m$ submatrix as if we consider the isolated *mother structure*, the first N_m coefficients of the RHS contain the solution of the isolated *mother structure*. If we continue the elimination until solving the unknowns associated to the next metallic addition, we will obtain the solution for the *mother structure* plus that addition. On the other hand, if we had swapped the rows and columns to place the rows and columns related to a different addition at the position of the submatrix related to the first addition (see Fig. 1b), we would have obtained the solution of the *mother structure* plus that different addition. Thus, it is very efficient to analyze the impact of different extensions of the *mother structure* just by resuming from the point of Fig.1a.

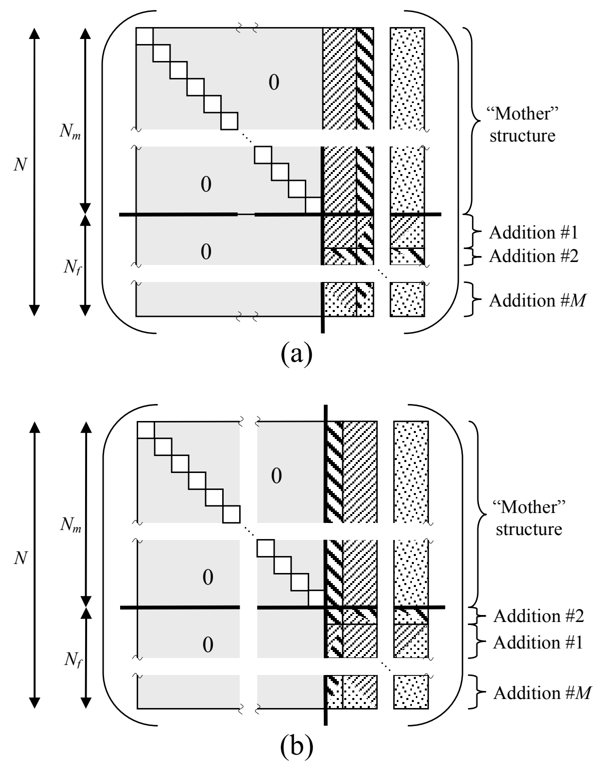

Fig. 1. Equations system matrix after solving the *mother structure*: (a) without any change; (b) after swapping rows and columns of the entries associated to the first and second additions.

Once the previous concepts have been detailed, it is straightforward to prove that the pivot element must be located in the diagonal. After k steps, the first $k \times k$ entries in the MoM matrix must be equal to the identity matrix (solution to the problem considering the k first basis functions). When another step is performed, a solution must exist as it corresponds to the problem of $k+1$ basis functions. Since the first $k \times k$ entries are the identity matrix, there is only one choice for the pivot element: its location in the

$k+1$ position of the diagonal. The reasoning can be extended to any arbitrary number of steps.

B. Complexity of the incomplete Gauss-Jordan elimination

The computational time cost to solve the *mother structure* can be approximated by the cost of solving the entire structure and, therefore, it is $O(N^3)$, as the usual direct solution schemes. On the other hand, the computational cost for resuming the analysis is only $O(N_f^2 N)$. Hence, this strategy involves a first analysis that is time-consuming but the penalty to analyze the rest of the combinations is very low.

The storage of the initial matrix and the time for the first analysis limit the size of the structures to be studied. In the next section, this problem will be mitigated by including recent developments related to reductions in the number of unknowns using efficient sets of macro basis functions to model parts of the geometry.

It is important to remark that after solving the *mother structure* (first N_m steps), it is only necessary to store the last N_f columns of the matrix, saving a large amount of memory in case we need to store several of these matrices (e.g. to carry out frequency sweeps).

III. ANTENNA POSITIONING WITH CHARACTERISTIC BASIS FUNCTIONS

In the previous section, we have seen how the MoM matrix can be partially solved. However, this methodology requires initially to store the entire MoM matrix so it is limited to electrically small geometries. In this section, we will show how the previous method in combination with the CBFM can be applied to the positioning of on-board antennas.

It is important to remark that in this case we must deal with parts of the geometry where two configurations are possible (with or without antenna) rather than analyzing the effect of adding metallic regions.

In particular, the problem under analysis consists in the study of one antenna for S positions on an electrically large structure. This situation is depicted in Fig. 2a for a cactus antenna placed on a ship for $S=5$. In other words, we pursue to analyze a structure where a given set of blocks can potentially contain the antenna yielding an *inter-block* strategy.

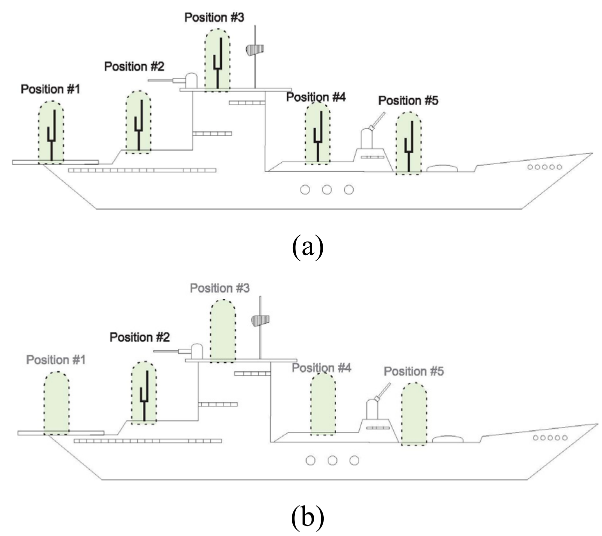

Fig. 2. Antenna positioning: a) all possible locations; b) antenna placed at position #2.

For this purpose, we will combine the aforementioned IGJE with the characteristic basis function method (CBFM) that has shown very desirable properties for the analysis of locally modified structures in the past [17].

The CBFM was developed with the aim of reducing the number of degrees of freedom when analyzing electromagnetic problems. The method is based on the use of the so-called "characteristic basis functions" (CBFs) which are defined on non-overlapped fragments of the geometry that are referred to as blocks.

These new basis functions are usually much less than the conventional low-level basis functions. Thus, this reduction enables the *direct solution* of problems much larger than the ones that can be analyzed with the conventional MoM. In addition, the direct solution avoids any potential convergence issue that could happen in the conventional fast algorithms which are based on iterative schemes. On the other hand, the current direct approaches can deal with a smaller number of unknowns if compared with the most powerful iterative schemes such as the FMM [12]. The CBFM is widely described in the literature and, therefore, we will only explain briefly the parts related to the current work. The reader is referred to [18-21] and the references therein for further details about the method.

Once the CBFs have been defined in terms of the low-level basis functions as in [20] and their coefficients are arranged by columns, then the matrix containing the interactions between the CBFs in the *m*-th observation block and the *n*-th source block is computed as:

$$\mathbf{Z}_{mn}^{(1)} = \mathbf{J}_m^t \mathbf{Z}_{mn}^{(0)} \mathbf{J}_n \ , \tag{1}$$

where $\mathbf{Z}_{mn}^{(0)}$ contains the reaction terms among the low-level basis functions of the *m*-th and *n*-th blocks. Thus, the original submatrix $\mathbf{Z}_{mn}^{(0)}$ is converted to a $K_m \times K_n$ block whose dimensions are typically around one order of magnitude less than the dimensions of the original matrix. It is also remarkable that the CBFM can be generalized through a multilevel formulation that enables to achieve higher compression rates for electrically large structures [22]. This compression together with the block partitioning is the keys to efficiently modify the geometry. In order to accomplish our goal, we split the geometry into T blocks. These blocks are classified into two types depending if they contain a possible location of the antenna, that will be referred to as antenna positioning block (AP block), or not. The other blocks contain the *mother structure* and, therefore, they will be referred to as *mother structure* blocks (MS blocks). Hence, there will be S AP blocks containing possible locations of the antenna and R blocks containing regular pieces of geometry, where $T = R + S$.

From the previous discussion, it can be inferred that both MS blocks and AP blocks can be created as in the conventional CBFM [18-21]). The only special rule that we have followed in this paper is that the volume enclosed by the antenna must be contained in one single CBFM block. It can be easily carried out by grouping all the blocks, in which the antenna spans, into one single block.

The AP blocks can be made of two possible geometries: i) with the antenna; ii) without the antenna. Since the regular CBFM enables the analysis of only one location in each simulation, an appropriate setup must be carried out to avoid unnecessary computation.

The equations system is built considering both configurations for the AP blocks at the same time yielding an augmented impedance matrix. It is important to remark that as a consequence of considering both configurations for the AP blocks, the CBFs for those blocks must be also computed for both block geometries. For the sake of clarity, the MS blocks are numbered from 1 to M while the AP blocks ranges from $R+1$ to $R+S$ for cases without antenna and from $R+S+1$ to $R+2S$ for configurations with antenna.

The augmented matrix contains the interaction among the MS blocks (subindex M), the AP blocks without the antenna (subindex P), and the AP blocks with the antenna (subindex P'):

$$\mathbf{Z}_a^{(1)} = \begin{pmatrix} \mathbf{Z}_{MM} & \mathbf{Z}_{MP} & \mathbf{Z}_{MP'} \\ \mathbf{Z}_{PM} & \mathbf{Z}_{PP} & \mathbf{Z}_{PP'} \\ \mathbf{Z}_{P'M} & \mathbf{Z}_{P'P} & \mathbf{Z}_{P'P'} \end{pmatrix}, \tag{2}$$

where the subscript a stands for "augmented" and the submatrices contain the interactions due to the corresponding blocks, i. e.:

$$\mathbf{Z}_{\alpha\beta} = \begin{pmatrix} \mathbf{Z}_{a,b}^{(1)} & \mathbf{Z}_{a,b+1}^{(1)} & \cdots & \mathbf{Z}_{a,b+d}^{(1)} \\ \mathbf{Z}_{a+1,b}^{(1)} & \mathbf{Z}_{a+1,b+1}^{(1)} & \cdots & \mathbf{Z}_{a+1,b+d}^{(1)} \\ \vdots & \vdots & \ddots & \vdots \\ \mathbf{Z}_{a+c,b}^{(1)} & \mathbf{Z}_{a+c,b+1}^{(1)} & \cdots & \mathbf{Z}_{a+c,b+d}^{(1)} \end{pmatrix}, \tag{3}$$

where α and β can be equal to M, P or P'. The blocks involved in each submatrix, can be easily computed considering the aforementioned scheme numbering for the blocks. In addition, we provide the Tables 1a and 1b that present the values for the indexes a, c and b, d for each possible combination of α and β.

Contrary to the common uses of the partial solving techniques, the augmented matrix contains blocks that are overlapped, i.e., a block corresponding to a piece of geometry and another one corresponding to the same geometry but with the antenna, and, therefore, it is expected to be singular (or at least with a high condition number) yielding a meaningless solution. Nevertheless, as we will see, we never employ the entire matrix to acquire the final solution.

Table 1a: Values of a and c for (3)

	a	c
$\alpha = M$	1	$R-1$
$\alpha = P$	$R+1$	$S-1$
$\alpha = P'$	$R+S+1$	$S-1$

Table 1b: Values of b and d for (3)

	b	d
$\beta = M$	1	$R-1$
$\beta = P$	$R+1$	$S-1$
$\beta = P'$	$R+S+1$	$S-1$

After computing (2), the IGJE is applied until finishing the first M blocks, which corresponds to the MS blocks, so that the augmented matrix becomes:

$$\tilde{\mathbf{Z}}_a^{(1)} = \begin{pmatrix} \mathbf{I} & \tilde{\mathbf{Z}}_{MP} & \tilde{\mathbf{Z}}_{MP'} \\ 0 & \mathbf{Z}_{PP} & \mathbf{Z}_{PP'} \\ 0 & \mathbf{Z}_{P'P} & \mathbf{Z}_{P'P'} \end{pmatrix}, \qquad (4)$$

where $\mathbf{I}$ is the identity matrix and the tilde symbol ~ marks that the submatrix has been modified by the application of the IGJE.

Once the previous stage has been finished, the rows and columns related to the entries of the block with and without antenna (labelled with a prime or not, respectively, in Fig. 3) can be swapped to consider the solution for a particular position. For example, if we want to solve the configuration where the second AP block contains the antenna and the other AP blocks are antenna-free, we swap the rows and columns of the corresponding positions (see Fig. 3b). After that, the IGJE can be resumed in order to solve the following S blocks and, thus, to obtain the solution for the given position. This step can be repeated once and again for each block in order to obtain the solution for each position. It is important to notice that we are only solving the first $R+S$ blocks (possibly reordered) of the augmented matrix and, therefore, the solution is not expected to be singular as for the entire augmented matrix.

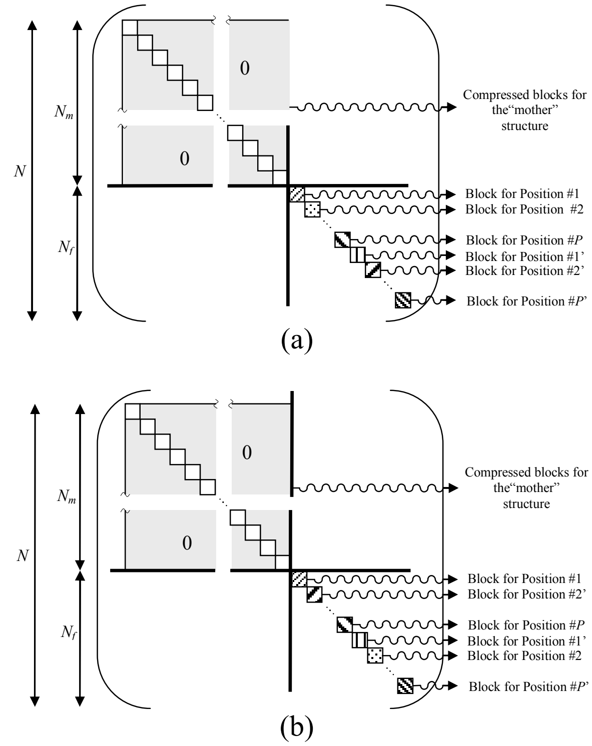

Fig. 3. IGJE application to the positioning of antennas. For the sake of clarity, off-diagonal blocks have been omitted. The primed positions indicate that the block contains the antenna:
a) block status after the first stage of the IGJE;
b) block status before resuming the IGJE for analyzing the antenna in position #2.

Regarding the overall accuracy of the method, it is important to observe that the method will yield the same results as the conventional CBFM as it can be inferred from the previous description. Hence, the accuracy of the method is only limited by the accuracy of the CBFM which has been widely demonstrated in the literature [18-22].

IV. NUMERICAL RESULTS

In this section, we firstly validate the IGJE algorithm in order to study its capacities for the design of antennas by optimizing a reconfigurable antenna. Next, the application of the partial solution of MoM matrices to electrically large structures is illustrated through the analysis of

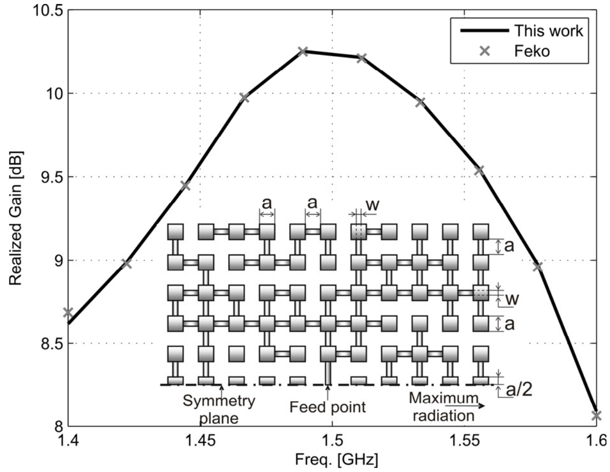

Fig. 4. Realized gain on the design band for the reconfigurable antenna.

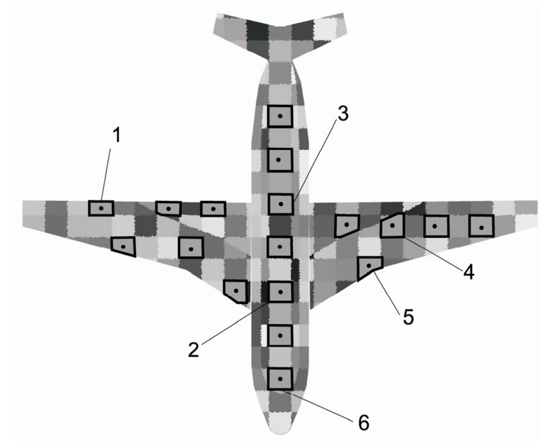

Fig. 5. Block partitioning of the airplane. The border of the blocks containing the possible location of the monopole has been highlighted.

different emplacements of a VHF monopole antenna on an airplane with the objective of finding the optimum positioning.

The times shown in this section correspond to the execution of the code on a CPU AMD Opteron® at 2.4 GHz. Rao-Wilton-Glisson (RWG) basis functions are used to expand the currents.

A. Antenna optimization with the incomplete Gauss-Jordan elimination

This example deals with the design of a reconfigurable antenna to radiate in a given direction. The antenna is based on the model presented in [23] and it consists of a free-standing symmetric array of square patches (see Fig. 4) that can be connected by strips ($a = 90$mm; $w = 30$mm) yielding 2^{104} possible combinations. The existence or absence of connections between patches affects the maximum radiation direction enabling multiple radiation pattern configurations.

The *mother structure* consists of the patches ($N_m = 2429$) and the feeding strip, while the additions region is formed by the rest of the strips ($N_f = 624$). The incomplete solution for the *mother structure* consumes 209 s. After that, the analysis of a certain configuration takes 1.58 s in the average case (calculated over 1000 runs) and 13.95 s in the worst case (all patches connected). The LU decomposition for the best case (no strips) spends 16.23 s. The antenna is optimized by using a genetic algorithm to radiate in the endfire direction in the band 1.4-1.6 GHz. Figure 4 shows the obtained configuration and the realized gain (the gain including the mismatch [23]) with a very good agreement with the commercial software Feko [24].

B. Monopole positioning on an aircraft

In order to illustrate the capabilities of the combination of the CBFM with the partial solving scheme in the context of electrically large structures, we will consider the positioning of a VHF $\lambda/4$ monopole at 120MHz on an airplane-like geometry (length of 50.8 m and wingspan of 61 m). The model is discretized using 66,476 RWG basis functions, so the regular MoM application is not feasible.

In order to apply the CBFM, the airplane is fragmented into 247 blocks and we choose 18 possible blocks to contain the monopole antenna. Seven of the 18 blocks are chosen along the highest part of the fuselage of the airplane since more equilibrated radiation patterns are expected on these positions. The remainder eleven blocks are chosen on the wings in order to also check the performance of the monopole on them. This partitioning as well as the antenna positions are depicted in Fig. 5. The CBFs generation is carried out illuminating each block with 400 plane waves and applying a SVD threshold of 10^{-2}.

If we consider the analysis of the CBFM for a single antenna, e.g. position #2 in Fig. 5, the

CBFM reduces the problem to 9145 unknowns and it is solved in 6522 s. Thus, the study for all the locations with the CBFM would require approximately 117,396 s.

On the other hand, if the problem is solved for all the 18 locations of the monopole in a single analysis with the locally modified CBFM plus the IGJE, it results in a total number of unknowns of 10,175 (the increment with respect to 9145 is due to the duplication of the AP blocks). In this case, the number of unknowns belonging to the *mother structure* (the airplane without the blocks with a possible location of the monopole) is $N_m = 8383$.

The total time until reaching the partial solution corresponding to the *mother structure* – i.e., CBFs generation, matrix filling and first N_m steps of the IGJE– is 16,430 s. After that, each position can be analyzed in only 30 s and, therefore, the total time to analyze the 18 positions is 16,970 s. The computational times for both strategies as well as the time for analyzing 18 monopole positions with the CBFM are detailed in Table 2.

The radiation patterns are shown in Fig. 6 for the six positions numbered in Fig. 5 together with the results provided by Feko in order to validate the accuracy of the radiation patterns. It is important to remark that all the possible locations of the antenna are on the upper part of the fuselage and wings in order to provide coverage during the taxiing on the ground. Thus, a mask of $\pm 30^o$ has been plotted in the elevation patterns to facilitate the graphical inspection. According to this mask, the most suitable diagram is the one corresponding to placing the antenna on the nose (position #6).

V. CONCLUSIONS AND DISCUSSION

The partial solving techniques available in the literature have been traditionally limited to electrically small structures because they need to deal with the entire MoM matrix. In this paper, we have presented a new partial solving technique based on the incomplete Gauss-Jordan elimination scheme and its extension to face electrically large problems. This extension has been carried out by combining the IGJE with the expansion of the currents by means of characteristic basis functions. Then, the number of unknowns is considerably reduced so the matrix can be efficiently manipulated in order to store and solve the MoM equations system. This fact together with the CBFM block partitioning have been exploited to efficiently analyze multiple given configurations of a certain set of blocks (*inter-block* strategy). The applicability of the IGJE plus the CBFM has been illustrated by considering the evaluation of positioning an antenna at multiple locations of an airplane, and has proven to be a highly efficient technique for optimization problems involving electrically large structures.

Table 2: Computational times for the analysis of the on-board VHF monopole on an airplane using the conventional CBFM and the modified CBFM

	CBFM 1 monopole	CBFM 18 monopoles	CBFM+IGJE 18 monopoles
CBFs generation	2635 s	2635 s × 18	2828 s
Matrix filling	3265 s	3265 s × 18	3863 s
LU factorization	622 s	622 s × 18	-
IGJE 1st stage	-	-	9739 s
IGJE 2nd stage	-	-	30 s × 18= 540s
Total time	6522 s	6522 s × 18 = 117,396 s	16,970 s

The future research lines are focused on including the multilevel formulation with the aim of dealing with even larger problems. The authors are also working in the effective modification of the content inside a block (intra-block strategy) in order to make possible the fine-tuning of the position of the antenna.

ACKNOWLEDGMENT

This work has been supported by Ministerio de Ciencia e Innovación of Spain /FEDER under projects TEC2008-01638/TEC (INVEMTA) and CONSOLIDER-INGENIO CSD2008-00068 (TERASENSE); by Unión Europea-Fondo Europeo de Desarrollo Regional under project EQP06-015; and by Cátedra Telefónica-Universidad de Oviedo.

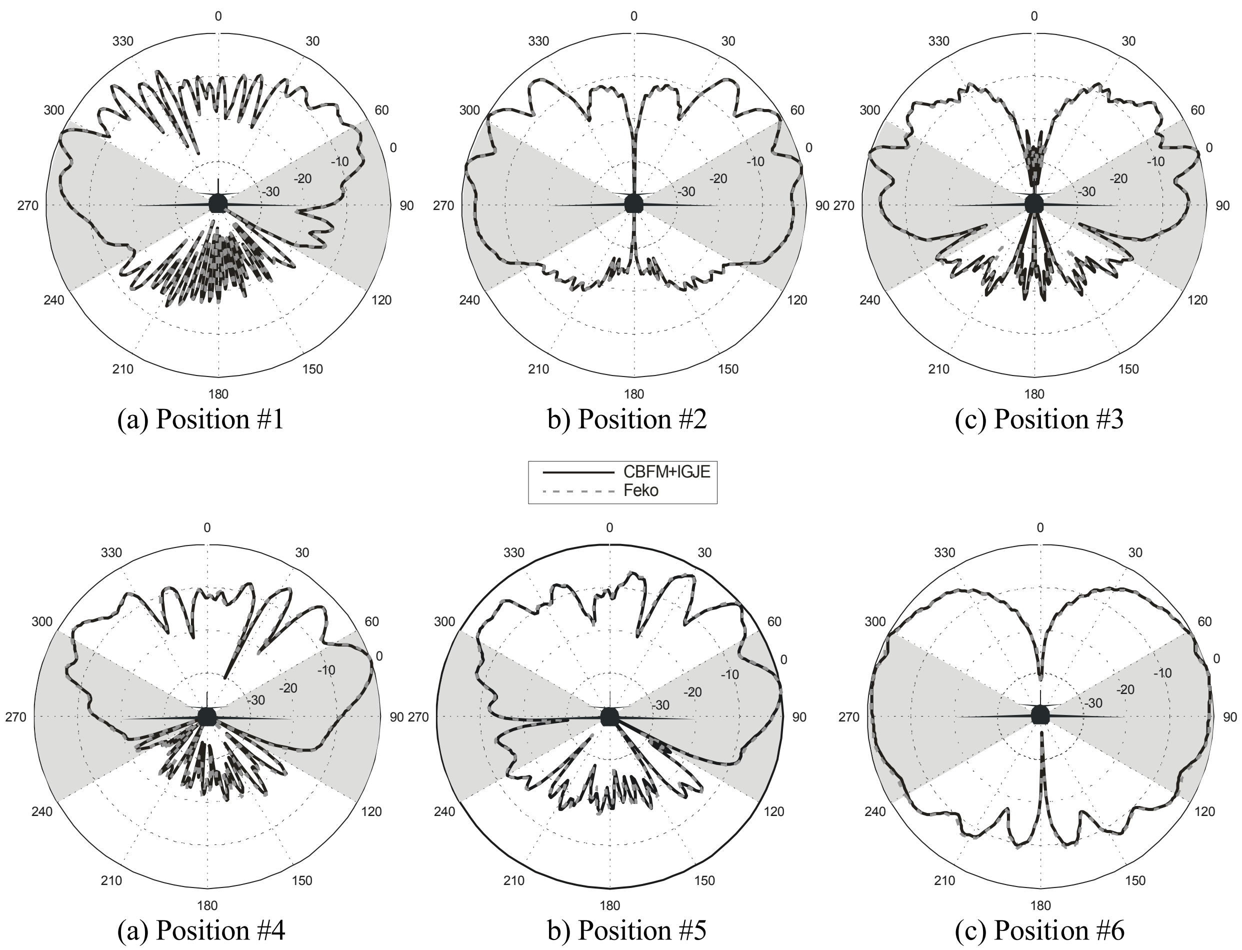

Fig. 6. Normalized radiation pattern in the roll-plane for different antenna locations. The position number corresponds to patterns of Fig. 5.

REFERENCES

[1] R. Kastner, "On matrix partitioning, the Sherman-Morrison-Woodbury technique and the add-on method," *Antennas and Propagation Society International Symposium*, 1989. AP-S. Digest, pp. 15–18, vol.1, Jun. 1989.

[2] R. Kastner, "An 'add-on' method for the analysis of scattering from large planar structures," *IEEE Trans. Antennas and Propagation*, vol. 37, no. 3, pp. 353-361, Mar. 1989.

[3] R. Kastner, "Analysis of microstrip antenna structures using the 'add-on' technique," *IEEE Trans. Antennas and Propagation*, vol. 38, no. 1, pp. 114-117, Jan. 1990.

[4] K. Naishadham and P. Misra, "Order recursive method of moments (ORMoM) for iterative design applications," *IEEE Trans. Microwave Theory Tech.*, vol. 44, no. 12, pp. 2595-2604, Dec. 1996.

[5] P. Misra and K. Naishadham, "Order-recursive Gaussian elimination (ORGE) and efficient CAD of microwave circuits," *IEEE Trans. Microwave Theory Tech.*, vol. 44, no. 12, pp. 2166-2173, Dec. 1996.

[6] L. Alatan, M. Aksun, K. Lablebicioglu, and M. Birand, "Use of computationally efficient method of moments in the optimization of printed antennas," *IEEE Trans. Antennas and Propagation*, vol. 47, no. 4, pp. 725-732, Apr. 1999.

[7] J. M. Johnson and Y. Rahmat-Samii, "Genetic algorithms and method of moments (GA/MoM) for the design of printed antennas," *IEEE Trans. Antennas and Propagation*, vol. 47, no. 10, pp. 1606-1614, Oct. 1999.

[8] D. Cormos, R. Loison, and R. Gillard, "A multistructure method of moments for EM optimizations," *Microwave Opt. Technol. Letters*, vol. 40, no. 2, pp. 114-117, Jan. 2004.

[9] D. Cormos, R. Loison, and R. Gillard, "Fast optimization and sensitivity analysis of nonintuitive planar structures," *IEEE Trans. Microwave Theory Tech.*, vol. 53, no. 6, pp. 2019-2025, Jun. 2005.

[10] F. Obelleiro, J. M. Taboada, J. L. Rodríguez, and J. M. Bertolo, "HEMCUVI: a software package for the electromagnetic analysis and design of radiating systems on board real platforms," *IEEE Antennas and Propagation Mag.*, vol. 44, no. 5, pp. 44-61, Oct. 2002.

[11] E. Koper, W. Wood, and S. Schneider, "Aircraft antenna coupling minimization using genetic algorithms and approximations," *IEEE Trans. Aerospace and Electronic Systems*, vol. 40, no. 2, pp. 742–751, 2004.

[12] R. Coifman, V. Rokhlin, and S. Wandzura, "The fast multipole method for the wave equation: A pedestrian prescription," *IEEE Antennas and Propagation Mag.*, vol. 53, no. 3, pp. 7–12, Jun. 1993.

[13] A. Thain, G. Peres, J.-P. Estienne, G. Sylvand, P. Cailleu, P. Benjamin, I. Terrasse, G.-P. Piau, and G. Sabanowski, "Numerical modelling of aircraft antenna installations," *EuCAP 2007. The Second European Conference on, Antennas and Propagatio,n* pp. 1–6, Nov. 2007.

[14] M. Heckler and A. Dreher, "Analysis of planar 4x4 microstrip antenna arrays installed on airframes," *EuCAP 2007. The Second European Conference on, Antennas and Propagation,* pp. 1–5, Nov. 2007.

[15] C. Penwell, "Prediction of VHF radiation patterns on gulfstream aircraft," *Wireless Communications and Applied Computational Electromagnetics, 2005. IEEE/ACES International Conference on*, pp. 519–522, Apr. 2005.

[16] A. Barka and P. Caudrillier, "Domain decomposition method based on generalized scattering for installed performance of antennas on aircraft," *IEEE Trans. Antennas and Propagation*, vol. 55, no. 6, pp. 1833–1842, Jun. 2007.

[17] E. Lucente, R. Mittra, and A. Monorchio, "An efficient procedure to analyze locally-modified scattering problems by using the characteristic basis function method," *Antennas and Propagation Society International Symposium, AP-S 2008. IEEE*, pp. 1–4, Jul. 2008.

[18] R. Mittra, "Characteristic Basis Function Method (CBFM) – An Iteration-free Domain Decomposition Approach in Computational Electromagnetics," *Applied Computational Electromagnetic Society* (*ACES) Journal*, vol. 24, no. 2, pp. 204-223, 2009.

[19] R. Maaskant, R. Mittra, and A. Tijhuis, "Fast Solution of Multi-Scale Antenna Problems for the Square Kilometre Array (SKA) Radio Telescope using the Characteristic Basis Function Method (CBFM)," *Applied Computational Electromagnetic Society (ACES) Journal*, vol. 24, no. 2, pp. 174-188, 2009.

[20] E. Lucente, A. Monorchio, and R. Mittra, "An iteration-free MoM approach based on excitation independent characteristic basis functions for solving large multiscale electromagnetic scattering problems," *IEEE Antennas and Propagation Mag.*, vol. 56, no. 4, pp. 999–1007, Apr. 2008.

[21] C. Delgado, M. F. Cátedra, and R. Mittra, "Application of the characteristic basis function method utilizing a class of basis and testing functions defined on NURBS patches," *IEEE Trans. Antennas and Propagation*, vol. 56, no. 3, pp. 784–791, Mar. 2008.

[22] J. Laviada, M. R. Pino, F. Las-Heras, and R. Mittra, "Solution of electrically large problems with multilevel characteristic basis functions," *IEEE Trans. Antennas and Propagation*, vol. 57, no. 10, pp. 3189–3198, Oct. 2009.

[23] L. Pringle, P. H. Harms, S. P. Blalock, G. N. Kiesel, E. J. Kuster, P. G. Friederich, R. J. Prado, J. M. Morris, and G. Smith, "A reconfigurable aperture antenna based on switched links between electrically small metallic patches," *IEEE Trans. Antennas and Propagation*, vol. 52, no. 6, pp. 1434–1445, Jun. 2004.

[24] *Feko User's manual*, EM Software & Systems, 2008, http://www.feko.info/.

Jaime Laviada was born in Gijón, Spain, in 1982. He received the degree in Ingeniería de Telecomunicación and Ph.D. from the Universidad de Oviedo, Spain, in 2005 and 2010, respectively. In 2006, he joined the Área de Teoría de la Señal y Comunicaciones, Universidad de Oviedo. He has been a Visiting Scholar in the Electromagnetics and Communications Laboratory of the Pennsylvania State University, University Park, during 2007 and 2008. His main research interests are in numerical efficient techniques and antenna pattern synthesis.

Javier Gutiérrez-Meana was born in Gijón, Spain, in 1982. He received his M.S. and Ph.D. degrees in electrical engineering from the University of Oviedo (Spain) in 2005 and 2010, respectively. He joined the R and D department of CTIC Foundation in 2005, and since 2006, he is a Research Assistant with the Area of Theory of Signal and Communications (University of Oviedo). He was a Visiting Researcher at The Gordon CenSSIS – Northeastern University (Boston) in 2008. His interests and research studies are focus on the evaluation of electromagnetic coverage in rural/urban electrically large scenarios by means of high frequency techniques.

Marcos Rodríguez Pino was born in Vigo, Spain, in 1972. He received the M.Sc. and Ph.D. degrees in electrical engineering from the University of Vigo, Vigo, Spain, in 1997 and 2000, respectively. Since 2001, he is with the Electrical Eng. Department, University of Oviedo, where he currently is Associate Professor teaching courses on electromagnetic fields. During 1998, he was a Visiting Scholar at the ElectroScience Laboratory, The Ohio State University, Columbus, OH. From 2000 to 2001, he was Assistant Professor at the University of Vigo. His research areas are radar cross section, rough surface scattering, and applied mathematics for computational electromagnetics.

Fernando Las-Heras was born in Zaragoza, Spain. He received the M.S. degree in 1987 and the Ph.D. degree in 1990, both in telecommunication engineering, from the Universidad Politécnica de Madrid (UPM). From 1988 to 1990, he was a National Graduate Research Fellow. From 1991 to 2000, he held a position of Associate Professor at the Dept. of Señales, Sistemas y Radiocomunicaciones (Dept. of Signal, Systems and Radiocommunications) of the UPM. From 2001 to 2003, he held a position of Associate Professor at the Dept. de Ingeniería Eléctrica (Dept. of Electrical Engineering) of the Universidad de Oviedo, heading the research group Teoría de la Señal y Comunicaciones (Signal Theory and Communications) at that University. From December 2003, he holds a Full-Professor position at the Universidad de Oviedo where he has been Vice-dean for the Telecommunication Engineering degree at the Escuela Politécnica Superior de Ingeniería de Gijón (Technical School of Engineering at Gijón), Spain. He has been Visiting Researcher at Syracuse University, New York, and Visiting Lecturer at the Universidad Nacional de Ingeniería, Peru, and ESIGELEC, France. He has authored over 200 technical journal and conference papers in the areas of antenna design; the inverse electromagnetic problem with application to diagnostic, measurement, and synthesis of antennas; propagation and computational electromagnetics and engineering education.

Strategies for Improving the Use of the Memory Hierarchy in an Implementation of the Modified Equivalent Current Approximation (MECA) Method

Hipólito Gómez-Sousa[1], José Á. Martínez-Lorenzo[1], Oscar Rubiños-López[1], Javier G. Meana[2], María Graña-Varela[1], Borja Gonzalez-Valdes[1], and Marcos Arias-Acuña[1]

[1] Department of Signal Theory and Communications
University of Vigo, ETSI de Telecomunicación, Campus Universitario, E-36310 Vigo, Spain
{hgomez, oscar}@com.uvigo.es

[2] Department of Electrical Engineering
University of Oviedo, Edificio Polivalente de Viesques, Campus Universitario, E-33203 Gijón, Spain

Abstract **─** In this paper, we investigate different techniques for improving the cache memory use when running a parallel implementation of the modified equivalent current approximation (MECA) method. The MECA method allows the analysis of dielectric and lossy geometries, and reduces to the well-studied physical optics (PO) formulation in case of PEC scatterers. We discuss several memory-hierarchy-based optimization techniques and present how to implement them in C. We show through simulations that these optimization strategies are effective for reducing the total execution time when calculating the scattered fields with a parallel implementation of the MECA method.

Index Terms **─** Memory-hierarchy-based optimization, parallel programming, physical optics (PO).

I. INTRODUCTION

Physical optics (PO) is a well-known asymptotic high frequency computational technique that is widely used in computing the electromagnetic scattering from electrically large and complex structures [1, 2]. In contrast to full wave methods, like the method of moments (MoM), PO does not need a huge amount of computational resources to solve these problems with a high degree of accuracy and efficiency.

The modified equivalent current approximation (MECA) method [3, 4] has extended PO to lossy materials with a complex effective permittivity by calculating the equivalent electric and magnetic currents based on the oblique incidence of a plane wave on the interface, together with a field decomposition into TE and TM components. Unlike the method of stationary phase, the surface is discretized into flat triangular facets where the current distribution has constant amplitude and linear phase variation. As a consequence, the radiation integral can be solved analytically and so problems which are prohibitive for full-wave simulation, especially at very high frequencies, are successfully modelled by MECA.

On the other hand, we have witnessed the emergence and sustained growth and improvement of high-speed and high-capacity personal computers during the last years. New programming paradigms can be used in order to improve the performances of the computational techniques (MPI, OpenMP). Two recent papers [5, 6] have analyzed parallel implementations of electromagnetic modeling codes which have been tested on several high-performance computer systems. To reduce the total runtime of MECA, we have also developed a parallel version of the code. We have selected an OpenMP paradigm because it can be applied in shared memory machines. In addition, we have implemented memory-hierarchy-based optimization techniques [10, 11] in our code.

In this paper, we demonstrate the usefulness of employing all these computational techniques to take advantage of the new computational resources available in personal computers. The main content of this paper is divided as follows. Section II gives an overview of the MECA method and briefly explains our parallel algorithm. In Section III, the proposed techniques for improving the use of the memory hierarchy are addressed. Afterwards, performance results obtained through simulations are presented in Section IV.

II. PARALLEL IMPLEMENTATION OF MECA

A. The MECA method

In the MECA method, the equivalent magnetic and electric current densities at the barycenter of each facet are calculated according to the following two equations respectively:

$$\mathbf{M_{i0}} = E_{TE}^{i}\left(1+R_{TE}\right)\left(\hat{\mathbf{e}}_{\mathbf{TE}}\times\hat{\mathbf{n}}_{\mathbf{i}}\right)+ \\ +E_{TM}^{i}\cos(\theta_i)\left(1+R_{TM}\right)\hat{\mathbf{e}}_{\mathbf{TE}}\Big|_{S_i}, \tag{1}$$

$$\mathbf{J_{i0}} = \frac{E_{TE}^{i}}{\eta_1}\cos(\theta_i)\left(1-R_{TE}\right)\hat{\mathbf{e}}_{\mathbf{TE}}+ \\ +\frac{E_{TM}^{i}}{\eta_1}\left(1-R_{TM}\right)\left(\hat{\mathbf{n}}_{\mathbf{i}}\times\hat{\mathbf{e}}_{\mathbf{TE}}\right)\Big|_{S_i}, \tag{2}$$

where η_1 is the impedance of the medium of incidence, and R_{TE} (R_{TM}) is the TE (TM) reflection coefficient. For the expressions of R_{TE} and R_{TM}, see [4, 12]. As shown in Fig. 1, $\mathbf{E_{TE}^{i}} = E_{TE}^{i}\hat{\mathbf{e}}_{\mathbf{TE}}$ and $\mathbf{E_{TM}^{i}} = E_{TM}^{i}\hat{\mathbf{e}}_{\mathbf{TM}}$ are the TE and TM components of the incident electric field at the barycenter of surface S_i, $\hat{\mathbf{p}}_{\mathbf{i}}$ is a unit vector pointing in the propagation direction of the incident wave, θ_i is the angle of incidence, and $\hat{\mathbf{n}}_{\mathbf{i}}$ is the outward unit normal vector to the triangular patch S_i. The first medium is characterized by its constitutive parameters: permittivity ε_1, permeability μ_1, and conductivity σ_1. Similarly, the second medium is characterized by $(\varepsilon_2,\ \mu_2,\ \sigma_2)$.

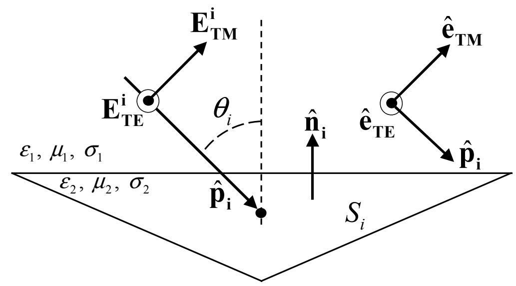

Fig. 1. Oblique wave incidence on a triangular facet S_i.

After obtaining $\mathbf{M_{i0}}$ and $\mathbf{J_{i0}}$, an analytical solution for the radiation integral at the observation point $\mathbf{r_k}$, located in the far field of each triangular patch, can be derived. The scattered electric field $\mathbf{E_k^s}$ at $\mathbf{r_k}$ due to the contribution of all the facets i of a given mesh geometry can be stated as [13]:

$$\mathbf{E_k^s} = \frac{j}{2\lambda}\sum_i \frac{e^{-jk_1 r_{ik}}}{r_{ik}}\left[\mathbf{E_{ik}^a} - \eta_1 \mathbf{H_{ik}^a}\times\hat{\mathbf{r}}_{\mathbf{ik}}\right], \tag{3}$$

where λ is the wavelength, k_1 is the wave number in the medium of incidence, and $\mathbf{r_{ik}} = r_{ik}\hat{\mathbf{r}}_{\mathbf{ik}}$ is the position vector from the barycenter $\mathbf{r_i}$ of the i-th facet to the observation point $\mathbf{r_k}$. Figure 2 summarizes the notation for the position vectors involved in the scattering calculations throughout this paper.

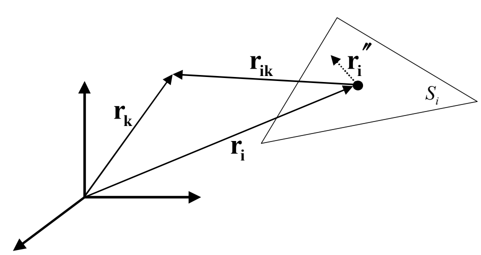

Fig. 2. Facet S_i, observation point $\mathbf{r_k}$ and the corresponding position vectors. $\mathbf{r_i}''$ is a variable vector from barycenter $\mathbf{r_i}$ to any point on S_i.

Assuming that the currents have constant amplitude and linear phase variation depending on the direction of propagation $\hat{\mathbf{p}}_{\mathbf{i}}$ of the incident wave, the vector values $\mathbf{E}^{\mathbf{a}}_{\mathbf{ik}}$ and $\mathbf{H}^{\mathbf{a}}_{\mathbf{ik}}$ in Eq. (3) can be calculated as [4]:

$$\mathbf{E}^{\mathbf{a}}_{\mathbf{ik}} = (\hat{\mathbf{r}}_{\mathbf{ik}} \times \mathbf{M}_{\mathbf{i0}}) I_i(\hat{\mathbf{r}}_{\mathbf{ik}}), \quad (4)$$

$$\mathbf{H}^{\mathbf{a}}_{\mathbf{ik}} = (\hat{\mathbf{r}}_{\mathbf{ik}} \times \mathbf{J}_{\mathbf{i0}}) I_i(\hat{\mathbf{r}}_{\mathbf{ik}}), \quad (5)$$

where $\mathbf{M}_{\mathbf{i0}}$ and $\mathbf{J}_{\mathbf{i0}}$ are the current densities in Eqs. (1) and (2), and $I_i(\hat{\mathbf{r}}_{\mathbf{ik}})$ is an integral given by:

$$I_i(\hat{\mathbf{r}}) = \int_{S_i} e^{jk_1(\hat{\mathbf{r}}-\hat{\mathbf{p}}_{\mathbf{i}})\cdot\mathbf{r}_{\mathbf{i}}''} ds_i. \quad (6)$$

$\mathbf{r}_{\mathbf{i}}''$ denotes a vector from the barycenter $\mathbf{r}_{\mathbf{i}}$ of the i-th facet to the source points on the triangular surface S_i (see Fig. 2). In the particular case that the observation point $\mathbf{r}_{\mathbf{k}}$ is in the absolute far field of the whole structure, then $\hat{\mathbf{r}}_{\mathbf{ik}} \approx \hat{\mathbf{r}}_{\mathbf{k}}$ and $r_{ik} \approx r_k$ for all the values of i, resulting:

$$\mathbf{E}^{\mathbf{a}}_{\mathbf{ik}} = e^{jk_1\hat{\mathbf{r}}_{\mathbf{k}}\cdot\mathbf{r}_{\mathbf{i}}} (\hat{\mathbf{r}}_{\mathbf{k}} \times \mathbf{M}_{\mathbf{i0}}) I_i(\hat{\mathbf{r}}_{\mathbf{k}}), \quad (7)$$

$$\mathbf{H}^{\mathbf{a}}_{\mathbf{ik}} = e^{jk_1\hat{\mathbf{r}}_{\mathbf{k}}\cdot\mathbf{r}_{\mathbf{i}}} (\hat{\mathbf{r}}_{\mathbf{k}} \times \mathbf{J}_{\mathbf{i0}}) I_i(\hat{\mathbf{r}}_{\mathbf{k}}). \quad (8)$$

The explained current distributions allow modeling with facets larger than those employed in other approaches. This fact implies a computational cost decrease in terms of both time and memory.

The integral in Eq. (6) always has an analytical solution [14]. The method for analytically solving this integral is summarized in Appendix I.

B. Parallel algorithm

In our parallel implementation of the MECA method, each thread computes the scattered fields $\mathbf{E}^{\mathbf{s}}_{\mathbf{k}}$ in a set of observation points $\mathbf{r}_{\mathbf{k}}$, *i.e.*, calculates all the summation terms in (3) for a range of values of k. A thread is a piece of computational work that runs independently. A program is parallel if more than one thread is executed concurrently during a time interval. We have selected the implementation strategy described above, instead of using each thread to compute, for all the observation points, the scattered fields due to a set of facets. As can be seen in Fig. 3, the chosen approach ensures that the threads do not compete for writing in the memory locations which must contain the values of $\mathbf{E}^{\mathbf{s}}_{\mathbf{k}}$ at the end of the parallel program. If each thread were utilized to calculate the contribution of a set of triangular patches, the runtime would be increased because some threads would have to wait to write their partial calculations of $\mathbf{E}^{\mathbf{s}}_{\mathbf{k}}$ (see Fig. 3b). These delays could be avoided using private variables for each OpenMP thread in order to store the partial results and, once all the threads have finished executing, employ these partial sums to compute the total values. Nevertheless, this solution can drastically increase the memory usage.

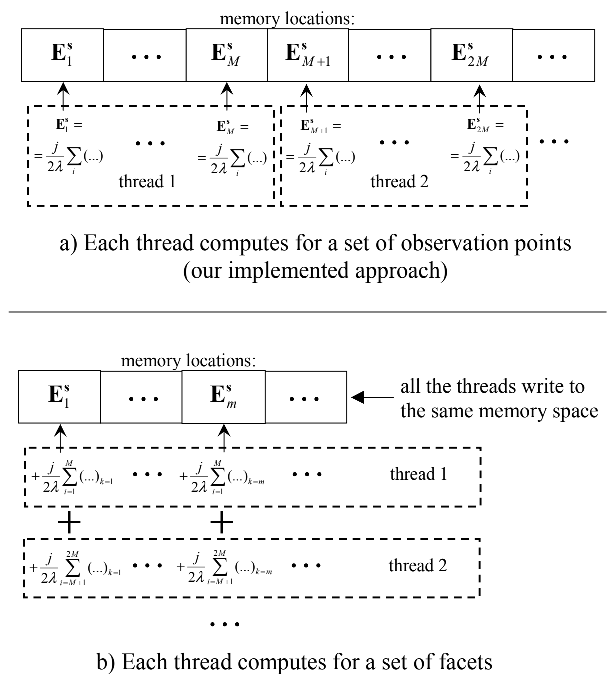

Fig. 3. Different strategies for implementing the parallelization of MECA.

From now on we will use the term "task" to refer to an observation point. When allocating tasks to the threads, first we assign `floor(nr/nth)` tasks to each thread, where `nr` denotes the total number of tasks and `nth` represents the number of threads. Each of the remaining `nr-nth*floor(nr/nth)` tasks is allocated to a single thread. As a consequence, in general, some threads compute

`M=floor(nr/nth)` tasks, whereas others compute `M=floor(nr/nth)+1` tasks.

In our parallel version of the MECA method, each thread runs two main nested *for* loops. The outer loop goes through each observation point (index k in (3)), while the inner one goes through each facet (index i in (3)).

We have chosen the OpenMP paradigm because it provides a portable application programming interface (API) for high-performance parallel programs on shared-memory platforms. In general, OpenMP has better performance on symmetric multiprocessing (SMP) systems than MPI [15]. An SMP system involves a hardware architecture where two or more identical processors are connected to a single shared main memory.

III. MEMORY-HIERARCHY-BASED OPTIMIZATION

A. Loop tiling

Different techniques can be employed to improve the use of the memory hierarchy. One of these techniques is *loop tiling,* whose aim is to increase the reutilization of both instructions and data stored in the cache memory. An improvement in cache data reuse reduces time spent on transferring data from the main memory to the cache and vice versa. Figure 4 and the pieces of C code in Table 1 exemplify *loop tiling.* The implementation of this technique is simple, and it requires adding a new *for* loop, external to the two original loops, as seen in Table 1.

Without *loop tiling,* all the corresponding inner iterations are executed at each outer iteration. On the contrary, if *loop tiling* is applied, only a number `block_size` of original inner iterations are executed per outer loop iteration, as Fig. 4 shows. Once the outer loop iterations are completed, they are executed again for the next blocks of consecutive inner iterations. In our particular case, the blocks of `block_size` inner iterations of a complete run of the outer loop correspond to the same facets. As a consequence, *loop tiling* produces reutilization of instructions and loaded cache data shared by blocks of inner iterations, thus reducing the amount of data moving between the cache and the main memory.

The value of the integer parameter `block_size` which minimizes the execution time must be empirically determined for a particular program and computer. If `block_size` is too large, each iteration of the outer loop could not fit on the cache, preventing total data reutilization and forcing additional cache loads. On the other hand, if `block_size` is too small, there is a certain amount of space not used in the cache for data reutilization, and this fact leads the cache memory to be unnecessarily loaded and unloaded. In order to obtain the optimal value, a set of experimental runs should be executed with a reduced amount of facets. Figure 5 presents the results of our tests for determining the optimal value of `block_size` when the geometry has 2×10^5 facets in the experimental context described in Section IV.

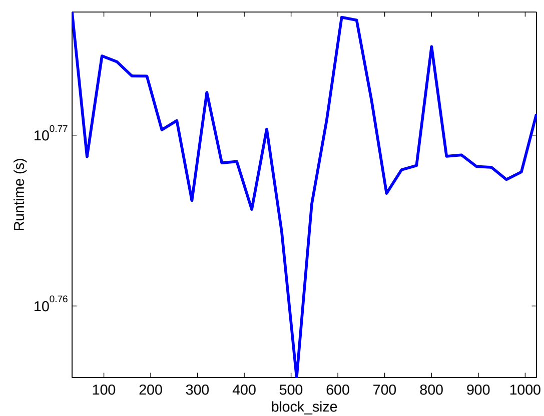

Fig. 5. Runtime vs. `block_size` with 2×10^5 facets. The values of the rest of the parameters can be found in Section IV.

B. Array fusion

Another memory hierarchy based optimization technique is *array fusion*, which consists of defining a single array of `structs` instead of several same-size arrays in the code. In the parallelization of MECA, we regrouped all the arrays which store information relative to the facets: magnetic/electric currents, barycenter points, etc. Let us consider that data is copied from main memory to cache, and back, in blocks of contiguous data. The elements of a `struct` are arranged in the memory in the same order as they are defined; hence, *array fusion* may lower the total data flow from and to the cache. In our case, this technique reduces the execution time because the currents at barycenter i and the coordinates of barycenter i are used together to compute Eqs. (4), (5), (7), and (8). Figure 6 and the two pieces of data declaration code in C which appear in Table 2 illustrate array fusion.

Without *array fusion,* the values of the magnetic and electric currents at a particular barycenter and the vector with the coordinates of that barycenter are never stored in contiguous order in the main memory. Therefore, in this case, at least three accesses to main memory could be necessary to move the needed facet data to the cache in order to compute each term of the summation in Eq. (3). On the contrary, only one access could suffice if *array fusion* is used.

In our MECA parallel implementation, the array which contains the observation points cannot be grouped together with the information relative to the facets in the same array of `structs`. The obvious reason is that the number of observation points is generally different from the amount of facets. Moreover, for a given observation point, Eq. (3) must be computed using the information of all the facets, *i.e.*, with *array fusion*, it would be necessary to define additional fields in each `struct` for storing the coordinates of all the required observation points. Clearly, this solution would lead to a much higher memory usage, and, what is more important, the `struct` so defined could not fit on the cache.

Table 1: Loop tiling implementation

Without *loop tiling:*

```
for (ind1=0; ind1<M; ind1++)
{
/* THIS OUTER LOOP GOES THROUGH */
/* EACH OBSERVATION POINT       */
   for (ind2=0; ind2<N; ind2++) {
   /* THIS INNER LOOP GOES THROUGH EACH FACET */...}}
```

With *loop tiling:*

```
for(ind_tiling=0;ind_tiling<N;ind_tiling+=block_size){
   for (ind1=0; ind1<M; ind1++) {
   /* THIS OUTER LOOP GOES THROUGH */
   /* EACH OBSERVATION POINT       */
      for (ind2=ind_tiling;
           ind2<MIN(ind_tiling+block_size, N);
           ind2++){
           /* THIS INNER LOOP GOES */
           /* THROUGH EACH FACET   */...}}}
```

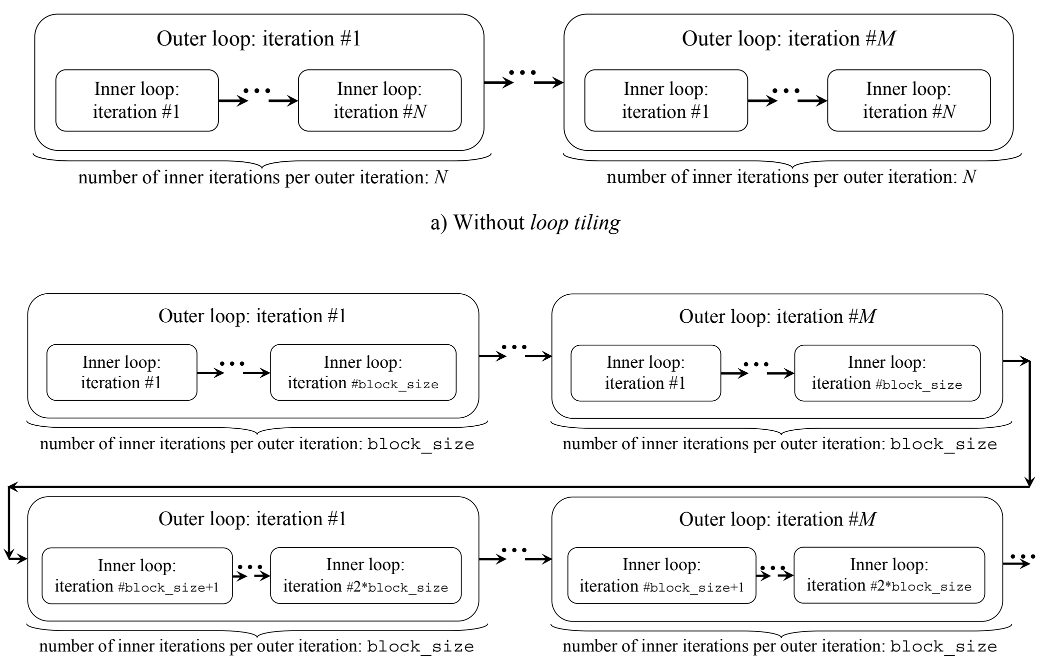

a) Without *loop tiling*

b) With *loop tiling*

Fig. 4. Execution order of the loop iterations. With *loop tiling,* there exists an increase in the reutilization of instructions and loaded cache data shared by blocks of inner iterations.

Table 2: Array fusion implementation

Without *array fusion:*

```
double J_Real[3*N], J_Imag[3*N], M_Real[3*N], M_Imag[3*N],
       Barycenter[3*N];

// For instance, { J_Real[3*i+0], J_Real[3*i+1], J_Real[3*i+2] } are the
// 3 real Cartesian components of the electric current density at
// barycenter i>=0.
// Single-dimensional arrays are used here to ensure that the 3
// components of each vector are contiguous in memory independently of
// the programming language, the compiler and the platform.
```

With *array fusion:*

```
struct reg{
    double J_Real[3], J_Imag[3], M_Real[3], M_Imag[3], Barycenter[3];
}
struct reg v[N];

// With array fusion, for each i the following 3-element arrays are
// contiguous in memory:
// v[i].J_Real, v[i].J_Imag, v[i].M_Real, v[i].M_Imag and
// v[i].Barycenter.
```

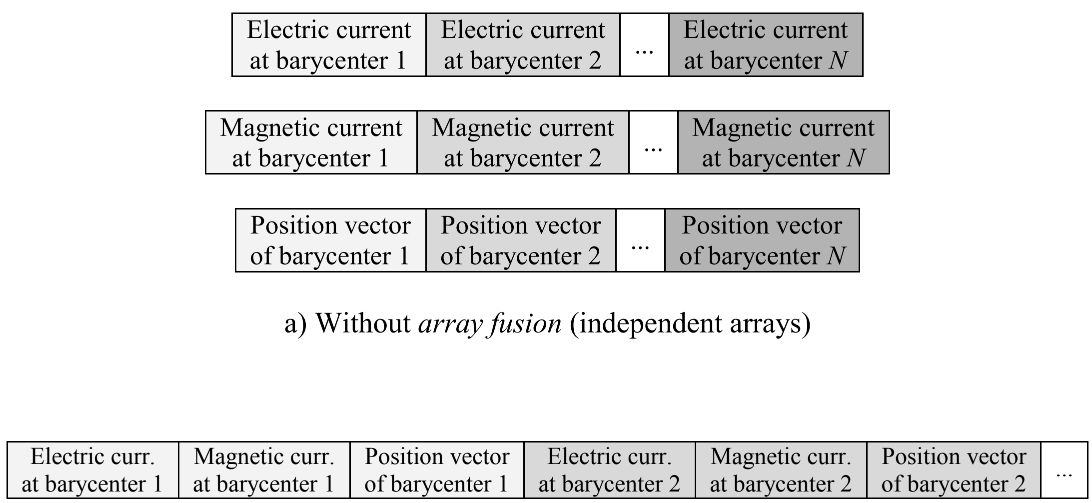

a) Without *array fusion* (independent arrays)

b) With *array fusion* (one array of `structs`)

Fig. 6. Storage order in the main memory. With *array fusion,* all the data relative to each facet is stored contiguously.

C. False-sharing reduction

The cache is subdivided into cache lines which represent the minimum amount of data transferable between cache and main memory. These cache lines are organized into C sets of K lines, as explained in Fig. 7. The content of main memory line X can only be stored in cache set X mod C.

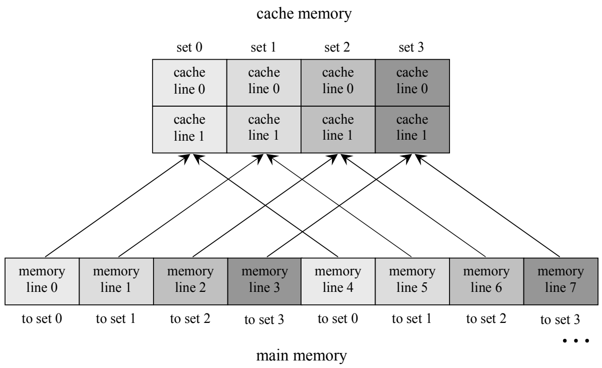

Fig. 7. Example: cache with C=4 sets of K=2 lines each.

When running a parallel application, false sharing occurs when two threads access different data elements in the same cache line for reads and writes. This situation is represented in Fig. 8. This particular problem could seriously degrade the performance of an application because some threads might have to wait until the preceding writing operations in the queue have completed.

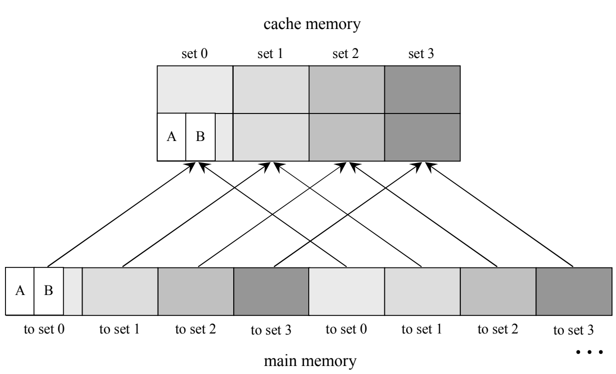

Fig. 8. Example: false sharing occurs when different threads modify variables A and B which reside in the same cache line.

To reduce false sharing, we use the `firstprivate` clause on the OpenMP task `pragma`. This clause declares one or more input variables to be private to a thread, and initializes each of these variables with the value that the corresponding original variable has when the task `pragma` is encountered. As we have seen, the utilization of `firstprivate` in our parallel program increases the performance.

IV. RESULTS

The algorithm for calculating the scattered field in Eq. (3) was implemented in C using the OpenMP library. We ran our parallel algorithm on a server with two Quad-Core Intel® Xeon® processors with 6 MB of L2 cache per processor, yielding a total of eight cores, each core running at 2.66 GHz. The parameter `block_size` was set to the value 512 (the optimal value, presented in Fig. 4), the number of observation points was 722, the maximum number of facets was 5×10^6, and we used 8 threads. A square plate geometry was chosen for our performance tests. Figures 9 and 10 show the total runtime as a function of the number of facets for our parallel implementation with and without all the optimization techniques described in Section III. For comparison, these figures, also, include the total runtime for a MATLAB® single-thread version of the MECA method, *i.e.*, a sequential program version in MATLAB®, without memory-hierarchy-based optimization techniques, executed on the same computer.

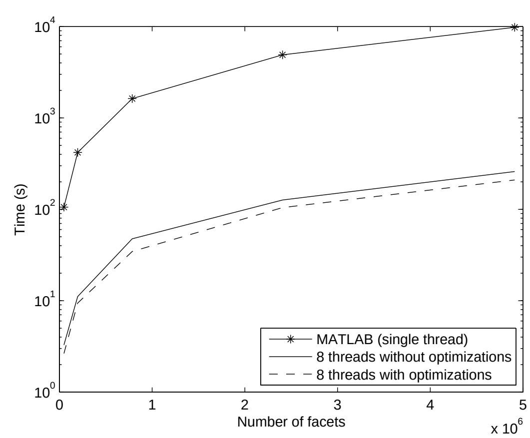

Fig. 9. Runtime vs. number of facets for near-field calculations.

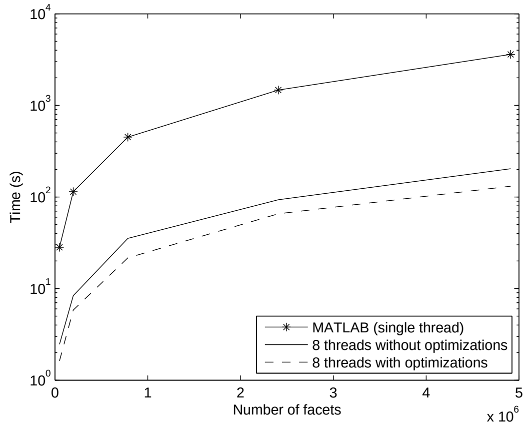

Fig. 10. Runtime vs. number of facets for far-field calculations.

Under the experimental conditions explained above, and employing the `firstprivate` clause, Figs. 11 and 12 show the effect on the runtime of the separate use of *array fusion* and *loop tiling*.

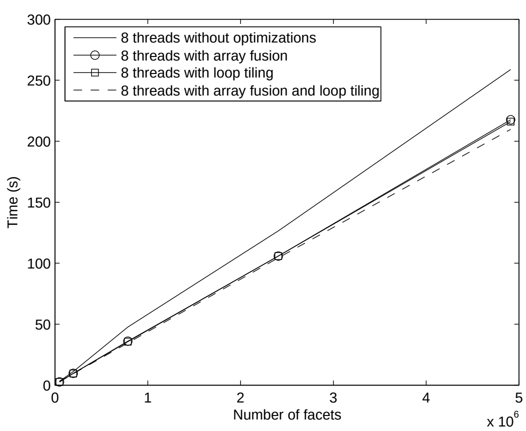

Fig. 11. Runtime vs. number of facets for near-field calculations with the separate use of *array fusion* and *loop tiling*.

The parallel speedup values under the experimental conditions described above were obtained varying the number of threads, up to the number of cores. In our particular case, it was noted that having more threads than cores degrades performance compared to the optimal solution of using as many threads as cores. The experimental speedup is defined by the following formula: $speedup(n \text{ threads}) = \dfrac{runtime(1 \text{ thread})}{runtime(n \text{ threads})}$.

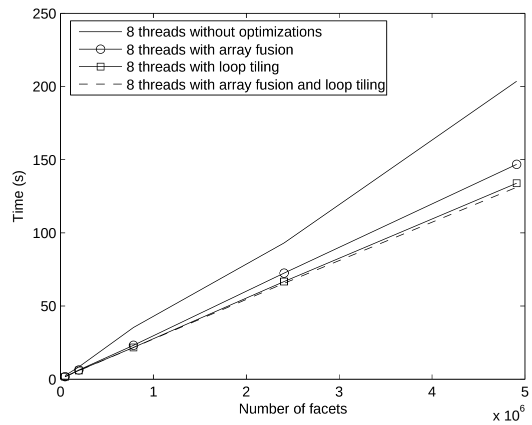

Fig. 12. Runtime vs. number of facets for far-field calculations with the separate use of *array fusion* and *loop tiling*.

The influence of the `firstprivate` clause is represented in Fig. 13.

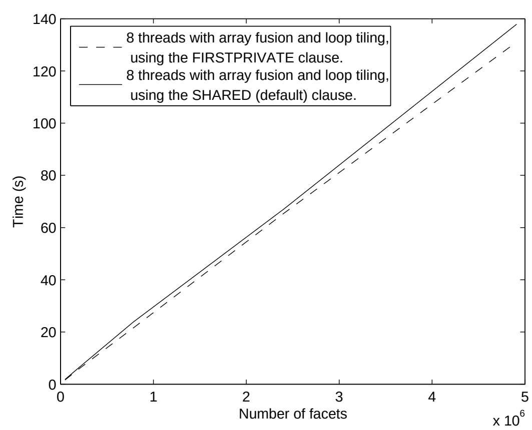

Fig. 13. Runtime vs. number of facets for far-field calculations, with and without the `firstprivate` clause.

The speedup so calculated, up to the number of real cores, allows inferring the scalability of our program, namely the optimal performance behavior of the program as a function of the number of cores.

If *n* threads are used in an ideal scenario with *n* cores, the runtime is reduced by a factor of *n* when compared to the runtime of one thread. The reason is that the total computational load is distributed evenly amongst the threads, and each thread is executed by a core. Then the ideal speedup is simply *speedup*(n threads)=n. In a real scenario, the speedup achieved is lower due to constraints such as the effect of accessing a shared memory or the communication times between threads. In our parallel algorithm, communication between the threads is not performed, but multiple threads simultaneously access the same shared memory.

The scalability obtained through simulations is illustrated in Fig. 14, showing the experimental speedup. Looking at this figure, the excellent scalability of our parallel implementation is clear.

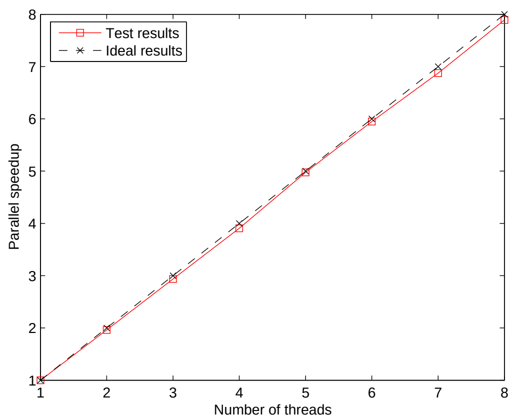

Fig. 14. The experimental speedup as a function of the number of threads (each thread assigned to a real core) for far-field calculations and a scattering problem with 5×10^6 facets.

Finally, Figs. 15 and 16 show a comparison between the far-field results of MECA and MoM. The geometry consists of a square PEC plate whose length is 3 cm, located in the XY plane. The incident field is a plane wave polarized along the direction $\hat{\theta}$, with amplitude 1 V/m, f = 94 GHz, and normal incidence on the interface.

V. CONCLUSION

This paper presents a parallel version of a modified PO method, known as the modified equivalent current approximation (MECA) method, valid for both PEC and dielectric objects. Our experimental results show that the computational performance of this parallel implementation is increased by applying techniques to improve the use of the memory hierarchy. These optimization techniques are simple and easy to understand, and they could be very effective in improving the programmed algorithm performance (either sequential or parallel programs) in many other methods for calculating scattered fields.

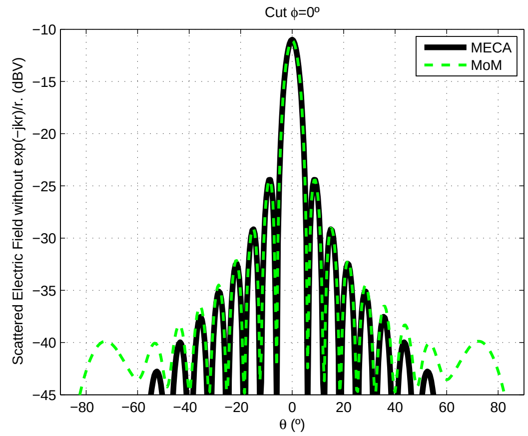

Fig. 15. Comparison between MoM and MECA solutions along the observation cut $\phi = 0^{\circ}$ for a square PEC scatterer of side length 3 cm.

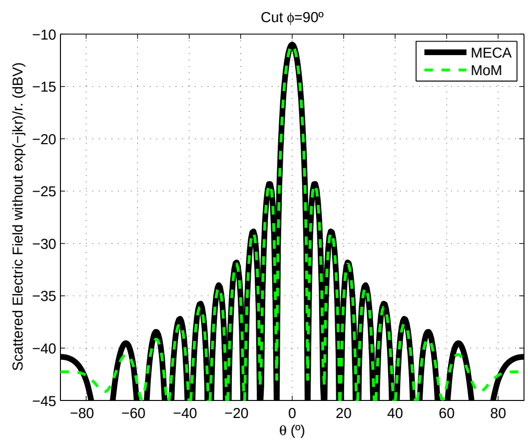

Fig. 16. Comparison between MoM and MECA solutions along the observation cut $\phi = 90^{\circ}$ for a square PEC scatterer of side length 3 cm.

ACKNOWLEDGMENT

This work was supported by the Spanish Government Grants CONSOLIDER-INGENIO 2010 CSD2008-00068 and "Ramón y Cajal" RYC-2009-04180, and by Xunta de Galicia Grant INCITE08PXIB322219PR.

APPENDIX I

In this appendix, we explain how to solve the integral in Eq. (6) using the procedure detailed in [14].

Let us consider a triangular flat patch as seen in Fig. 17. The triangle i is defined by three points $\mathbf{P_1}$, $\mathbf{P_2}$, $\mathbf{P_3}$, and $\mathbf{r_i}$ is a reference point placed at the barycenter ($\mathbf{r_i} = (\mathbf{P_1} + \mathbf{P_2} + \mathbf{P_3})/3$). We define $\mathbf{v_{mn}}$ as the vector $\mathbf{v_{mn}} = \mathbf{P_n} - \mathbf{P_m}$. The normal vector $\hat{\mathbf{n}}$ of the triangle i is defined such that $\mathbf{v_{12}} \times \mathbf{v_{13}} = 2A_i\,\hat{\mathbf{n}}$, as seen in Fig. 17, where A_i is the area of this triangle.

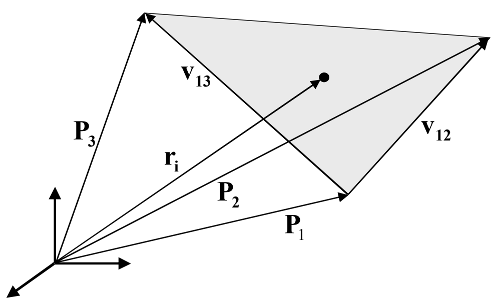

Fig. 17. Triangular patch with barycenter $\mathbf{r_i}$ and vertices $\mathbf{P_1}$, $\mathbf{P_2}$ and $\mathbf{P_3}$.

A coordinate system is used with scalar variables (u,v) such that any point $\mathbf{r_i}''$ on the triangle surface can be described as:

$$\mathbf{r_i}'' = \mathbf{P_1} - \mathbf{r_i} + u\cdot\mathbf{v_{12}} + v\cdot\mathbf{v_{13}}. \quad (9)$$

The integral (6) is then given by:

$$I_i(\hat{\mathbf{r}}) = 2A_i\, e^{-j\frac{\alpha+\beta}{3}} \int_{u=0}^{u=1}\int_{v=0}^{v=1-u} e^{j(\alpha u+\beta v)}\,dv\,du, \quad (10)$$

whose solution is

$$I_i(\hat{\mathbf{r}}) = 2A_i\, e^{-j\frac{\alpha+\beta}{3}} \left[\frac{\alpha e^{j\beta} - \beta e^{j\alpha} + \beta - \alpha}{\alpha\beta(\alpha-\beta)}\right], \quad (11)$$

where

$$\alpha = k_1 \mathbf{v_{12}}(\hat{\mathbf{r}} - \hat{\mathbf{p}}_\mathbf{i}), \quad (12)$$

$$\beta = k_1 \mathbf{v_{13}}(\hat{\mathbf{r}} - \hat{\mathbf{p}}_\mathbf{i}). \quad (13)$$

The expression (11) has the following singular values:

$$\alpha = 0, \beta \neq 0 \Rightarrow I_i(\hat{\mathbf{r}}) = 2A_i\, e^{-j\frac{\beta}{3}} \frac{1 + j\beta - e^{j\beta}}{\beta^2}, \quad (14)$$

$$\alpha \neq 0, \beta = 0 \Rightarrow I_i(\hat{\mathbf{r}}) = 2A_i\, e^{-j\frac{\alpha}{3}} \frac{1 + j\alpha - e^{j\alpha}}{\alpha^2}, \quad (15)$$

$$\alpha = \beta \neq 0 \Rightarrow I_i(\hat{\mathbf{r}}) = 2A_i\, e^{j\frac{\alpha}{3}} \frac{1 - j\alpha - e^{-j\alpha}}{\alpha^2}, \quad (16)$$

$$\alpha = \beta = 0 \Rightarrow I_i(\hat{\mathbf{r}}) = A_i. \quad (17)$$

REFERENCES

[1] C. Uluisik, G. Cakir, M. Cakir, and L. Sevgi, "Radar cross section (RCS) modeling and simulation, part 1: a tutorial review of definitions, strategies, and canonical examples," *Antennas and Propagation Magazine, IEEE,* vol. 50, no. 1, pp. 115-126, Feb. 2008.

[2] J. A. M. Lorenzo, A. G. Pino, I. Vega, M. Arias, and O. Rubiños, "ICARA: induced-current analysis of reflector antennas," *Antennas and Propagation Magazine, IEEE,* vol. 47, no. 2, pp. 92-100, April 2005.

[3] J. G. Meana, J. A. M. Lorenzo, F. Las-Heras, and C. Rappaport, "A PO-MoM comparison for electrically large dielectric geometries," *Antennas and Propagation Society International Symposium,* 2009. APSURSI '09. IEEE, 1-5 June 2009.

[4] J. G. Meana, J. A. M. Lorenzo, F. Las-Heras, and C. Rappaport, "Wave scattering by dielectric and lossy materials using the Modified Equivalent Current Approximation (MECA)," *Transactions on Antennas and Propagation, IEEE,* vol. 58, no. 11, pp. 3757-3761, 2010.

[5] D. Daroui and J. Ekman, "Parallel Implementations of the PEEC Method," *ACES Journal,* vol. 25, no. 5, pp. 410-422, 2010.

[6] R. J. Burkholder, Ç. Tokgöz, C. J. Reddy, and W. O. Coburn, "Iterative Physical Optics for Radar Scattering Predictions," *ACES Journal,* vol. 24, no. 2, pp. 241-258, 2009.

[7] S. R. Rengarajan and E. S. Gillespie, "Asymptotic approximations in radome analysis," *Transactions on Antennas and Propagation, IEEE,* vol. 36, no. 3, pp. 405-414, 1988.

[8] R. E. Hodges and Y. Rahmat-Samii, "Evaluation of dielectric physical optics in electromagnetic scattering," in *Proceedings 1993 Antennas and Propagation Society International Symposium,* EE.UU., June 1993.

[9] F. Sáez de Adana, I. González, O. Gutiérrez, P. Lozano and M. F. Cátedra, "Method based on physical optics for the computation of the radar

cross section including diffraction and double effects of metallic and absorbing bodies modeled with parametric surfaces," *Transactions on Antennas and Propagation, IEEE,* vol. 52, no. 12, pp. 3295-3303, 2004.
[10] B. B. Fraguela, "Optimization of the use of the memory hierarchy," *Course Notes,* Department of Electronics and Systems, University of A Coruña, Spain, October 2009.
[11] G. Wu, J. Xu, Y. Dou, and M. Wang, "Computation rotating for data reuse," *Computer Systems Architecture Conference,* 2008. ACSAC 2008. 13th Asia-Pacific. Hsinchu, August 2008.
[12] D. H. Staelin, A. W. Morgenthaler, and J. A. Kong, *Electromagnetic Waves,* USA: Prentice Hall, 1994.
[13] C. A. Balanis, *Advanced Engineering Electromagnetics,* 1st ed. New York, USA: John Wiley and Sons, 1989.
[14] M. Arias, O. Rubiños, I. Cuiñas, and A. G. Pino, "Electromagnetic scattering of reflector antennas by fast physical optics algorithms," *Recent Res. Devel. Magnetics,* no. 1, pp. 43-63, 2000.
[15] G. Krawezik and F. Cappello, "Performance comparison of MPI and OpenMP on shared memory multiprocessors," *Concurrency Computat.: Pract. Exper.,* vol. 18, no. 1, pp. 29-61, Oct. 2005.

Hipólito Gómez-Sousa received the M.S. degree in telecommunications engineering from the University of Vigo, Vigo, Spain, in 2009.

Since 2009, he has been with the Department of Signal Theory and Communications, University of Vigo. His current research interests are on computational electromagnetism, THz sensing systems, and quantum cryptography.

José Ángel Martínez-Lorenzo (S'03–M'05) was born in Madrid, Spain, in 1979. He received the M.S. and Ph.D. degrees in telecommunications engineering from the University of Vigo, Vigo, Spain, in 2002 and 2005, respectively.

He was a Teaching and Research Assistant with the University of Vigo from 2002 to 2004. He joined the faculty at the University of Oviedo, Gijón, Spain, in 2004, where he was an Assistant Professor with the Department of Signal Theory and Communications until 2006. During the spring and summer of 2006, he was a Visiting Researcher with the Bernard Gordon Center for Subsurface Sensing and Imaging Systems (Gordon-CenSSIS), Northeastern University, Boston, MA. He was appointed as a Research Assistant Professor with the Department of Electrical and Computer Engineering, Northeastern University. He is currently a Ramon y Cajal researcher at the University of Vigo. He has authored over 80 technical journal and conference papers. His research is geared toward the understanding, modeling, and quantitative prediction of complex electromagnetic problems with special application to security sensing systems, communication systems, and biomedical systems.

Oscar Rubiños-López obtained the M.S. and Ph.D. degrees in telecommunication engineering from the Universidad de Vigo in 1991 and 1997, respectively.

He joined the Universidad de Vigo in 1991 and is currently an associate professor with the Dept. of Signal Theory & Communications at the Universidad de Vigo. From 2001 to 2006, he held the position of Vice-President of University Extension (2001-2002) and for University Extension and Students at the University of Vigo. His research interests include: the analysis and design of broadband antennas, numerical simulation of applied electromagnetic problems, terahertz technology for electromagnetic sensing applications, satellite systems and wireless communications

Javier Gutiérrez-Meana was born in Gijón, Spain, in 1982. He received his M.S. and Ph.D. degrees in electrical engineering from the University of Oviedo (Spain) in 2005 and 2010, respectively.

He joined the R and D department of CTIC Foundation in 2005, and since 2006, he is a Research Assistant with the Area of Theory of Signal and Communications (University of Oviedo). He was a Visiting Researcher at The Gordon CenSSIS – Northeastern University (Boston) in 2008. His interests and research studies are focus on the evaluation of electromagnetic coverage in rural/urban electrically large scenarios by means of high frequency techniques.

María Graña-Varela received the M.S. and Ph.D. degrees in telecommunication engineering from the University of Vigo, Spain, in 2000 and 2009, respectively.

From 2000 to 2005, she took part in several projects related to signal propagation and antennas design, initially with a research fellowship in the University of Vigo and in the Polytechnique University of Madrid and, from 2002, working in a Spanish telecommunication company as a network planning engineer. From 2005 to nowadays, she is with the Group of Antennas of the University of Vigo, involved in projects to design antennas for spatial communications. Her research interests include reconfigurable reflector antennas and computational electromagnetism.

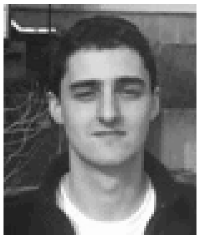

Borja González-Valdés was born in Gijón, Spain, in 1981. He received the B.S. and M.S. degree in 2006 in telecommunications engineering from the University of Vigo.

Since this moment to present, he has been research grant holder in the Department of Signal Theory and Communications, University of Vigo, Spain. During 2008 and 2009, he was a Visiting Researcher at the CenSSIS (The Bernard M. Gordon Center for Subsurface Sensing and Imaging Systems), Northeastern University, Boston.

He received his Ph.D. in electromagnetic engineering in 2010. His current research interest is geared toward the modeling and simulation of electromagnetic systems, with special application to high-performance reconfigurable reflectors.

Marcos Arias-Acuña was born in Vigo, Spain, on June 1, 1968. He received the Ingeniero de Telecomunicacion degree and Doctor Ingeniero de Telecomunicacion degree from the University of Vigo in 1991 and 1997, respectively.

He is a Profesor Titular since 1998 and has been with the Department of Signal Theory and Communications teaching radio communications since 1992. He has worked in projects related with antennas for satellite and radioastronomy and communication systems such DVB-T, LMDS, and UMTS. His research interests include:

- Reflector antennas, feeder for reflector antennas (arrays, horns...), shaped reflectors.
- Communication systems.
- High frequency techniques for modeling electromagnetic problems.

Analysis of Circular Slots Leaky-Wave Antenna in Cylindrical Waveguide by Wave Concept Iterative Procedure

Z. Houaneb[1], H. Zairi[1], A. Gharsallah[1], and H. Baudrand[2]

[1] Unité Circuit Système électronique HF. Faculté des sciences de Tunis. Tunisie
zied_houaneb@yahoo.fr, Hassen.zairi@ipsi.rnu.tn, ali.gharsallah@fst.rnu.tn

[2] Laboratoire LAPLACE, UPS-INP Toulouse. France
henri.baudrand@yahoo.fr

***Abstract*—** This paper presents the analysis of circular slots leaky-wave antenna by using an iterative method based on the wave concept. The classic method has been reformulated in cylindrical coordinates in order to be adequate for the analysis of the leaky-wave antenna with fast convergence. The proposed leaky-wave antenna can be used to replace a micro-strip patch array. Numerical results are presented to illustrate the advantages of the proposed structure. A good agreement between the new wave concept iterative procedure (WCIP) method results and published data is obtained.

***Index Terms*—** Circular patch, Hankel transform, leaky-waves, multi slits antenna, wave concept.

I. INTRODUCTION

For many years, there has been an increasing interest in microstrip leaky-wave antennas (LWAs) for their several features, which made them attractive candidates for many applications, ranging from mobile communications to phased array radar systems. They are replacing the conventional antennas in electronic scanning applications by frequency steering [1, 7].

Two-dimensional (2-D) microstrip planar antennas constitute a prime candidate for the exploration, separately, in two distinct perpendicular planes. The design of these antennas depends upon understanding the effects of patches excitation, substrate thickness, dielectric constant, and grids spacing on its scan performance. A few years ago, the use of 2-D scanning possibility both in elevation and azimuth planes was realized by additional phase-shifters in one plane and the frequency scanning in the other. This geometry was proposed in order to enhance the capabilities of 1-D uniform radiating structures by frequency changes [8, 10]. In recent years, there has been significant development in planar radiating structures for 2-D scanning features in millimetre-wave range applications, particularly in two dimensional periodic structures.

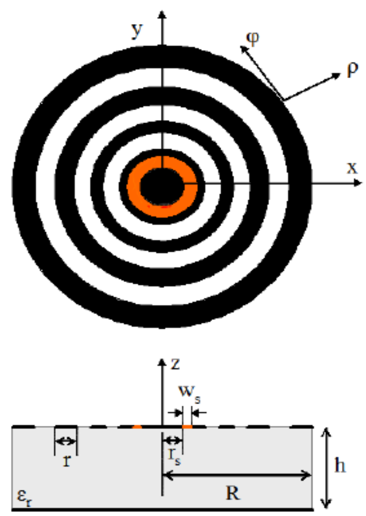

Fig. 1. Multi-slits antenna design.

The aim of this paper is to use the two-dimensional leaky-wave, which propagates outward radially along a planar surface. Among the printed antennas which can satisfy the above conditions is a series of concentric slits around a circular patch in cylindrical waveguide fed by a central ring, which maximizes the excitation of leaky-waves (See Fig. 1). Before exciting the fundamental TM_0 mode of the cylindrical waveguide, an electric source independent of φ is chosen and placed in the first slot. Thus, the various parts of the antenna are successively excited, in order to generalize leaky-wave phenomenon in all the directions of plane with circular wave forms.

To study this structure, a new wave concept iterative procedure (WCIP) in cylindrical coordinates is used. It consists in generating a recursive relationship between a given wave source and reflected waves at the interface containing the circuit [11]. The implementation of the iterative calculation is shown to extract the scattering parameters (S_{ij}) and generate the radiation patterns of the new structure. It consists of generating a recursive relationship between a given source wave and reflected waves at the interface containing the circular circuit. This discontinuity plane is divided into cylindrical cells and characterized by a scattering matrix operator depending on boundary conditions. Then, a Hankel transform is used to pass from spatial to spectral domain for each iteration of the recursive process. The advantage of the use of this method of simulation is to take into account the coupling between the circular slits without making additional calculations.

II. WCIP FORMULATION

Let us consider the shielded circular circuit, assumed to be lossless, presented in Fig. 2. The air-dielectric interface (plane Ω) is divided into cylindrical cells denoted by three subdomains corresponding to metal, dielectric and source domains. The wave concept is introduced by writing the transverse electric field $\vec{E}_i$ and surface tangential current density $\vec{J}_i$ in terms of incident ($\vec{B}_i$) and reflected ($\vec{A}_i$) waves. This leads to the following set of equations [12]:

$$\begin{cases} \vec{A}_i = \dfrac{1}{2\sqrt{Z_{0i}}}\left(\vec{E}_i + Z_{0i}\vec{J}_i\right) & i=1,2 \\ \vec{B}_i = \dfrac{1}{2\sqrt{Z_{0i}}}\left(\vec{E}_i - Z_{0i}\vec{J}_i\right) & i=1,2 \end{cases}, \quad (1)$$

where $Z_{0i} = \sqrt{\mu_0 / \varepsilon_0 \varepsilon_{ri}}$ is the characteristic impedance of region i (i = 1, 2) and ε_{ri} is the relative permittivity of the region i. $\vec{J}_i$ is the surface tangential current density as $\vec{J}_i = \vec{H}_i \times \vec{n}_i$, with $\vec{n}_i$ a unit vector normal to the interface Ω and $\lfloor \times \rfloor$ is the cross product operator.

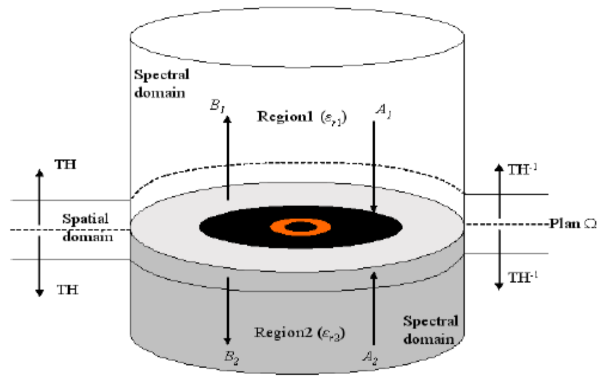

Fig. 2. The ideal WCIP structure.

$\vec{B}_i$ and $\vec{A}_i$ are incident and reflected waves in region i associated with the discontinuity interface Ω. The iterative process consists in establishing a recurrence relationship between waves $\vec{B}_i$ and $\vec{A}_i$. In order to generate incident waves $\vec{B}_i$ in the space domain, the circular circuit is excited by an electric planar source. Supposing that the space above the patch is equipped with cylindrical symmetry, it will be possible to consider the circular patch as a discontinuity between two half spaces that form two cylindrical guides of infinity radius.

The decomposition of the incident wave vector $B_i(\rho,\varphi)$ on the basis of mode TE and TM of the cylindrical guide, leads us to obtain:

$$B_i(\rho,\phi) = \sum_{m,n}\left(B^{\mathrm{TE}}_{i;mn}\left|f^{\mathrm{TE}}_{mn}(\rho,\phi)\right\rangle + B^{\mathrm{TM}}_{i;mn}\left|f^{\mathrm{TM}}_{mn}(\rho,\phi)\right\rangle\right), \quad (2)$$

where f^{α}_{mn} are mode functions of cylindrical guide with α={TE,TM}. By choosing an electric excitation source with a shape of ring with thickness w_s on the patch, the expressions of the cylindrical modes can be reduced due to fact that the electric and magnetic fields in the plane Ω are independent of φ. Thus, the radial component of electromagnetic TM mode is only excited.

By replacing f^{TM}_{mn} by their expressions of mode, we obtain the magnitude of TM mode:

$$B^{TM}_{i,mn} = -\frac{1}{\sqrt{\pi}} k_\rho \left\langle J'_n(k_\rho \rho) \middle| B_{i,\rho}(m,n) \right\rangle, \quad (3)$$

where k_ρ is the radial wave number and J'_n is the derivative of the Bessel function.

The scalar product in (3) becomes then:

$$\left\langle J_n^{'}\left(k_\rho \rho\right) \middle| B_{i,\rho}\left(m,n\right)\right\rangle = \int_0^R B_{i,\rho}\left(m,n\right) J_n^{'}\left(k_\rho \rho\right) \rho d\rho. \quad (4)$$

By using the recurrent relation of Bessel functions of integer order, the integral in equation (4) can be written as a Hankel transform [13, 14]. This transform enables us to move from space domain to the spectral domain.

As far as separable geometry is concerned, the set of functions associated with both TE and TM transverse electric field provides a complete set of orthogonal basis functions suitable to expand electric fields in the boxed structure as [15]:

$$E_T(\rho,\phi) = \sum_{\alpha,m,n} e_{mn}^{\alpha} f_{mn}^{\alpha}(\rho,\phi). \quad (5)$$

The tangential current density is expressed as:

$$J_T(\rho,\phi) = \sum_{\alpha,m,n} e_{mn}^{\alpha} Y_{mn}^{\alpha} f_{mn}^{\alpha}(\rho,\phi). \quad (6)$$

The expressions (5) and (6) support the expansions in the spectral domain of the integral operator $\hat{Y}$ defined as:

$$\vec{J} = \hat{Y}\vec{E}$$

$$\hat{Y} = \sum_{\alpha,m,n} \left| f_{mn}^{\alpha} \right\rangle Y_{mn}^{\alpha} \left\langle f_{mn}^{\alpha} \right|. \quad (7)$$

Hence, from definition (1), the waves can be expanded on the same set of basis functions of the tangential fields and the $\hat{\Gamma}_i$ operator such that:

$$\vec{A}_i^{\alpha} = \hat{\Gamma}_i^{\alpha} \vec{B}_i^{\alpha}, \quad (8)$$

where i = 1,2 refers to the sides of interface Ω. Thus, $\hat{\Gamma}_i^{\alpha}$ has the general form:

$$\hat{\Gamma}_i^{\alpha} = \sum_{m,n} \left| f_{mn} \right\rangle \Gamma_{mn}^{\alpha} \left\langle f_{mn} \right|. \quad (9)$$

Applying $\hat{\Gamma}$ simply consists in multiplying the modal amplitude of the waves by the corresponding numbers $\hat{\Gamma}_i^{TE}$ and $\hat{\Gamma}_i^{TM}$ in (11), such that:

$$\hat{\Gamma}_i = \frac{1 - Z_{0i} Y_{i,mn}^{\alpha}}{1 + Z_{0i} Y_{i,mn}^{\alpha}}, \quad (10)$$

where $Y_{i,mn}^{\alpha}$ is defined in Table 1, $k_r^2 = \omega^2 \varepsilon_0 \varepsilon_r \mu_0$, $\gamma^2 = k_\rho^2 - k_r^2$ and $Y_r = \sqrt{\varepsilon_0 \varepsilon_{ri} / \mu_0}$ is the admittance of each domain.

Table 1: Mode admittance expressions of a uniform waveguide

	TE mode	TM mode
Infinite guide	$-jY_r\gamma / k_r$	$-jY_r k_r / \gamma$
Guide short circuited at distance h	$-jY_r\gamma \coth(\gamma h)/k_r$	$-jY_r k_r \coth(\gamma h)/\gamma$

The spectral wave $\vec{B}_i^{\mathrm{TM}}$ is reflected in each domain by the $\hat{\Gamma}$ operator to give the reflected wave $\vec{A}_i^{\mathrm{TM}}$:

$$\vec{A}_i^{\mathrm{TM}} = \hat{\Gamma}_i \vec{B}_i^{\mathrm{TM}}. \quad (11)$$

To return to the spatial domain, an inverse Hankel transform must be used:

$$\vec{A}_{i,\rho} = \mathbf{HT}^{-1}\left\{\vec{A}_i^{\mathbf{TM}}\right\}. \quad (12)$$

The wave $\vec{A}_{i,\rho}$ is scattered in interface plane Ω by Γ_Ω factor [16, 17] in order to constitute the incident wave $\vec{B}_i$ for the next iteration:

$$\vec{B}_i = \left[\Gamma_\Omega\right]\vec{A}_i + \vec{B}_0, \quad (13)$$

where $\vec{B}_0$ is source excitation.

The implementation of the iterative procedure consists in establishing a recurrent relationship between each side of the interface (discontinuity). By using the boundary conditions in spatial domain (13) and reflection in the spectral domain (11) the following relationships can be obtained:

$$\vec{B}_i^{(k)} = \Gamma_\Omega \vec{A}_i^{(k-1)} + \vec{B}_i^{(0)} \quad (14)$$

$$\vec{A}_i^{(k)} = \hat{\Gamma}_i \vec{B}_i^{(k)}, \quad (15)$$

where i is the index media, k is the number of iterations. The iterative process is stopped when the electric field and the current density converge. So, the main characteristics of the circuit can be extracted. Once convergence is achieved, the $\vec{B}_i$ and $\vec{A}_i$ waves are expressed in spatial domain and the electric field and current density can be determined at the interface plane Ω. It is done using the equations in (1).

$$\vec{E}_i = \sqrt{Z_{0i}}\left(\vec{A}_i + \vec{B}_i\right) \tag{16}$$

$$\vec{J}_i = \frac{1}{\sqrt{Z_{0i}}}\left(\vec{A}_i - \vec{B}_i\right). \tag{17}$$

The algorithm of the iterative process is shown by Fig. 3. In order to implement this process, the FORTRAN language is used.

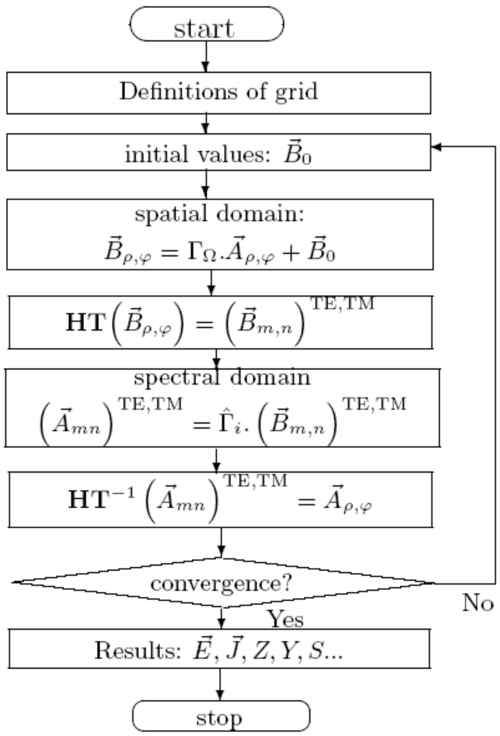

Fig. 3. The WCIP algorithm.

III. VALIDATION OF WCIP METHOD

The presented formulation was implemented in FORTRAN code. To demonstrate the effectiveness of the method, circular patch antenna has been considered (See Fig. 4).

Figure 5 shows the S_{11} and real and imaginary parts of Z_{in} convergence at 6.6 GHz for the structure given by Fig. 4 for a radius patch equal to 7.0 *mm*. Figure 6 shows the simulated resonant frequency obtained for the space wave against radius R compared to the published data [18]. Thus, a good agreement between simulated and published data is observed.

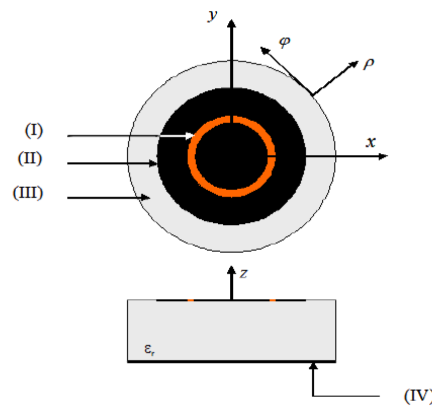

Fig. 4. Configuration of the circular patch: (I) excitation ring, (II) circular patch, (III) dielectric, (IV) ground plane.

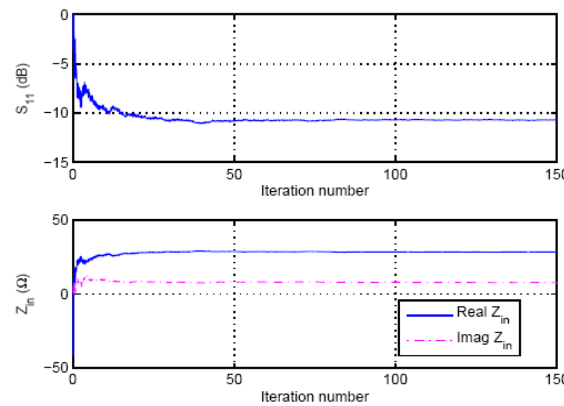

Fig. 5. S_{11} and Z_{in} convergence versus iterations number at 6.6GHz.

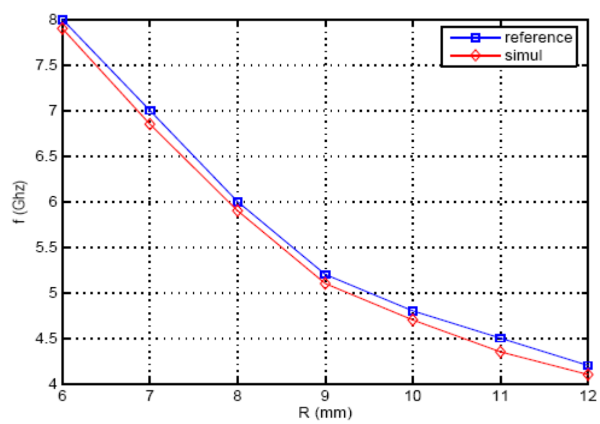

Fig. 6. The variation of resonance frequency f simulated for space wave against R compared to those published.

To validate the WCIP in cylindrical coordinate, the Q-factor of surface wave has been simulated versus the height of substrate (Fig. 7) and the radius of the patch (Fig. 8) for two different values of ε_r and compared to published data [18]. The accuracy of these figures explains that the addition of the tangential electric field and density of current given by magnetic and electric walls is necessary. We denote by E_{ma} and E_{el} the fields given by magnetic and electric walls situated at large value of r approximately equal to $5\lambda g$. The total field is given by:

$$\begin{aligned} E_{tot} &= E_{ma} - jE_{el} \\ &= \cos(k_0 r) - j\sin(k_0 r) \\ &= \exp(jk_0 r). \end{aligned} \tag{18}$$

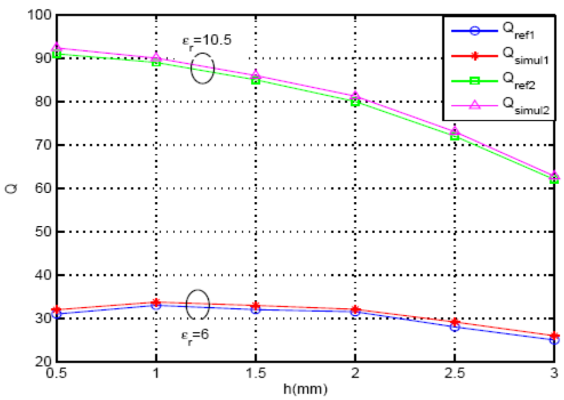

Fig. 7. The variation of Q-factor of surface wave with h for two different ε_r and $R = 7mm$.

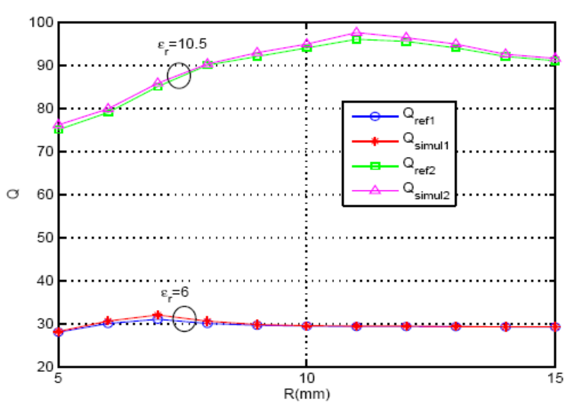

Fig. 8. The variation of Q-factor of surface wave with R for two different ε_r and $h = 1.27mm$.

IV. ANTENNA DESIGN

The structure proposed in this work is an antenna of low profile. Fig. 1 illustrates the circular microstrip patch antenna, which incorporates annular slits. This new design is fed by a circular ring. The circular patch of radius R is mounted on a substrate of thickness h and with a dielectric constant ε_r. The feed ring of width w_s, is located at a distance r_s from the centre of the patch. The annular slits are situated concentrically around the central circular patch. The distance r between the slits is chosen when the derivative Bessel function $J_0^{'}$ is in its maximum. The interface Ω is sampling in 340*40 polar pixels (radial direction by 340 and azimuth direction by 40).

When this antenna is excited by an electric source, that is independent of the variable φ, the radial component of TM_0 mode is only excited. In each slit exists an electric field which is created by the leaky-wave. These fields give rise to a radiated field. This one is identical to an array antenna patch when it is excited by a feeder network. Thus, each patch creates a far field in space. The advantage of our antenna is the use of only one source instead of a network. Also, the condition of spacing between the slits is not necessarily $\lambda_g/2$. Thus, the shape of the proposed antenna is more compact.

First, we study an antenna with a central ring (that represents the source) and an annular slit to validate the WCIP method of simulation. This antenna is mounted on a substrate of thickness h = 2.0 *mm* and with a permittivity ε_r = 4.25. This one is fed by the central ring having an interior radius r_0 = 0.5 *cm* and a width w_s = 1.0 *mm*. The annular slit has a width w = 1.0 *mm* and an interior radius 1.0 *cm*. The distance between the central ring and the slit that surrounds it is r = 2.0 *mm*. The r distance is chosen in a way that the derivative Bessel function $J_0^{'}$ reaches its first maximum. Both the boundary of the domain that is a perfectly cylindrical conductor and the radius of patch have 6.0 *cm* of radius.

In order to demonstrate the validity and the advantages of the iterative approach, a program implanted with a symbolic calculation with FORTRAN language is developed. Figure 9 represents the distribution of the electric field on the plane Ω at the resonance frequency. We notice the appearance of the electric field in the slit, which is due to the leaky-wave.

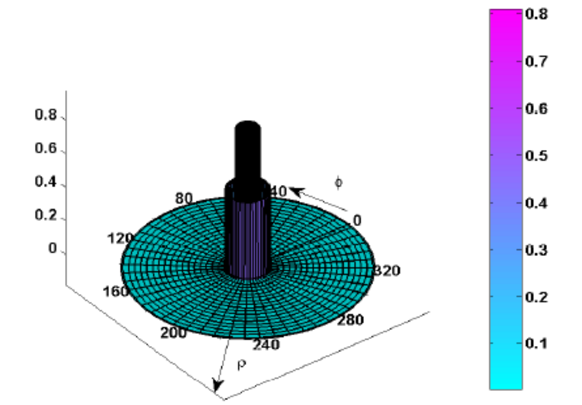

Fig. 9. The electric field magnitude as a function of ρ-φ.

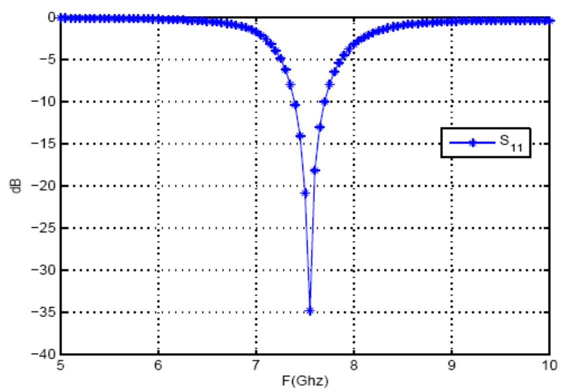

Fig. 10. Return loss as function of frequency.

The return loss parameter is extracted in Fig. 10. The resonance frequency of this antenna is located at 7.55 GHz. For each frequency, the WCIP process consumes 13 seconds but the ADS software consumes 19 seconds and the HFSS software 20 seconds. All theses tests are done with the same computer characteristics. Moreover the time of calculation is less than the one using a conventional technique.

In Fig. 11, the real and imaginary parts of input impedance of this antenna with two slits are represented. The real part of impedance is 50 ohm and the imaginary part is around 0 at the resonance frequency, this shows that our antenna is resonating.

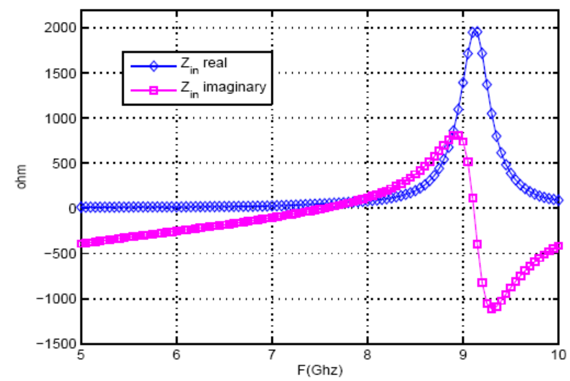

Fig. 11. Real and imaginary parts of input impedance of antenna with two slits.

V. RADIATION PATTERNS

To calculate the radiated field by multi-slits antenna, each slit can be represented as a magnetic loop of current [19]. Each loop creates a far field E_{rad}^{k} where k designs the index of slits. The total field radiated by our antenna (E_{rad}^{t}) is the sum of the fields radiated by each loop of current:

$$E_{rad}^{t} = \sum_{k=1}^{N_s} E_{rad}^{k} \,, \tag{19}$$

where N_s is the number of slits. The centre of the slits defines the origin of the reference mark. As the antenna has symmetry of revolution, the magnetic current is expressed with Fourier series:

$$\vec{M}^{k}(\rho,\varphi) = \sum_{n_\varphi=-\infty}^{+\infty} \left(M_{\rho}^{k}(\rho; n_\varphi)\vec{\rho} + M_{\varphi}^{k}(\rho; n_\varphi)\vec{\varphi} \right) e^{jn_\varphi \varphi} \,. \tag{20}$$

It is the same for the far electric field, given by:

$$E_{\theta}^{k}(\theta,\varphi) = -k\Psi(r_k) \sum_{n=-\infty}^{+\infty} j^{n} e^{jn\varphi} \left[jC_{\theta,\rho}^{k}(\theta;n) + C_{\theta,\varphi}^{k}(\theta;n) \right] \tag{21}$$

$$E_{\varphi}^{k}(\theta,\varphi) = k\Psi(r_k)\cos(\theta) \sum_{n=-\infty}^{+\infty} j^{n} e^{jn\varphi} \left[C_{\varphi,\rho}^{k}(\theta;n) - jC_{\varphi,\varphi}^{k}(\theta;n) \right] \tag{22}$$

with

$$\Psi(r_k) = \frac{e^{-jkr_{ki}}}{r_k}$$

$$C_{\theta,\rho}^{k}(\theta;n) = \int_{r_k - \frac{w_k}{2}}^{r_k + \frac{w_k}{2}} M_{\varphi}^{k}(\rho;n) \frac{nJ_n(k\rho\sin\theta)}{k\rho\sin\theta} \rho d\rho$$

$$C_{\theta,\varphi}^{k}(\theta;n) = \int_{r_k - \frac{w_k}{2}}^{r_k + \frac{w_k}{2}} M_{\rho}^{k}(\rho;n) J_{n}^{'}(k\rho\sin\theta) \rho d\rho$$

$$C_{\varphi,\rho}^{k}(\theta;n)=\int_{r_k-\frac{w_k}{2}}^{r_k+\frac{w_k}{2}} M_{\varphi}^{k}(\rho;n)J_n^{'}(k\rho\sin\theta)\rho d\rho \quad (23)$$

$$C_{\theta,\varphi}^{k}(\theta;n)=\int_{r_k-\frac{w_k}{2}}^{r_k+\frac{w_{ki}}{2}} M_{\rho}^{k}(\rho;n)\frac{nJ_n(k\rho\sin\theta)}{k\rho\sin\theta}\rho d\rho \quad .$$

The simulated radiation patterns at the resonance frequency are given by Fig. 12.

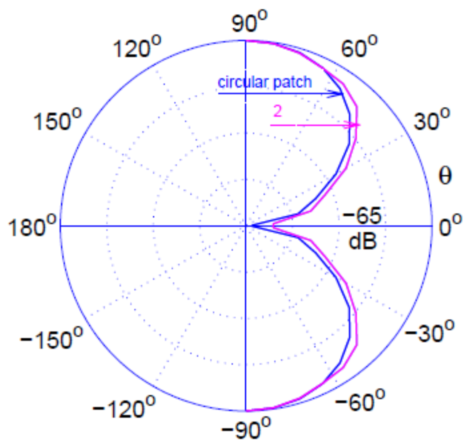

Fig. 12. The radiation patterns at frequency 7.55 GHz. (The numbers in the figure represent the number of slits on the patch.)

The directivity of the proposed antenna is improved by addition of one slit in the circular disc. The beam width to -3dB is reduced by 5 degrees if we add one slit in this circular patch. That is, due to the surface waves which were excited by the source that an electric field in the second slit taking part in the radiation can be seen. This is equivalent to an antenna array with two patches. To improve the directivity in a considerable way, it is necessary to increase the number of slits. These slits are outdistanced by *r* distance between them such as the derivative Bessel function $J_0^{'}$ which reaches its maximums on each slit. The radiated field at $\phi = 0$ is usually equal to zero for any number of slits. This is due to the symmetry of this antenna. The study of coupling between the slits is not necessary since the new WCIP method as electromagnetic simulator is used. The advantage of this method is to take into account the coupling between the cells, which constitutes the interface plane Ω where the circular antenna with slits is put.

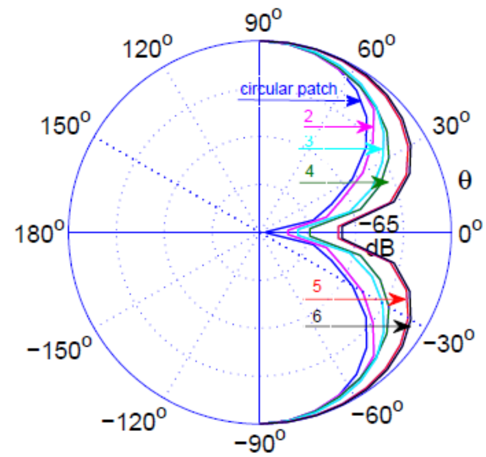

Fig. 13. The radiation patterns at frequency 7.55GHz of different number of slits. (The numbers in the figure represent the number of slits on the patch.)

According to Fig. 13, the 3dB radiation ranges from 90 degree of circular patch to between 30 and 60 degree for a structure with slits. Thus, the band increases with the number of slits. In Table 2, the reduction of the beam width to -3dB of the antenna with slits compared with circular patch is shown.

Table 2: Beam width reduction

Number of slits	Beam width reduction (degree)
2 slits	5°
3 slits	23°
4 slits	31°
5 slits	36°
6 slits	38°

We notice that if we have more than six slits, the reduction of the beam width will not be significant any more. So, we can limit ourselves to an antenna with six slits.

VI. CONCLUSION

In this paper, the formulation and the implementation of a new iterative method based on the concept of waves is presented to study a new leaky-wave antenna with circular shape containing a number of concentric slits around a circular patch, which can be used for broadcast applications. It is demonstrated that this antenna can play the part of an array antenna if we increase the number of slits in the structure. The advantage of this new antenna is its compact form and facility of realization. Numerical results have been obtained with reduced CPU time because of the Hankel transformation used in the iterative method. A good agreement between our results and published data is obtained.

REFERENCES

[1] C. Lin and C. Tzuang, "A dual beam micro CPW leaky-mode antenna," *IEEE Trans. Antenna And propag.,* vol. 48, pp. 310-316, 2000.

[2] C. Caloz, S. Lim, and T. Itoh, "A novel leaky-wave retrodirective reflector using short/matched terminations," *33rd European Microwave Conference,* pp. 1071-1074, October 2003.

[3] T. Zhao, D. Jackson, J. Williams, D. Yang, and A. Oliner, "2-D periodic leaky-wave antennas- Part I: Metal patch design," *IEEE Trans. Anten. and Propag.,* vol. 53, pp. 3505-3514. 2005.

[4] T. Zhao, D. Jackson, and J. Williams, "2-D periodic leaky-wave antennas- Part II: Slot design," *IEEE Trans. Anten. and Propag.,* vol. 53, pp. 3515-3524. 2005.

[5] T. Zhao, D. Jackson, J. Williams, and A. Oliner, "General formulas for 2-D leaky-wave antenna," *IEEE Trans. Anten. and Propag.,* vol. 53, pp. 3525-3532, 2005.

[6] D. Killips, J. Radclife, L. Kempel, and S. Schneider, "Radiation by a linear array of half-width leaky-wave antennas," *ACES Journal*, vol. 21, no. 3, pp. 248-255, 2006.

[7] J. R. James and G. Andrasic, "Analysis and computation of leaky-wave hyperthermia applicator," *ACES Journal*, vol. 7, no. 2, pp. 72-84, 1992.

[8] P. Liao and R. York, "A new phase-shifters beam scanning technique using arrays of couple oscillator," *IEEE Trans. Microwave Theor. Techn.,* vol. 41, pp. 1810-1815, 1993.

[9] K. Chen, Y. Qian, C. Tzuang, and T. Itoh, "A periodic microstrip radial antenna array with a conical beam," *IEEE Trans. Anten. Propag.,* vol. 51, no. 4, pp. 756-765, 2003.

[10] C. Hu, C. Jou, and J. Wu, "An aperture coupled linear microstrip leaky-wave antenna array with two dimensional dual beam scanning capability," *IEEE Trans. Anten. Propag.,* vol. 48, pp. 909-913, 2000.

[11] R. S. N'gongo and H. Baudrand, "A new approach for microstrip active antennas using modal FFT algorithm," *IEEE AP-S Int symp Ind USNC/URSI Natl Radio Sci Mtg,* Orlando, FL, July 1999.

[12] H. Zairi, A. Gharsallah, A. Gharbi, and H. Baudrand, "Modelling of coupled microstrip antennas integrated with EBG structure using an iterative method," *ACES Journal,* vol. 23, no. 4, pp. 357-362, Dec. 2008.

[13] M. Guizar-Sicairos and J. C. Gutierrez-Vega, "Computation of quasi-discrete Hankel transforms of integer order for propagating optical wave fields," *J. Opt. Soc. Am.,* vol. 21, no. 1, pp. 53-58, 2004.

[14] Z. A. Delecki, "Eigenvalue computation for application of the finite Hankel transform in coaxial regions," *ACES Journal,* vol. 4, no. 1, pp. 41-56, Mar. 1989.

[15] H. Baudrand, "The wave concept in electromagnetic problem: application in integral methods," *Asia Pacific Microwave Conference*, New Delhi, December 1996.

[16] A. Gharsallah, A. Gharbi, and H. Baudrand, "Analysis of interdigital capacitor and quasi-lumped miniaturized filters using iterative method," Int *J Num Modelling: Electronic Networks, devices and Fields,* vol. 15, issue 2, pp. 169-179, Apr. 2002.

[17] A. Gharsallah, R. Garcia, A. Gharbi, and H. Baudrand, "Wave concept iterative process merges with modal fast Fourier transformation to analyze microstrip filters," *ACES Journal*, vol. 16, no. 1, pp. 61-67, Mar. 2001.

[18] D. El-Kouhen, H. Aubert, M. Ghomi, and H. Baudrand, "Q-factor computation of radiation loss corresponding to surface wave in a patch circular resonator," *Electronics Letters*, vol. 32, no. 22, pp. 2039-2041, October 1996.

[19] S. J. Orfanidis, "Electromagnetic Waves and Antennas," Copyright (c) 1996-2008 by Sophocles J. Orfanidis, www.ece.rutgers.edu/ orfanidi/ewa.

Zied Houaneb was born in Tunisia. He received his master's degree in telecommunication from Ecole Supérieure des Communications de Tunis, Tunisia in 2002. He is currently working toward his Ph.D. degree at the Faculty of Sciences, Tunis, Tunisia. His research interests include circular devices and antennas for wireless communication and microwave integrated circuits.

Hassen Zairi received his master's degree in physics from the Faculty of Sciences, Tunis, Tunisia, in 2002 and the Ph.D. degree in 2005. He is currently an Assistant Professor with the Department of Electrical Engineering, Ecole Supérieure de Technologie et d'informatique, Tunis, Tunisia. His main research interests are in numerical methods for the analysis of microwave and millimeter-wave circuits.

Ali. Gharsallah received the degrees in radio-electrical engineering from the Ecole Supérieure de Télécommunication de Tunis in 1986 and the Ph.D. degree in 1994 from the Ecole Nationale d'Ingénieurs de Tunis. Since 1991, he was with the Department of Physics at the Faculty of Sciences, Tunis. His current research interests include antennas, multilayered structures, and microwave integrated circuits.

Henry Baudrand, Professor Emeritus at the Ecole Supérieure d'Electronique Electrotechnique Informatique, ENSEEIHT, of National Polytechnic Institute of Toulouse, France is specialized in Modelling of Passive and Active Circuits and Antennas. He is the author and co-author of three books:

- Introduction au calcul des éléments de circuits micoondes
- Optimisation des circuits non linéaires. (in collaboration with M.C.E. Yagoub)
- Calcul des circuits microondes par les schémas équivalents. (in collaboration with H.Aubert)

These books are published by CEPADUES Editions Toulouse.

He co-signed over 130 publications in international journals, four chapters in scientific books and 250 communications in international conferences.

He is a Fellow Member of IEEE Society, a Fellow Member of the Electromagnetism Academy and a Senior Member of the IEE society. He was President of URSI France commission B for 6 years (1993-1999), President of IEEE-MTT-ED French chapter (1996-1998), and President of International Comity of O.H.D. (Hertzian Optics and Dielectrics) between 2000 and 2004. He is awarded "Officier des Palmes académiques" and Doctor Honoris causa of lasi University (1996).

Parasitic Patch of the Same Dimensions Enabled Excellent Performance of Microstrip Antenna Array

Mingchun Tang, Shaoqiu Xiao, Tianwei Deng, Duo Wang, and Bingzhong Wang

The Institute of Applied Physics
University of Electronic Science and Technology of China, Chengdu, China, 610054
xiaoshaoqiu@uestc.edu.cn

Abstract - This paper presents a thorough investigation on the use of parasitic patch as an effective secondary radiator to suppress mutual coupling and improve the gain of a microstrip array. The measured results show that the proposed parasitic patch placed halfway between elements in the *E*-plane of two-element array not only suppresses mutual coupling by 7.3dB, but, also, improves the gain by 1.6dB. By further simulation and comparison, the results indicate the proposed parasitic patch is quite suitable for application into the high-density microstrip arrays.

Index Terms - Gain improvement, microstrip array, mutual coupling reduction, parasitic patch.

I. INTRODUCTION

Microstrip arrays are used extensively due to their many attractive features, including low profile, light weight, and convenience for integrating with microwave monolithic integrated circuit (MMIC) technologies. Despite the above important advantages over other conventional antennas, there are some drawbacks which have prevented practical applications. One of the most severe problems is that, when the substrate with high dielectric constant is selected, the strong mutual coupling is accordingly incurred in virtue of the pronounced surface wave excitation [1-3]. To suppress unwanted surface wave, lots of methods are presented, such as loading electromagnetic band-gap (EBG) structures [4], mu-negative (MNG) metamaterials [5, 6], and defected ground structures (DGSs) [7]. However, they take on some inherent defects in applications. EBG needs complicated and high-cost design, and takes too much spacing; MNG metamaterials are of narrowband and little mechanical robustness; DGSs lead to inevitable strong backward radiation through the notched ground.

In this paper, the parasitic antenna of the same dimensions is proposed, and it is etched halfway between the two *E*-coupled microstrip antennas as a simple and effective way to suppress surface wave and improve the whole gain, due to its “secondary radiation” property.

II. USING PARASITIC PATCH TO SUPPRESS MUTUAL COUPLING AND IMPROVE GAIN OF THE WHOLE ARRAY

The comprehensive studies related to the mutual coupling between adjacent microstrip antennas exist [8]. In a standard array configuration with a high permittivity substrate, the surface waves dominate and the coupling between elements in the *E*-plane orientation is greater than that in the *H*-plane [7]. Therefore, mutual coupling suppression between the *E*-plane-coupled elements is only investigated to validate the performance of the proposed parasitic antenna in Fig. 1. The parasitic antenna has the same dimensions of the two active antennas, and it is loaded halfway in the traditional probe-fed microstrip array, with the interelement spacing approximately three quarters of wavelength in free space.

The antenna arrays presented in this paper are all simulated using Ansoft HFSS [9], an electromagnetic simulator based on finite element method (FEM). Together with simulated results, the experimentally measured results of the array in Fig. 1 are entirely shown in Figs. 2 and 3. Because of strong surface waves, the mutual coupling (S_{21}) of -13.9dB in traditional array at the center resonant frequency 6.06GHz is observed in Fig. 2(a), which is in good agreement with the aforementioned analysis in Section I. When the parasitic patch of the same dimensions is etched halfway between the two elements as a secondary radiator in the *E*-plane, the mutual coupling drops to -21.2dB (7.3dB reduction) at the center

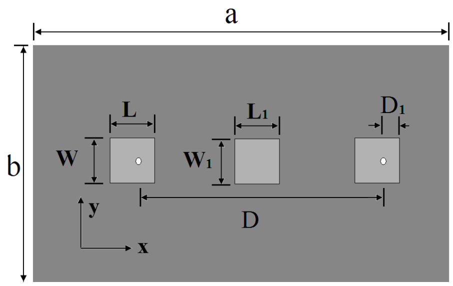

(a)

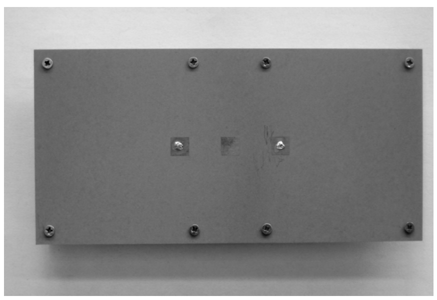

(b)

Fig. 1. Geometry of a two-element array with parasitic patch; the patches: $L= L_1=6.6mm$, $W=W_1=6.7mm$, the distance of the two active patches: $D=36mm$, the two probe-fed positions: D_1=4.2mm, the substrate ($a\times b=140mm\times 70mm$) with the dielectric constant ε_r=10.2 has the height = $2mm$. (a) dimensions in details, (b) fabricated antenna array.

resonant frequency 6.09 GHz in Fig. 2 (b). It is noticed that, due to the additional intercoupling between the active elements and parasitic element, there is a slight drift of the center resonant frequency occurrence (0.03GHz shifting).

The far-field radiation performance is also experimentally measured and compared as shown in Fig. 3. The side lobe drops distinctly and the gain pattern becomes smooth with no apparent ripples in comparison with that of the reference array [7], especially in the *E*-plane. As a secondary radiator, a certain surface wave constrained within substrate is radiated into front free space, which improves the whole array peak gain of radiation pattern in the front from 7.9dBi to 9.5dBi.

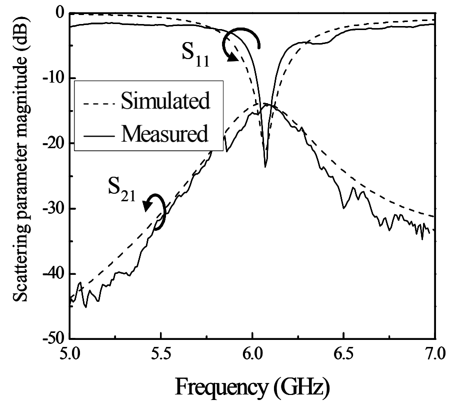

(a)

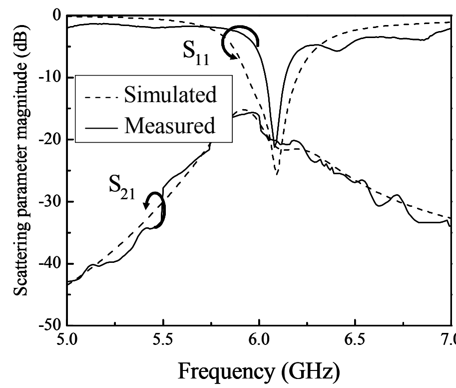

(b)

Fig. 2. Simulated and measured scattering parameters of the traditional array and parasitic patch loaded array. (a) traditional array, (b) parasitic patch loaded array.

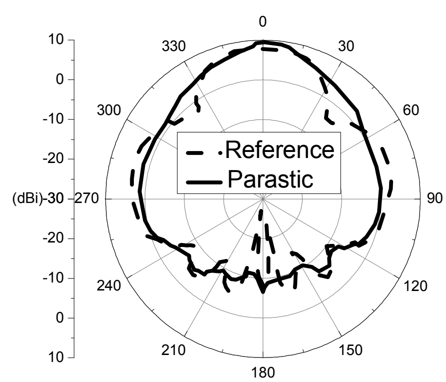

(a)

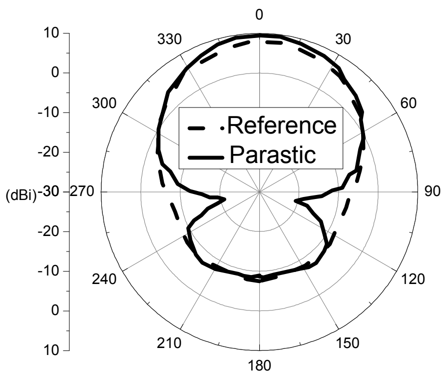

(b)

Fig. 3. Experimentally measured gain patterns of the traditional array and parasitic patch loaded array. (a) *E*-plane, (b) *H*-plane.

III. RESULTS AND ANALYSIS

To analyze the electromagnetic characteristics of parasitic patch, the surface current distribution on the upper surface of the three identical patches at the center resonant frequency 6.09GHz is, also, simulated, and the sketch is drawn in Fig. 4. It is shown that when the two *E*-coupled antennas are excited with the same phases and magnitudes, the current on parasitic patch is synchronously induced, which is regularly polarized on the surface in accordance with that on the active patches. Certain EM energy could radiate through the parasitic patch and much more energy is guided upwards into free space by comparing traditional array and the array with parasitic patch as shown in Fig. 5. It is in good agreement with the measured results in Fig. 3, which improves the main lobe gain. In details, the near-field illumination created by the proposed parasitic-patch-loaded array is more uniform than the traditional two-element array, and it has cosine-shaped illumination amplitude shown in

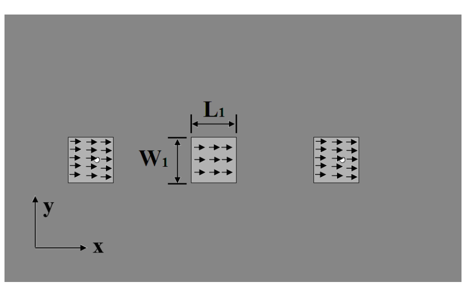

Fig. 4. Surface current distribution on all patches at resonance frequency.

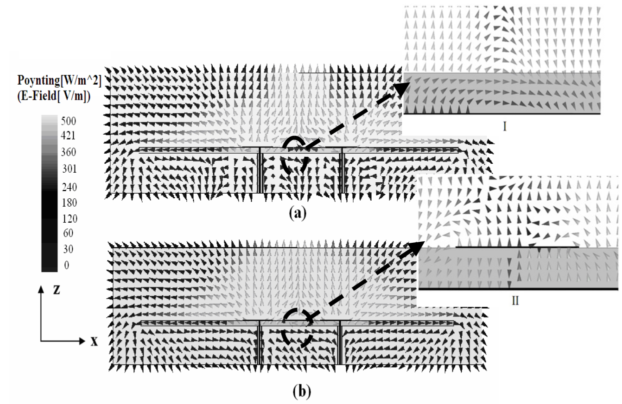

Fig. 5. Simulated Poynting vector distribution in *E*-plane of the two-element array and corresponding amplified *E*-field distribution images (I and II) in the middle places. (a) traditional array, (b) the array with parasitic patch.

Fig. 5(b), in opposition to the illumination in Fig. 5(a), which clearly shows some peaks in the Poynting vector amplitude. Therefore, the radiation diagram of the proposed parasitic-patch-loaded array has higher directivity (due to the fact that more uniform illumination creates a larger effective radiating aperture) and lower sidelobe level (as the cosine tapered amplitude illumination reduces diffraction at the edges of the patch), as it can be seen in the E-plane gain patterns shown in Fig. 3(a).

Furthermore, the current on the parasitic patch (in Fig. 4) is induced by surface wave in the substrate. It could be verified by comparing two amplified images in Fig. 5. The *E*-field of surface wave in the amplified image I is weak and homogeneous in the substrate. On the contrary, when the parasitic patch is loaded halfway, the *E*-field in the amplified image II is much stronger in the substrate. Besides, the *E*-field on the two sides of the parasitic patch is polarized in opposite phase, which demonstrates that the surface wave gives rise to parasitic patch resonance as two other active patches (Fig. 4). Accordingly, the parasitic patch acts as an energy director, and it guides the majority of the surface wave energy from the substrate into the front space so that the surface wave in the substrate degrades sharply. The reduction of surface wave interaction between the two active elements consequently incurs mutual coupling suppression (Fig. 2). Moreover, we add another probe-fed under the parasitic patch to excite it with the same phase. The simulation result demonstrates that the peak gain reaches 8.67dBi (which is lower than the array with parasitic patch in Fig. 1), and the mutual coupling between two elements at the edges is -15.7dB (slight mutual coupling reduction 1.8dB). It is seen that the active patch exhibits much poorer performance in comparison with the parasitic one.

It can be seen that the parasitic patch has two functions: mutual coupling suppression and gain improvement. In contrast of the aforementioned inherent defects (methods of EBG, mu-negative metamaterials, and DGS loading), this method, conquering the above problems, exhibits particular properties when the elements in array are placed in high density.

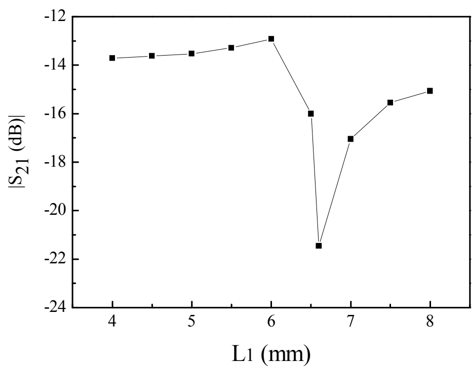

Fig. 6. The mutual coupling coefficient (S_{21}) against the length of parasitic patch L_1.

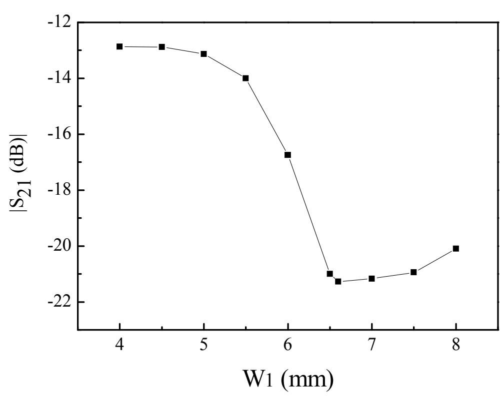

Fig. 7. The mutual coupling coefficient (S_{21}) against the width of parasitic patch W_1.

The dimensions of the parasitic patch are thoroughly simulated and compared in Figs. 6 and 7. Figure 6 gives the relationship between the mutual coupling S_{21} and the length of the parasitic patch when the width is fixed to *6.7mm*. The results indicate when its length changes, the mutual coupling changes accordingly. Especially when $L_1=L=6.6mm$ is chosen, the best mutual coupling suppression (S_{21}= -21.3dB) is attained. Similarly, the mutual coupling, also, alters with variation of the parasitic patch width, and $W_1=W=6.7mm$ is the most suitable value for mutual coupling reduction, on the premise of the fixed length *6.6mm*, shown in Fig. 7. It can be seen that the parasitic patch can be utilized as a radiating patch operating at 6.09GHz. However, the best choice is the use of ordinary parasitic patch of the same dimensions as the radiating elements.

Moreover, the performance of the parasitic patch in mutual coupling suppression is further analyzed in Fig. 8. In order to validate its predominant capability, the results of traditional array are also listed in Fig. 8. When the elements are high-density placed in the *E*-plane with the variation of interelement distance between $0.5\lambda_0$ and λ_0 (where λ_0 is the wavelength in free space at the operation frequency), the mutual coupling

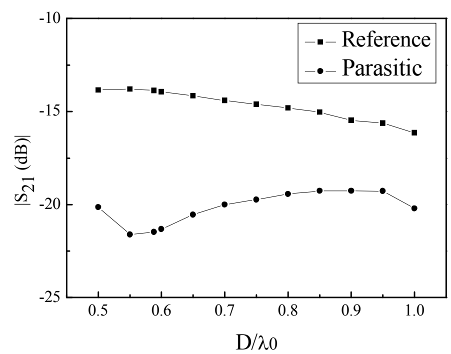

Fig. 8. The mutual coupling coefficient (S_{21}) against distance between two active elements in *E*-plane.

drops markedly (5-10dB), compared with the reference array. Thus, it is quite suitable to be utilized in a high density microstrip array application.

IV. CONCLUSIONS

A simple and effective method to suppress mutual coupling is presented in this paper. The arrays with and without parasitic patch are measured and compared, respectively. The results demonstrate that the compact parasitic patch can suppress mutual coupling by 7.3dB, and improve the gain of the array by 1.6dB in a two-element array. With the assistance of simulation analysis, the proposed parasitic patch with the same dimensions as the active elements is quite available to apply into high density microstrip array to suppress mutual coupling and improve the whole array radiation performance. In addition, due to low mutual coupling performance and simple configuration of the proposed parasitic patch, it can be a candidate for conformal phased array applications.

ACKNOWLEDGMENT

This work was supported partially by the Hi-Tech Research and Development Program of China (Grant No. 2009AA01Z231), partially by the National Natural Science Foundation of China (Grant No. 60872034), and partially by the National Defense Pre-Research Foundation of China (Grant No. 08DZ0229, 09DZ0204).

REFERENCES

[1] A. H. Mohammadian, Noel M. Martin, and Donald W. Griffin, “A theoretical and experimental study of mutual coupling in microstrip antenna arrays,” *IEEE Trans. Antennas Propag.*, vol. 37, pp. 1217–1223, 1989.

[2] C. M. Krowne, “Dielectric and width effect on H-plane and E-plane coupling between rectangular microstrip antennas,” *IEEE Trans. Antennas Propag.*, vol. 31, pp. 39–47, 1983.

[3] R. R. Ramirez and F. De Flaviis, “A mutual coupling study of linear and circular polarized microstrip antennas for diversity wireless systems,” *IEEE Trans. Antennas Propag.*, vol. 51, pp. 238–248, 2003.

[4] N. Jin, A. Yu, and X. X. Zhang, “An enhanced 2×2 antenna array based on dumbbell EBG structure,” *Microwave Opt.Technol. Lett.*, vol. 39, pp. 395–399, 2003.

[5] K. Buell, H. Mosallaei, and K. Sarabandi, “Metamaterial insulator enabled superdirective array,” *IEEE Trans. Antennas Propag.*, vol. 55, pp.1074–1085, 2007.

[6] B.-L. Wu, H. Chen, J. Au Kong, and T. M. Grzegorczyk, “Surface wave suppression in antenna systems using magnetic metamaterial,” *J. Appl. Phys.*, vol. 101, 2007.

[7] D.-B. Hou, S. Xiao, B.-Z. Wang, L. Jiang, J. Wang, and W. Hong, “Elimination of scan blindness with compact defected ground structures in microstrip phased array,” *IET Microw. Antennas Propag.*, vol. 3, pp. 269-275, 2009.

[8] J. J. Pérez and J. A. Encinar, “A simple model applied to the analysis of E-plane and H-plane mutual coupling between microstrip antennas,” *Proc. IEEE AP-S Int. Symp.*, vol. 1, pp. 520-523, 1993.

[9] Ansoft High Frequency Structure Simulation (HFSS), ver. 10, Ansoft Corp., 2005.

Input Impedance Sensitivity Analysis of Patch Antenna with Discrete Perturbations on Method-of-Moment Grids

Yifan Zhang, Natalia K. Nikolova, and Mohamed H. Bakr

Department of Electrical and Computer Engineering
McMaster University, Hamilton, ON L8S 4L8, CANADA
zhangyf98@grads.ece.mcmaster.ca, nikolova@ieee.org, mbakr@mail.ece.mcmaster.ca

***Abstract* —** A new practical approach is proposed to the response sensitivity analysis of high-frequency structures modeled with the method of moments. The response sensitivities are calculated with the self-adjoint approach and discrete shape perturbations on the method of moments grids. The approach requires certain computational effort as a pre-process. This effort is due to building a global system matrix that covers all possible geometrical variations which may arise during design optimization. The technique is illustrated through the sensitivity analysis of the input impedance of a Yagi-Uda array and a printed patch antenna. The computed sensitivities are validated by comparing with the central finite-difference estimates at the response level.

***Index Terms* —** Antenna analysis, frequency-domain, response sensitivity analysis, self-adjoint.

I. INTRODUCTION

The purpose of response sensitivity analysis is to evaluate the sensitivity of the responses of a system to its design parameters. The response sensitivity is represented by the response gradient in the design-parameter space. In high-frequency structure analysis, the design parameters typically describe the geometry and the electromagnetic (EM) properties of the involved materials.

The system response may be defined as: 1) a distributed response represented by the state variables such as current or field distributions; 2) a set of engineering parameters describing the structure's performance such as *S*- or *Z*-parameters; and 3) a single scalar function, which represents a global performance measure, such as the objective function in an optimization problem. The sensitivity information is crucial in gradient based optimization. In this paper, we propose a new technique using method of moments (MoM) grids and the respective current solutions to perform the sensitivity analysis and to carry out gradient optimization.

Our technique is based on the adjoint variable method (AVM). The AVM offers an efficient approach to the design sensitivity analysis of problems of high complexity where the number of state variables is much greater than the number of the required response derivatives [1-10].

Approaches to the sensitivity analysis with the MoM have been developed before [11-13]. There, the analytical formulation of the system matrix derivatives is abandoned as it is impractical for a general sensitivity solver. Instead, the derivatives of the system matrix are estimated with finite differences or the Broyden update. With these approaches, however, the computational speed is still limited due to the following factors: (a) the need to actually compute the perturbed system matrices, and/or (b) the need to perform an adjoint-system analysis, which means one additional full-wave simulation.

A general self-adjoint approach to the sensitivity analysis of network parameters was formulated in [15, 16]. It requires neither an adjoint problem nor analytical system matrix derivatives. An application to the sensitivity analysis of *S*-parameters with the MoM is considered. However, the approach has three drawbacks. First, the computational overhead of the sensitivity is still significant due to the n additional matrix fills for the n perturbed structures. These n matrices are needed to carry out the forward finite differencing of the system matrices. Second with commercial software, users can only have access to the system matrices after they are written on the disk. The time needed to export n+1 large dense system matrices in every iteration (one system matrix for the nominal structure and n system matrices for the perturbed structures) may be significant. Finally, a special mesh control has to be enforced when perturbing the design variables. This is difficult to implement with most existing commercial MoM solvers.

Here, we propose a new self-adjoint sensitivity analysis (SASA) technique with the MoM solutions. This technique uses discrete perturbations of the optimizable shape parameters on a pre-determined MoM grid. The purpose is to aid gradient-based optimization of antenna structures. A global system matrix is calculated only once at the beginning of the analysis. This system matrix covers the whole range of structures (in MoM, these are metallic surfaces), which could be considered during the design optimization. The system matrix of any particular structure arising during optimization is assembled by disabling the elements of the global system matrix corresponding to segments or surfaces which are not metalized.

Take a planar patch antenna as an example. The global system matrix is built for a sufficiently large area, which is discretized into a predetermined number of rectangular subsections. Every structure that is smaller than this large area can be represented by a proper selection of subsections. The patches of the small structure are simply a sub-set of the patches of the large area.

The advantage of the technique is that it accelerates not only the response sensitivity analysis but also the optimization procedure. This is due to the fact that the global matrix is used to assemble quickly not only the perturbed-structure system matrices needed in sensitivity analysis but also the system matrices for all iterates during the optimization.

In Section II, we state the basics of the self-adjoint sensitivity analysis. In Section III, we introduce the discrete perturbation technique on MoM grids. The application of the approach to the sensitivity analysis of a wire array and a printed patch are presented in Section IV. An example of optimizing a printed patch is given in Section V together with comparisons with conventional optimization. The implications and significance of this work are briefly discussed in the conclusions.

II. SELF-ADJOINT SENSITIVITY ANALYSIS

Using the MoM notations, a linear EM system is represented by

$$\boldsymbol{Z}(\boldsymbol{x})\boldsymbol{I} = \boldsymbol{V} \ . \tag{1}$$

Here, $\boldsymbol{x} = [x_1 \ldots x_n]^T$ is the vector of design parameters; $\boldsymbol{Z}$ is the system matrix whose complex coefficients depend on the geometry and the materials; $\boldsymbol{I} = [I_1 \ldots I_m]^T$ is the solution provided by the MoM solver at the nominal design; and $\boldsymbol{V}$ is the excitation vector.

We define a general response function $f(\boldsymbol{x}, \bar{\boldsymbol{I}}(\boldsymbol{x}))$ at the current solution $\bar{\boldsymbol{I}}$ of (1) with respect to the design parameter $\boldsymbol{x}$. The objective of the sensitivity analysis is to obtain the gradient of the system response, i.e.,

$$\nabla_{\boldsymbol{x}} f, \text{ subject to } \boldsymbol{ZI} = \boldsymbol{V} , \tag{2}$$

where $\nabla_{\boldsymbol{x}} f$ is the row operator

$$\nabla_{\boldsymbol{x}} = [\partial/\partial x_1, \partial/\partial x_2, \cdots, \partial/\partial x_n] . \tag{3}$$

Assuming that the $\boldsymbol{Z}$ matrix is not singular, $\nabla_{\boldsymbol{x}}\boldsymbol{I}$ is obtained from (1) as

$$\nabla_{\boldsymbol{x}}\boldsymbol{I} = \boldsymbol{Z}^{-1}\left[\nabla_{\boldsymbol{x}}\boldsymbol{V} - \nabla_{\boldsymbol{x}}(\boldsymbol{Z}\bar{\boldsymbol{I}})\right] . \tag{4}$$

The response gradient $\nabla_{\boldsymbol{x}} f$ of (2) can be written as

$$\nabla_{\boldsymbol{x}} f = \nabla^e_{\boldsymbol{x}} f + \nabla_{\boldsymbol{I}} f \cdot \nabla_{\boldsymbol{x}}\boldsymbol{I} , \tag{5}$$

where $\nabla_{\boldsymbol{I}}$ is a row operator analogous to $\nabla_{\boldsymbol{x}}$ in (3). The gradient $\nabla^e_{\boldsymbol{x}} f$ represents the explicit dependence of $f(\boldsymbol{x}, \bar{\boldsymbol{I}}(\boldsymbol{x}))$ on $\boldsymbol{x}$. Substituting (4) into (5) leads to

$$\nabla_{\boldsymbol{x}} f = \nabla^e_{\boldsymbol{x}} f + \hat{\boldsymbol{I}}^T\left[\nabla_{\boldsymbol{x}}\boldsymbol{V} - \nabla_{\boldsymbol{x}}\left(\boldsymbol{Z}\bar{\boldsymbol{I}}\right)\right] . \tag{6}$$

The adjoint vector $\hat{\boldsymbol{I}}$ is the solution to

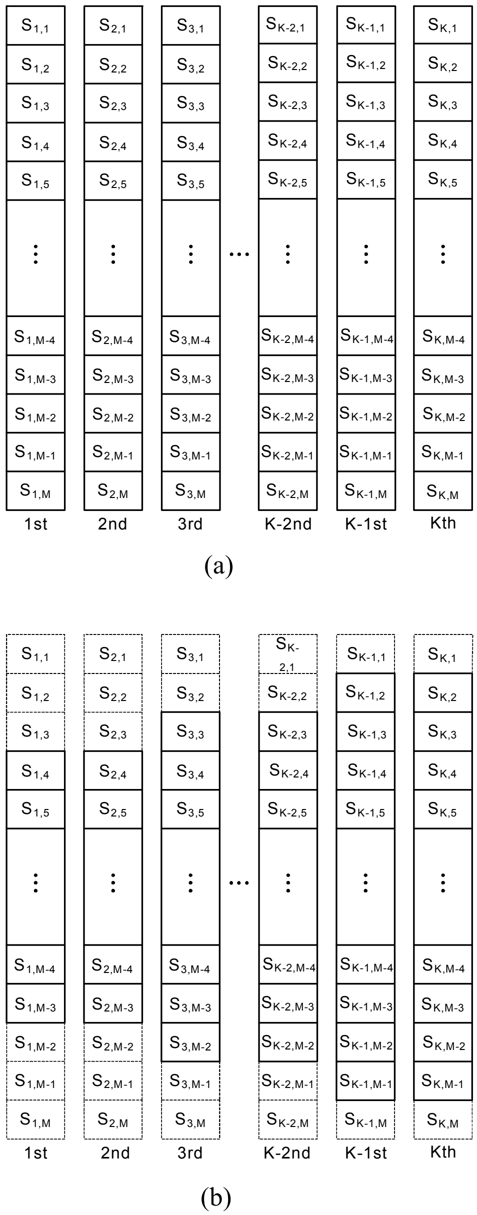

Fig. 1. Discretization of a wire antenna array: (a) the large library structure; (b) the new structure as a sub-set of the library structure. Segments shown with thick line correspond to metal and those shown with dash line correspond to air.

$$\boldsymbol{Z}^T \hat{\boldsymbol{I}} = \hat{\boldsymbol{V}} \,, \tag{7}$$

where

$$\hat{\boldsymbol{V}} = \left[\nabla_{\boldsymbol{I}} f\right]^T \tag{8}$$

is the adjoint excitation [11].

To perform the computations in (6), we need the current solution $\bar{\boldsymbol{I}}$ of (1), the solution $\hat{\boldsymbol{I}}$ of (7), and the system matrix derivatives $\partial \boldsymbol{Z}/\partial x_i$ $(i=1,\ldots,n)$.

The matrix derivatives can be obtained by central finite differences (CFD) as

$$\frac{\partial \boldsymbol{Z}}{\partial x_i} \approx \frac{\boldsymbol{Z}(x_i+\Delta x_i)-\boldsymbol{Z}(x_i-\Delta x_i)}{2\Delta x_i}, \;\; i=1,\ldots,n\,. \tag{9}$$

The shape parameter perturbations Δx_i $(i=1,\ldots,n)$ are equal to the respective segment size in the MoM discrete grid. This is explained in detail in Section III.

The adjoint current $\hat{\boldsymbol{I}}$ is the solution to (7). With the self-adjoint approach, we do not need to solve (7), which would be as computationally demanding as solving (1). From (1) and (7), we see that if the system matrix is symmetric, $\boldsymbol{Z} = \boldsymbol{Z}^T$,[1] and the excitation vectors $\boldsymbol{V}$ and $\hat{\boldsymbol{V}}$ fulfill

$$\hat{\boldsymbol{V}} = c\boldsymbol{V} \,, \tag{10}$$

therefore

$$\hat{\boldsymbol{I}} = c\boldsymbol{I} \,. \tag{11}$$

Here, c is a complex number called the self-adjoint constant. The adjoint simulation is thus avoided. In the case of an antenna input impedance (a response of interest here), the self adjoint constant is [15]

$$c = -I_{in}^{-2} \tag{12}$$

where I_{in} is the current at the feed point of the antenna.

III. DISCRETE PERTURBATION WITH THE METHOD OF MOMENTS

Here, we propose a method for system analysis, which is particularly suitable for design optimization. It is based on deriving a complete set of mutual-coupling coefficients $\boldsymbol{Z}_{i,j}$ (i, j = 1,…, $N_{\max}$), for all possible metallic segments of the antenna structure. This approach reduces the computational load associated with building the system matrices of the optimized structures during the iterative process. It is particularly advantageous in response sensitivity analysis as discussed next.

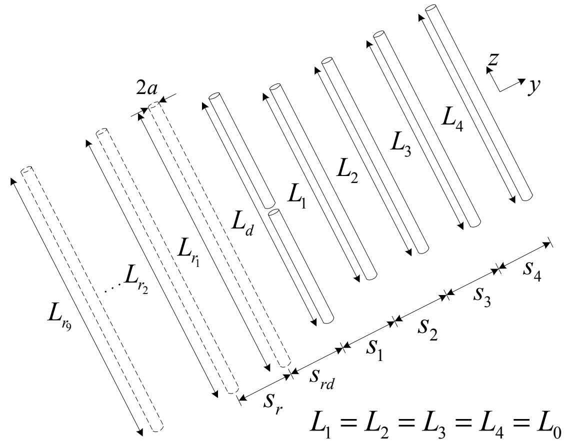

$$L_1 = L_2 = L_3 = L_4 = L_0;$$
$$L_{r_1} = L_{r_2} = \cdots = L_{r_9} = L_r;$$
$$s_1 = s_2 = s_3 = s_4 = s_d.$$

Fig. 2. Six-element Yagi-Uda antenna.

Table 1: Nominal design parameters of the Yagi-Uda antenna

Design parameter	Value
L_0 / λ	0.386
L_d / λ	0.426
L_r / λ	0.604
s_d / λ	0.340
s_{rd} / λ	0.320
s_r / λ	0.050
a / λ	0.003

A sufficiently large structure is built which covers all the possible metallic segments that may be used in the structures arising during the optimization or sensitivity analysis. Its system matrix is referred to as library matrix $\boldsymbol{Z}_{lib}$. Any new structure can be viewed as a sub-set of the library structure. Also, each new system matrix $\boldsymbol{Z}$ can be obtained by switching off the corresponding elements of $\boldsymbol{Z}_{lib}$ and filling the respective rows and columns with zeros. Take a K-element Yagi-Uda array, as an example. We first choose a suitable segment length δ and discretize each wire into M segments as shown in Fig. 1 (a). Thus, $\boldsymbol{Z}_{lib}$ has the dimension of $N_{\max} \times N_{\max}$ ($N_{\max} = K \cdot M$). The new structure has its segments with indices i_1, i_2 ,..., i_k de-metalized. These segments are shown with a dash line in Fig. 1 (b). The new system matrix is obtained by switching off all the

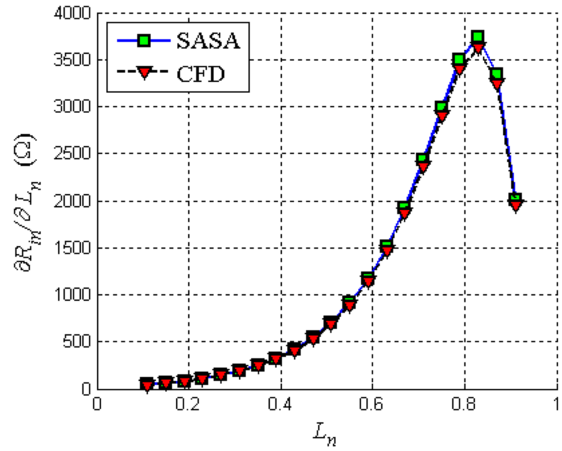

(a)

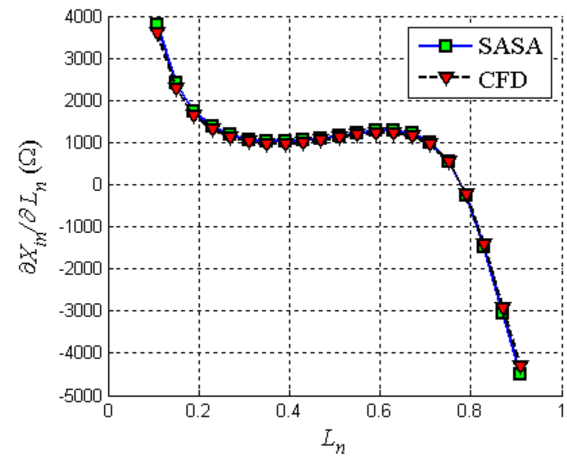

(b)

Fig. 3. Sensitivity of the input impedance of the Yagi-Uda antenna with respect to the normalized length of the driving element: (a) resistance derivative; (b) reactance derivative.

corresponding matrix elements in $\boldsymbol{Z}_{lib}$, i.e., all matrix elements with subscripts containing $i_1, i_2, \ldots, i_k$ are set to zero.

In order to perform the sensitivity calculation in (9), we need to obtain $\boldsymbol{Z}(x_i + \Delta x_i)$ and $\boldsymbol{Z}(x_i - \Delta x_i)$. These are the system matrices of the perturbed antenna structures where the ith parameter is perturbed in the forward and backward directions. Each one of these perturbed-structure $\boldsymbol{Z}$ matrices is obtained from $\boldsymbol{Z}_{lib}$ by switching off "air" segments. Note that all shape parameters are thus constrained to a large but finite set of segment combinations. A typical perturbation Δx_i is equal to one segment length δ (on a uniform MoM grid).

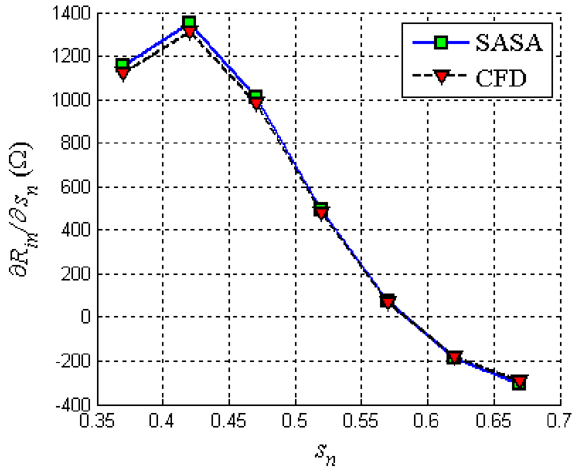

(a)

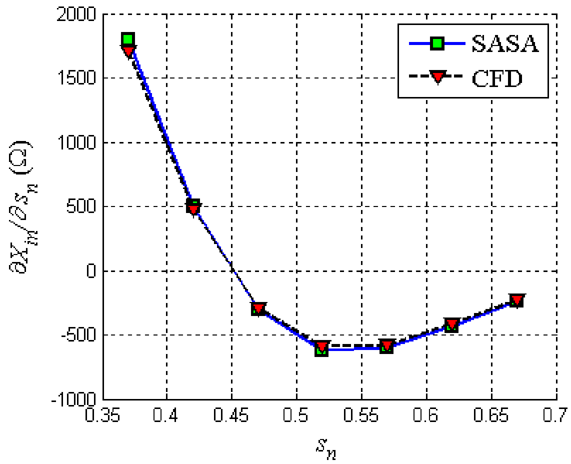

(b)

Fig. 4. Sensitivity of the input impedance of the Yagi-Uda antenna with respect to the distance between the driving element and the reflector: (a) resistance derivative; (b) reactance derivative.

IV. VALIDATION EXAMPLES FOR THE SENSITIVITY ANALYSIS WITH THE MOM

We use a six-element Yagi-Uda array and a printed patch to illustrate the SASA of the input impedance of the two antennas.

A. Sensitivity analysis of a Yagi-Uda array

The size of the library structure in this example is determined by two factors. First, the length of each wire element in the library structure needs to be sufficiently long in order to cover the whole range of lengths allowed in the optimization

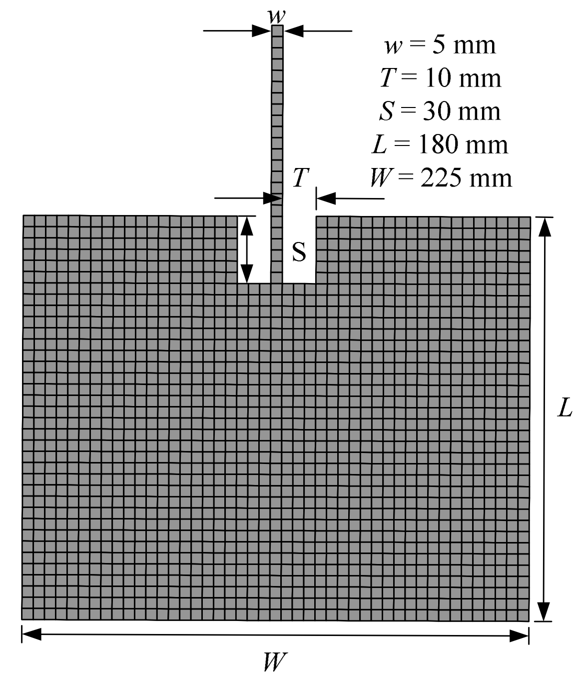

Fig. 5. Library structure of a planar patch.

and needed by the sensitivity analysis. We fix the lengths of all six wire elements to $L=\lambda$, with a radius $a = 0.003\lambda$. Each wire element is discretized into $M=101$ segments. The segment length is thus $\delta=\lambda/M=\lambda/101$. Second in order to perform the sensitivity analysis and optimize with respect to the separation distance between the driving element and the reflector, we assign $K_p=9$ positions at which the reflector can be positioned. These are shown in Fig. 2 with dash lines. The total number of wire elements in the library structure is thus $K_{lib}=K+K_p-1=14$. Therefore, the size of $\boldsymbol{Z}_{lib}$ is $N_{lib} \times N_{lib}$ where $N_{lib} = M \times K_{lib} = 101 \times 14 = 1414$.

After a nominal structure is built and analyzed, its sensitivity analysis is carried out. Its forward and backward perturbed structures with respect to the length of a wire are obtained by adding and subtracting one segment at each wire end. The forward and the backward perturbed structures with respect to the separation are obtained by selecting the neighbouring positions to that of the nominal reflector position. The nominal parameters of the Yagi-Uda array are shown in Table 1. Note that s_r is the fixed distance between

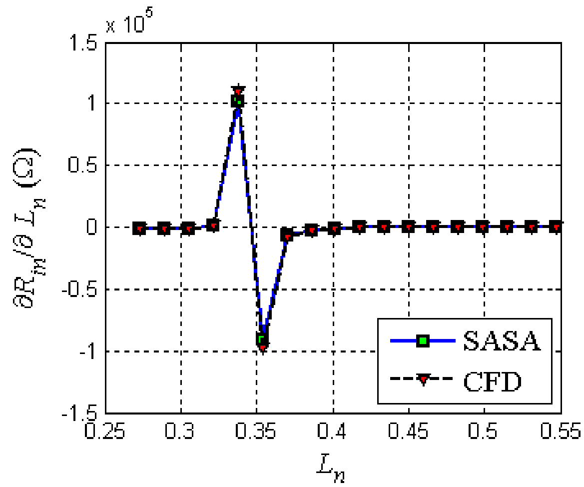

(a)

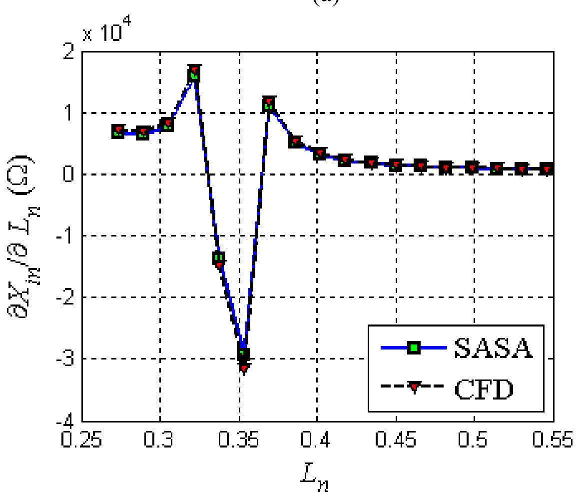

(b)

Fig. 6. Sensitivity of the input impedance with respect to L_n at W_n = 0.66: (a) resistance derivative; (b) reactance derivative.

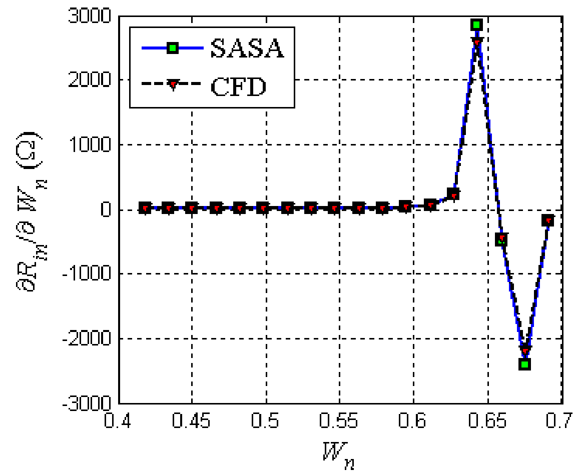

(a)

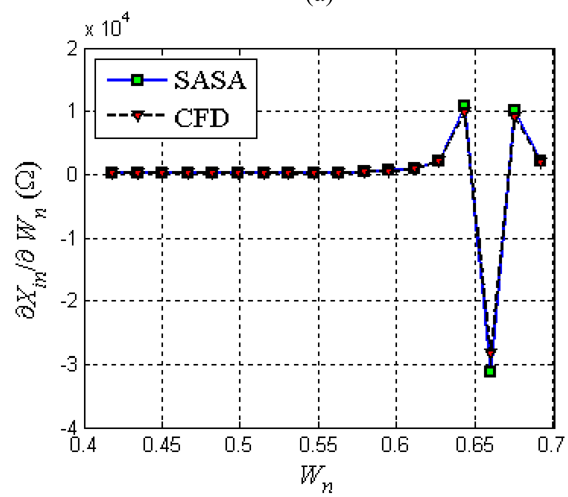

(b)

Fig. 7. Sensitivity of the input impedance with respect to W_n at L_n = 0.48: (a) resistance derivative; (b) reactance derivative.

neighbouring reflector positions [see Fig. 2].

The derivatives of the antenna input impedance are calculated with the proposed approach for a sweep of the length of the driving element. The length of the driving element L_d is swept from 0.1λ to 0.9λ while the separation distance between the driving element and the reflector is fixed at 0.32λ. The results for the derivatives with respect to the normalized lengths of the driver $L_n = L_d/\lambda$ are plotted in Fig. 3. There, two derivative curves are shown. The curves marked with "SASA" are obtained using our approach. The curves marked with "CFD" (center finite difference) are obtained with the perturbation approach where finite differences at the response level are used.

The results plotted in Fig. 4 present the sensitivities with respect to the normalized separation distance $s_n = s_{rd}/\lambda$ between the reflector and the driving element. This distance is swept from 0.37λ to 0.67λ with a step of 0.05λ. The length of the driving element is fixed at $L_d = 0.426\lambda$. The agreement between the adjoint sensitivities and those obtained with finite differences at the response level is excellent as shown in both Fig. 3 and Fig. 4.

B. Sensitivity analysis of a printed patch

The library structure is shown in Fig. 5. Here, we set the edge length of the square subsection to be δ = 5.0 mm. The length of the library structure is L = 36δ = 180.0 mm and its width is W = 45δ = 225.0 mm. Sensitivity analysis is carried out with respect to the length and width of the patch antenna. The forward and backward perturbed structures with respect to the length of the patch are obtained by adding and subtracting one line of subsections at the patch edge opposite to the feeding-point edge. The forward and the backward perturbed structures with respect to the width of the patch are obtained by adding and subtracting one line of subsections at both sides of the patch. The nominal design parameters of the patch are shown in Fig. 5.

The analysis is carried out at the frequency f_0 = 0.97 GHz. The derivatives of the antenna input impedance are calculated with the proposed approach for a sweep of the length of the patch. The length L is swept from 0.27λ to 0.55λ while the width of the patch is fixed at W_n = W/λ = 0.66. Here, λ is the wavelength in air. The results for the derivative with respect to the normalized length of the patch L_n = L/λ are plotted in Fig. 6. The results shown in Fig. 7 present the sensitivities with respect to the normalized width of the patch W_n = W/λ which is swept from 0.42λ to 0.69λ while the length is fixed at L_n = L/λ = 0.48. Again, excellent agreement is observed between the sensitivities calculated with the proposed approaches and those calculated with response-level finite differences.

Note that in calculating the CFD sensitivity, two additional EM simulations have to be performed per parameter. In obtaining the adjoint sensitivity, the calculation involves only two matrix subtractions and a vector-matrix-vector multiplication. Thus, our approach is much faster than the CFD method.

V. DESIGN OPTIMIZATION EXAMPLE

We use the technique described above to optimize the input impedance of the planar patch antenna shown in Fig. 5. The objective function is defined as

$$f(\boldsymbol{x}) = \left| \frac{Z_{in} - \bar{Z}}{\bar{Z}} \right|, \qquad (13)$$

where $\bar{Z} = 50\,\Omega$ and Z_{in} is the input impedance of the antenna. The vector of design parameters is $\boldsymbol{x} = [L, W]^T$. The values of the rest of the design parameters are fixed at those given in Fig. 5. The objective function (13) depends on a single complex-valued current I_f at the feed-point. The input impedance is then calculated with $Z_{in} = V_f / I_f$, where $V_f = 1$ V. The relation between $\nabla_x f$ and $\nabla_x Z_{in}$ is given by

$$\nabla_x f = \mathrm{Re}\left[\frac{1}{\bar{Z}} \cdot \frac{(Z_{in} - \bar{Z})^*}{|Z_{in} - \bar{Z}|} \cdot \nabla_x Z_{in} \right]. \qquad (14)$$

The sensitivity $\nabla_x Z_{in}$ is calculated by our proposed approach. The optimization is implemented by using the Matlab function *fmincon*, whose algorithm is based on the line-search method with sequential quadratic programming (SQP). At each iteration, the SQP sub-problem is solved and its solution is used to define a search direction.

For comparison, the optimization is carried out in two separate procedures using two different methodologies: a) optimization with the sensitivity information offered by our self-adjoint method and using the library matrix $\boldsymbol{Z}_{lib}$; b) optimization without the sensitivity information and without using the $\boldsymbol{Z}_{lib}$ matrix.

A. Design optimization with sensitivity information and pre-calculated library matrix

The frequency of interest is f_0 = 0.97 GHz. The initial design is set to $\boldsymbol{x} = [165, 195]^T$ mm. The EM solver [17] is used to compute the library matrix $\boldsymbol{Z}_{lib}$. It is, also, called by the optimization algorithm to compute the input impedances of the antenna design iterates. The system matrices of these iterates are obtained by switching on and off the corresponding elements of the library matrix according to the geometry information provided by the optimizer. The optimization process converges after 4 iterations with an optimal design $\boldsymbol{x}^* = [175, 205]^T$ mm and objective function $f(\boldsymbol{x}^*) = 0.098$. The progress of the optimization is shown in Fig. 8. Only four optimization iterations are needed. During these iterations, the EM solver is called 14 times. The values of the design parameters as well as the values of the input impedance, and the objective function are listed in Table 2.

Table 2: Design parameters, input impedance, and objective function in the optimization with sensitivity information and using the $\boldsymbol{Z}_{lib}$ matrix

	L	W	R_{in}	X_{in}	f
0	165	195	9.96	411.09	8.261
1	175	210	7.24	190.88	3.912
2	170	205	53.6	-16.60	0.340
3	175	205	50.1	4.90	0.098
4	175	205	50.1	4.90	0.098

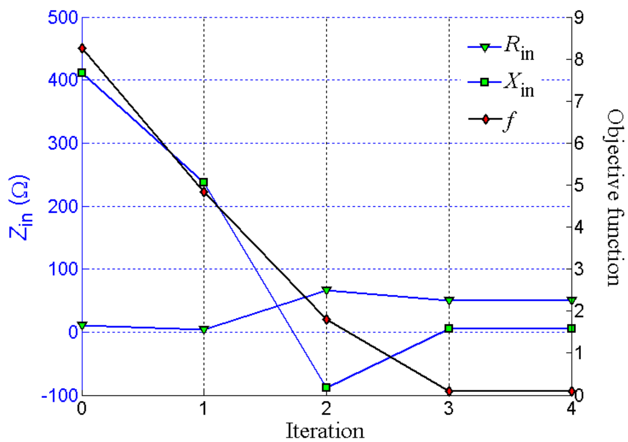

Fig. 8. Progress of the objective function and the input impedance during the optimization with sensitivity information.

B. Design optimization without sensitivity information and pre-calculated library matrix

In order to illustrate the efficiency of the gradient-based design optimization with sensitivity information, we present a conventional optimization without the sensitivity information and without the use of $\boldsymbol{Z}_{lib}$. The conventional approach has the same settings, except that the gradient is not provided to the optimizer. The system matrices are built by the EM solver for each particular structure. Optimization starts with the same initial values. After 23 calls to the EM solver (6 iterations), the result converges to an optimal design $\boldsymbol{x}^* = [175, 205]$ mm and objective function $f(\boldsymbol{x}^*) = 0.098$. The progress is shown in Fig. 9 and the design parameters are given in Table 3.

C. Comparison between the two optimization procedures

For the optimization with the proposed approach, the computational overhead is due to two calculations: 1) filling the system matrix $\boldsymbol{Z}_{lib}$ at the beginning of the optimization; and 2) solving

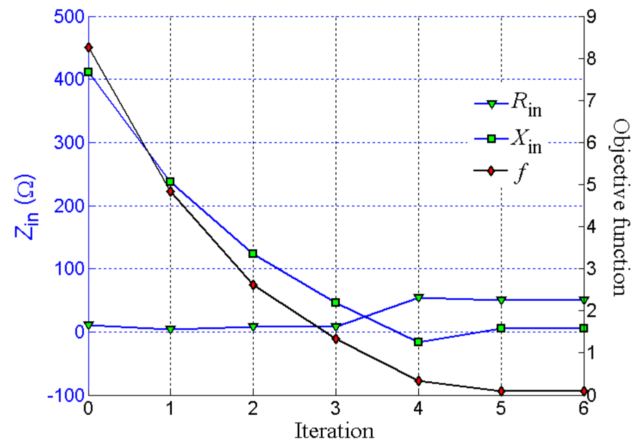

Fig. 9. Progress of the objective function and the input impedance during the optimization without sensitivity information.

Table 3: Design parameters, input impedance, and objective function in the optimization without sensitivity information and without using the $\boldsymbol{Z}_{lib}$ matrix

	L	W	R_{in}	X_{in}	f
0	165	195	9.96	411.09	8.261
1	175	215	3.33	237.69	4.845
2	165	205	7.48	123.62	2.615
3	165	210	7.71	45.94	1.324
4	170	205	53.61	-16.60	0.340
5	175	205	50.1	4.90	0.098
6	175	205	50.1	4.90	0.098

Table 4: Comparison between the computational overhead of the gradient-based optimization with and without sensitivity information / library matrix

	Proposed approach	Conventional approach
Iterations	4	6
Call for solver	14	23
Matrix fill time (s)	3.9	66.8
Solve system time (s)	52.0	80.6
Total CPU time (s)	55.9	147.4

the linear system of the nominal structure at each simulation call. In the second approach, the computational overhead at each call to the simulator is due to: 1) matrix fill, and 2) solving the system of equations. The comparison between the two approaches is shown in Table 4 in terms of: 1) the number of iterations, 2) the number of calls for EM simulations, 3) the CPU time for matrix fill, 4) the CPU overhead for solving the system, and 5) the total CPU overhead. It is evident that the optimization process with our approach converges faster and takes shorter time.

VI. CONCLUSION

A new approach to self-adjoint sensitivity analysis with discrete perturbations on MoM grids is proposed. The technique aims at computationally efficient gradient-based optimization of antenna structures analyzed by the MoM. A large system matrix (the "library matrix") is computed only once at the beginning. This matrix is then used for rapid sensitivity calculations as well as for quick matrix-building for the structures arising during the optimization.

ACKNOWLEDGMENT

The author would like to thank Dr. J. Rautio and Dr. S. Arvas, Sonnet Software, North Syracuse, NY, USA, and the team at Sonnet Support, North Syracuse, NY, USA, for their patience and help regarding the technical details in handling the exported data from the Sonnet simulator.

REFERENCES

[1] E. J. Huang, K. K. Choi, and V. Komkov, *Design Sensitivity Analysis of Structural Systems*, Orlando, FL, Academic, 1986.

[2] S. W. Director and R. A. Rohrer, "The generalized adjoint network and network sensitivities," *IEEE Trans. Circuit Theory*, vol. CT-16, pp. 318–323, Aug. 1969.

[3] H.-B. Lee and T. Itoh, "A systematic optimum design of waveguide-to-microstrip transition," *IEEE Trans. Microwave Theory Tech.*, vol. 45, pp. 803–809, May 1997.

[4] J. P. Webb, "Design sensitivity of frequency response in 3-D finite-element analysis of microwave devices," *IEEE Trans. Magn.*, vol. 38, pp. 1109–1112, Mar. 2002.

[5] N. K. Nikolova, J. W. Bandler, and M. H. Bakr, "Adjoint techniques for sensitivity analysis in high-frequency structure CAD," *IEEE Trans. Microwave Theory Tech.*, vol. 52, pp. 403–419, Jan. 2004.

[6] S. M. Ali, N. K. Nikolova, and M. H. Bakr, "Recent advances in sensitivity analysis with frequency-domain full-wave EM solvers," *Applied Computational Electromagnetics Society Journal*, vol. 19, pp. 147–154, Nov. 2004.

[7] M. H. Bakr and N. K. Nikolova, "An adjoint variable method for frequency domain TLM problems with conducting boundaries," *IEEE Microwave and Wireless Components Letters*, vol. 13, pp. 408–410, Sep. 2003.

[8] N. K. Nikolova, X. Zhu, Y. Song, A. Hasib, and M. H. Bakr, "S-parameter sensitivities for electromagnetic optimization based on volume field solutions," *IEEE Trans. Microwave Theory Tech.*, vol. 57, no. 6, pp. 1526–1538, Jun. 2009.

[9] P. Zhao, M. H. Bakr, and N. K. Nikolova, "Adjoint first order sensitivities of transient responses and their applications in the solution of inverse problems," *IEEE Trans. Antennas Propagat.*, vol. 57, no. 7, pp. 2137–2146, July 2009.

[10] P. A. W. Basl, M. H. Bakr, and N. K. Nikolova, "Efficient transmission line modeling sensitivity analysis exploiting rubber cells," *Progress In Electromagnetic Research B*, vol. 11, pp. 223–243, 2009.

[11] N. K. Georgieva, S. Glavic, M. H. Bakr, and J. W. Bandler, "Feasible adjoint sensitivity technique for EM design optimization," *IEEE Trans. Microwave Theory Tech.*, vol. 50, pp. 2751–2758, Dec. 2002.

[12] N. K. Nikolova, R. Safian, E. A. Soliman, M. H. Bakr, and J. W. Bandler, "Accelerated gradient based optimization using adjoint sensitivities," *IEEE Trans. Antennas Propagat.*, vol. 52, pp. 2147–2157, Aug. 2004.

[13] E. A. Soliman, M. H. Bakr, and N. K. Nikolova, "Accelerated gradient-based optimization of planar circuits," *IEEE Trans. Antennas Propagat.*, vol. 53, no. 2, pp. 880–883, Feb. 2005.

[14] J. W. Bandler, Q.-J. Zhang, J. Song, and R. M. Biernacki, "FAST gradient based yield optimization of nonlinear circuits," *IEEE Trans. Microwave Theory Tech.*, vol. 38, pp. 1701−1710, Nov. 1990.

[15] N. K. Nikolova, J. Zhu, D. Li, M. H. Bakr, and J. W. Bandler, "Sensitivity analysis of network parameters with electromagnetic frequency domain simulators," *IEEE Trans. Microwave Theory Tech.*, vol. 54, pp. 670−677, Feb. 2006.

[16] D. Li, J. Zhu, N.K. Nikolova, M.H. Bakr, and J.W. Bandler, "Electromagnetic optimization using sensitivity analysis in the frequency domain," *IET Microw. Antennas Propag.*, vol. 1, no. 4, pp. 852–859, Aug. 2007.

[17] *Sonnet em User's Manual*, *Suites 12.52*, Sonnet Software, Inc., North Syracuse, NY, Dec. 2009. Available: http://www.sonnetsoftware.com/.

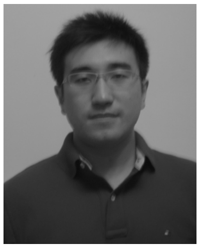

Yifan Zhang received the B. Eng. degree (with honors) in electrical engineering from Harbin Institute of Technology, Harbin, China, in 2008, and is currently working toward the Ph.D. Degree at McMaster University, Hamilton, Canada.

In September 2008, he joined the Computational Electromagnetics Research Laboratory, Department of Electrical and Computer Engineering, McMaster University, where he is currently a Teaching Assistant. His research interests include computational EM, computer-aided design for high frequency structures and antennas, EM optimization, and microwave image.

Natalia K. Nikolova received the Dipl. Eng. degree from the Technical University of Varna, Varna, Bulgaria, in 1989, and the Ph.D. degree from the University of Electro-Communications, Tokyo, Japan, in 1997.

From 1998 to 1999, she was with the Natural Sciences and Engineering Research Council of Canada (NSERC), during which time she was initially with the Microwave and Electromagnetics Laboratory, DalTech, Dalhousie University, Halifax, NS, Canada, and then for a year with the Simulation Optimization Systems Research Laboratory, McMaster University, Hamilton, ON, Canada. In July 1999, she joined the Department of Electrical and Computer Engineering, McMaster University, where she is currently a Professor. Her research interests include theoretical and computational electromagnetism, microwave methods for imaging and detection, as well as the computer-aided design of high-frequency structures and antennas.

Dr. Nikolova is a member of the Applied Computational Electromagnetics Society. She is also an International Union of Radio Science (URSI) correspondent, Commissions B and D. She was the recipient of an NSERC Post-Doctoral Fellowship from 1998 to 1999. She held a University Faculty Award of the NSERC from 2000 to 2005 and is currently Canada Research Chair in High-frequency Electromagnetics.

Mohamed H. Bakr received the B.Sc. degree in electronics and communications engineering with distinction (honors) and the M.Sc. degree in engineering mathematics from Cairo University, Cairo, Egypt, in 1992 and 1996, respectively, and the Ph.D. degree from McMaster University, Hamilton, ON, Canada, in 2000.

In 1997, he was a student intern with Optimization Systems Associates Inc. (OSA), Dundas, ON, Canada. From 1998 to 2000, he was a Research Assistant with the Simulation Optimization Systems (SOS) Research Laboratory, McMaster University. In November 2000, he joined the Computational Electromagnetics Research Laboratory (CERL), University of Victoria, Victoria, BC, Canada, as a Natural Sciences and Engineering Research Council of Canada (NSERC) Post-Doctoral Fellow. He is currently an Associate Professor with the Department of Electrical and Computer Engineering, McMaster University. His research areas of interest include optimization methods, computer-aided design and modeling of microwave circuits, neural-network applications, smart analysis of microwave circuits, and efficient optimization using time-/frequency-domain methods.

Dr. Bakr was a recipient of the Premier's Research Excellence Award (PREA) presented by the Province of Ontario, Canada, in 2003.

A Microstrip Directional Coupler with Tight Coupling and Relatively Wideband using Defected Ground Structure

Ayman S. Al-Zayed [1], Zuhair. M. Hejazi [2], and Ashraf S. Mohra [2]

[1] Electrical Engineering Department
Kuwait University, University, P.O. Box 5969, Safat, 13060, Kuwait
ayman.alzayed@ku.edu.kw

[2] Electrical Engineering Department
King Saud University, Saudi Arabia
zhejaz@ksu.edu.sa, amohra@ksu.edu.sa

***Abstract*─** This paper presents a detailed investigation utilizing a defected ground structure (DGS) to a conventional edge-coupled microstrip coupler with tight coupling level over a relatively wide frequency band. A reasonable spacing between microstrip coupled lines and stronger coupling are achieved using this technique. A 20 dB initial coupler (over a fractional bandwidth of 35% with ±1dB ripple) is converted into 8 dB coupler with almost 3 times wider band by etching off a single unit cell of rectangular and meandered slot loop in the ground plane under the central part of the coupling region. Optimum DGS dimensions are related to coupler dimensions in easy to use design curves. An efficient technique for compensation of the significant unavoidable mismatch resulting from the presence of the DGS is applied and tested. Some coupler samples with different DGS are fabricated, measured, and compared with a conventional coupler counterpart to verify the simulation results and illustrate the improvements, very good agreements are observed.

***Index Terms*─** Defected ground structures, directional coupler, microstrip, wideband.

I. INTRODUCTION

Couplers are essential components for applications in virtually all RF and microwave transmission systems, such as power and VSWR measurements, signal sampling for monitoring or testing, equal or unequal power division, phase shifting (particularly 90^0 and 180^0), feed-forward signal injection, isolation of signal sources. Other applications with the highest possible performance are particularly required in instrumentation, such as the new version of vector network analyzers require couplers with wide bandwidth, flat frequency response, and long-term stability [1].

In recent years, a growing research interest has been shown in applying various shapes of defected ground structures (DGS) to improve the performance of microwave circuits, such as microstrip filters and couplers. DGS are achieved by etching off a defected pattern from the ground plane of the microstrip line. Such structures disturb the current distribution in the ground plane and hence, introducing higher effective inductance and capacitance of the microstrip circuit, and reject certain frequency bands. A design of the lowpass filter using microstrip defected ground structure has been first proposed by Ahn et al. [2] in 2001. Numerous publications have applied the DGS in lowpass filter [2-6], and in directional coupler designs [7-10]. Hong et al. [11] proposed a general circuit model that represents varieties of DGS in either microstrip or coplanar waveguide (CPW).

It is commonly known that higher coupling in conventional microstrip couplers can be achieved by tightening the spacing between the coupled lines which is limited by fabrication tolerance. Sharma et al. [10] demonstrated an edge-coupled coupler with reasonable spacing between lines and improved coupling by introducing a rectangular slot in the ground plane under the coupler lines. Burokur et al. [7] realized a narrow band coupler by using the inverted slot split-ring resonators

1054-4887 © 2010 ACES

(SSRR). Liu et al. [8] has proposed a microstrip coupler with complementary split-ring resonator (CSRR), to achieve a 3 dB coupling over a fractional bandwidth of only 38.1%. With utilizing the properties of electromagnetic bandgap structure (EBG), Wu et al. [9] improved the coupling of a microstrip coupler by using cascaded EBG and showed a broader coupling band.

Other works have used other methods rather than DGS such as inductor loading to enhance the directivity and the bandwidth as Seungku et al. [12] for a bandwidth of 16.3% at 2.4 GHz or using multi-section asymmetric directional coupler as Gruszczynski et al. [13] to achieve 4 GHz bandwidth at 3 GHz center frequency.

Dong et al. [14] has used a DGS technique on a CPW directional coupler design and achieved only 1 GHz bandwidth (50% fractional bandwidth at 2 GHz center frequency). Conventional edge-coupled microstrip coupler design, applying floating-plate overlay (not DGS), can be found in Kuo-Sheng et al. [15] for a one-section (one-stage) 3-dB and three-section (three-stages) 6 dB directional couplers over a bandwidth of 1 to 2 GHz (54% and 94% fractional bandwidth, respectively). Abbosh [16] demonstrated a 3 dB coupling coefficient over a wide bandwidth by converting an initial 7 dB conventional coupler, which implies a 4 dB coupling gain. This is achieved by applying a DGS of a floating potential plate in the ground plane. However, the coupled line spacing of only 0.13 mm still seems to be tight. The mismatch introduced by the DGS and restoring it to acceptable levels may also need to be addressed.

In this paper, a simplified approach, for systematic control of the coupler characteristics, is presented. This approach provides a much more relaxed line spacing and compensated mismatch caused by the presence of DGS. The DGS geometrical parameters are related to the geometry of any desired initial coupler through several extracted design curves which enables the designer to identify the trade-offs between geometry and performance parameters. The investigation includes DGS geometries from rectangular slot area to rectangular slot loop and meandered versions of slot loops. The mismatch caused by the DGS that deteriorates the refection and isolation scattering parameters was compensated by inserting a narrow notch in the feed arms of the initial coupler in addition to mitering the corners with the feed lines. Full-wave EM simulation tools [17-18] are used in the study. Samples of the proposed couplers are fabricated, measured, and compared and their results have very good agreements.

II. DESIGN AND GEOMETRY

Before starting with the geometrical details of the coupler and related DGS design to be used in the simulations, it is useful to discuss some concepts of the DGS and its effects on the properties of the microstrip line.

A. Design considerations

A DGS in the ground is a kind of slot, regardless of its shape: a line slot, rectangular slot area, slot loop, dumbbell etc., and single or periodic, all exhibit multi stop bands in frequencies [11].

It is known that the presence of the DGS modifies the properties of the microstrip line such as characteristic impedance and propagation constant. Thus, a disturbance of the already setup matching is expected. The simplest general equivalent circuit of a DGS can be presented in parallel *LC* circuit resonators, which can also be obtained from cutoff and attenuation frequencies obtained from the field analysis or the experimental measurement.

The coupled microstrip lines support two propagation modes denoted as even and odd modes. In the even mode, the electric field is symmetric, and the DGS may act as an open circuit, consequently slowing down the signal phase velocity, something like passing through a series stub. While in the odd mode, the electric field is asymmetric and the slot behaves something like a short circuit, where the signal can simply pass through without slowing down its phase velocity which is the same as if the DGS is absent. When the phase velocity decreases as is the case in the even mode, the effective dielectric constant increases. In this way, the microstrip properties are modified by the DGS, so the coupling coefficient may, also, be controlled by the shape and dimensions of the DGS. A simple equation illustrating such a control is given from the proportionality [19]

$$\left|S_{31}\right| \propto \Delta n_{eff} = \sqrt{\varepsilon_{r_{effe}}} - \sqrt{\varepsilon_{r_{effo}}}\ , \qquad (1)$$

where $|S_{31}|$ is the magnitude of the coupling coefficient, while the ε_{reffe} and ε_{reffo} are the effective dielectric constant for the even and odd modes, respectively.

B. Design geometry

The initial microstrip coupler (without DGS) is designed using conventional synthesis technique [20-22]. The well known design steps are used assuming symmetrical two-line microstrip directional coupler. The coupler was designed on RT/Duroid 5880 (ε_r = 2.2, h = 1.5748 mm) with -20 dB coupling coefficient at center frequency of 2 GHz.

The coupling level is deliberately chosen, so to obtain enough spacing and reasonable line width to ease the fabrication lithography process. The geometrical dimensions, Fig.1, are (W_C = 4.8 mm), (S_C = 1.8 mm), and (L_C = 36 mm) which are the width of the lines in the coupled region, the separation between the coupled lines, and the coupling length of the coupler, respectively.

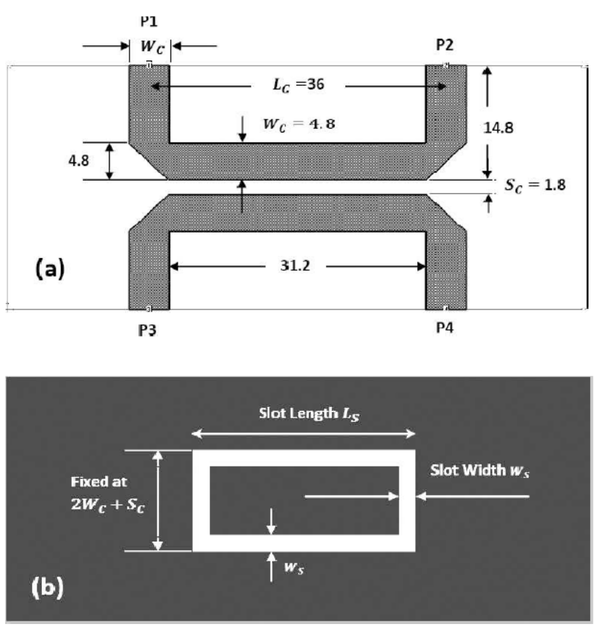

Fig. 1. Initial microstrip coupler with DGS. All dimensions are in mm. (a) Geometry of the -20 dB coupler. (b) DGS rectangular slot loop.

For preliminary investigation, the DGS structure, chosen to be applied with this initial coupler, is a rectangular slot loop shown in Fig. 1 (b). The parameters are denoted as: slot length (L_S), slot width (W_S), and the slot side ($2W_C + S_C$) that is maintained fixed in all investigations. The other dimensions are made variables during the optimization process as will be shown in next sections.

III. SIMULATION RESULTS

The simulated frequency response of the initial microstrip coupler without DGS, that has a finite ground plane, is shown in Fig. 2. It achieves -20 dB coupling around the operating frequency 2 GHz as specified with acceptable transmission, isolation, and reflection coefficients. The effect of varying the DGS slot loop length and width will be discussed next.

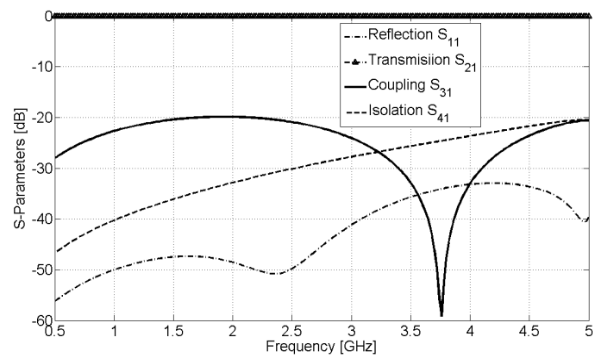

Fig. 2. Simulated S-Parameters of the -20 dB initial coupler without DGS, designed at 2 GHz.

A. Effect of the DGS slot loop dimensions

Preliminary investigations showed that a reasonable slot loop width of (W_S = 1.2 mm) can be used as a starting parameter. The slot loop length (L_S) is then altered from zero up to nearly the coupling length (L_C). Note that when (L_S = 0), the DGS vanishes and the coupler is returned back to its original initial microstrip structure.

The DGS geometrical parameters are illustrated in Fig. 3, where two investigations will be conducted to gain insight in designing the DGS and to achieve the optimal design in terms of all scattering parameters. In Fig. 3 (a), the slot loop width (W_S) is fixed at 1.2 mm, while in Fig. 3 (b), the slot length (L_S) is fixed at 24 mm.

For convenience of extracted data, normalized values are used such as normalized slot length to coupling length (L_S / L_C) and normalized slot width to coupled line width (W_S / W_C). This is essential to relate the DGS dimensions with the initial coupler dimensions. Figure 4 illustrates the simulated S-parameters against the normalized slot length to coupling length (L_S / L_C) at fixed ratio of slot width to coupling width (W_S / W_C = 0.25). Figure 5 illustrates the simulated S-parameters against the normalized slot width to coupling width (W_S / W_C) at fixed ratio of slot length to coupling length ($L_S / L_C = 1$).

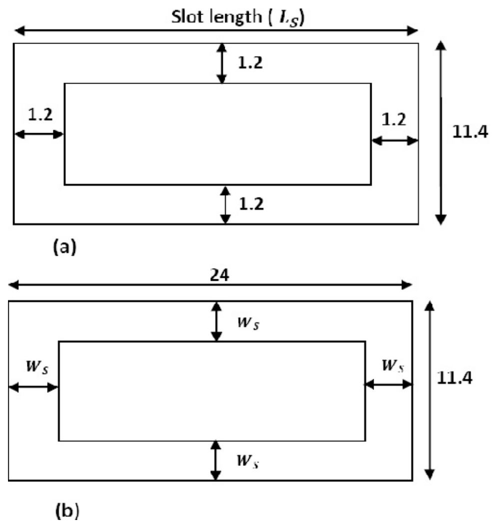

Fig. 3. DGS geometry. (a) Variation of (L_S) at fixed (W_S). (b) Variation of (W_S) at fixed (L_S).

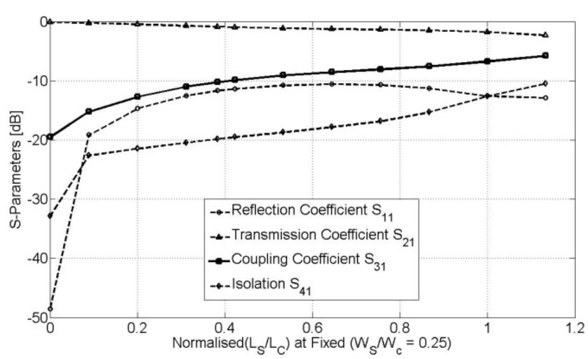

Fig. 4. The S-parameters against normalized (L_S / L_C) at fixed ratio ($W_S / W_C = 1/4$).

From these plots (Fig. 4 and Fig. 5), although an immediate increase in the coupling from -20 dB to around -7 dB is observed, it can be clearly seen that this increase in coupling is associated with a significant deterioration of reflection and isolation coefficients S_{11} and S_{41}. Such deterioration would make the coupler useless. This is due to a significant mismatch caused by applying the DGS beneath the coupler which confirms the concepts mentioned in the design considerations in Section II. A. However, it can also be seen that the effect of slot length variations is stronger than the effect of the slot width. This may be due to the fact that increasing the slot length, actually increases the metallic conductor area beneath the coupler lines and affects the electric field distribution of the structure; hence, the odd mode capacitance of the structure will increase. Increasing the slot width, on the hand, reduces the conductor area beneath the coupler lines. As a result, an opposite effect occurs on both even and odd modes capacitances (see also the discussions in Section II).

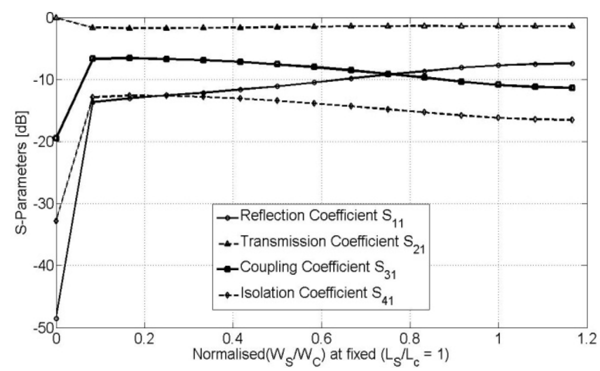

Fig. 5. The S-parameters against (W_S / W_C) at fixed ratio of (L_S / L_C =1).

To complete this preliminary study, the effect of slot length and width variations on the coupler fractional bandwidth (B%) are shown in Fig. 6. In fact, the very large fractional bandwidth of the coupling above 90% is associated with the worst S_{11} and S_{41}, as expected. Also, the slot length effect on the bandwidth is much stronger than the slot width effect.

It should be noted that the variations of S-parameters due to slot dimensions are larger in the higher frequency region than in the lower frequency region. This may be due to the difference in phase velocities of the odd and even modes of the coupler.

To acquire better insight on the extent of the resulting mismatch in the reflection coefficient S_{11} (even with the improvement of the coupling coefficient S_{31} over a wide frequency band), several simulations for S_{11} and S_{31} responses, are plotted in Fig. 7 to illustrate these effects.

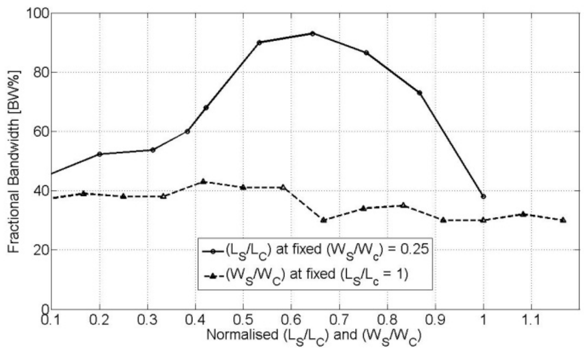

Fig. 6. Fractional bandwidth (B%) against (L_S / L_C) and (W_S / W_C) at fixed ratios of (W_S / W_C = 1/4) and (L_S / L_C =1) respectively.

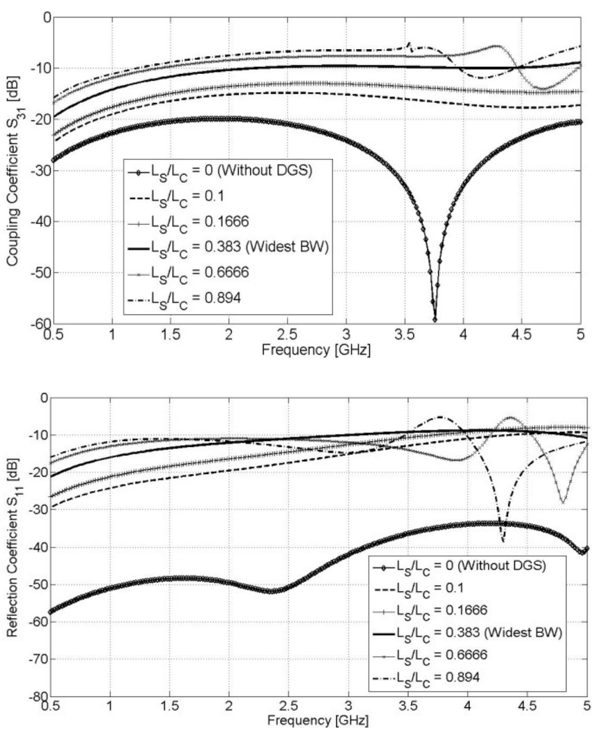

Fig. 7. The coupling and reflection coefficients against frequency at different values (L_S / L_C) at fixed ratio of (W_S / W_C = 1/4).

B. Mismatch compensation of the DGS coupler

The presence of the DGS modifies some properties of the microstrip line including the coupling coefficient, but at the same time deteriorates both the reflection coefficient S_{11} and isolation coefficient S_{41}. Thus, the already matched initial coupler is expected to deteriorate its reflection S_{11} and isolation coefficient S_{41}, although the coupling bandwidth has improved. To restore the S_{11} and S_{41} Performance, while maintaining a wide bandwidth and relatively flat coupling response, mismatch compensation should be achieved. Thus, the coupler feed arms are modified with a narrow notch and increased depth of the corner mitering as shown in Fig. 8 (a). Figure 8 (b) shows the DGS geometrical parameters used in the subsequent simulations. Therefore, it is important to investigate the impact of this mismatch compensation method on the other scattering parameters of the coupler.

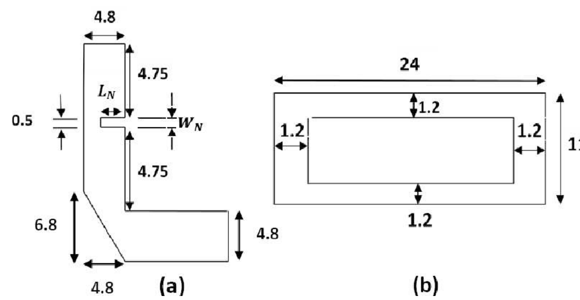

Fig. 8. Geometry of the notch length (L_N) and associated DGS of the coupler.

The effect of the notch feed lines and mitered corners, on S-parameters of the modified coupler, is shown in Fig. 9. The normalized notch length to coupler width (L_S / W_C) is varied at fixed notch width (W_N / W_C ≈1).

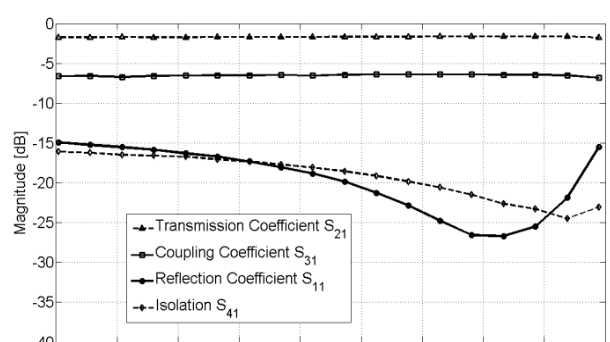

Fig. 9. Effect of the notch and mitering on the scattering parameters of the modified coupler, against (L_S / W_C) at fixed ratio of (W_N / W_C ≈1).

The improvement on S_{11} and S_{41} is evident in the limits ($0.65 \leq L_N / W_C \leq 0.85$), while the other parameters remain almost unchanged. The optimum notch length is chosen to be 4 mm, i.e. ($L_N / W_C = 0.833$). That gives a broader coupling coefficient.

The modified coupler is shown in Fig. 10, while the S-parameters with respect to (L_S / L_C) at ($W_S / W_C = 1/4$) are shown in Fig. 11, where the notch is fixed at length of 4 mm and width of 0.5 mm. From Fig. 11, it can be seen that when the ratio of ($L_S / L_C = 2/3$), a better performance of S_{11} and S_{41} has been occurred, so the slot length (L_S) will be equal to 24 mm. This value is adopted as optimum for the investigations.

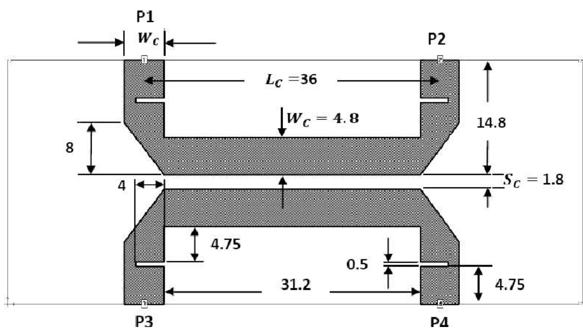

Fig. 10. Geometry of the modified initial coupler with a notch in feed arms. All dimensions are in mm.

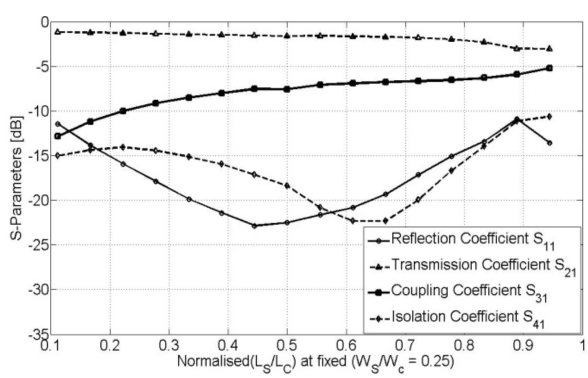

Fig. 11. Variation of *S*-parameters of the modified coupler against (L_S / L_C) at fixed ($W_S / W_C = 1/4$). The notch dimensions are 4 mm x 0.5 mm.

Now, it is worth monitoring the variations of fractional bandwidth (B%) for the coupler (Fig. 10) against the ratios (L_S / L_C), and (W_S / W_C) at fixed ratios ($W_S / W_C = 1/4$), and ($L_S / L_C = 2/3$) respectively. These relationships are illustrated in Fig. 12 where the effect on (B%) by varying the slot width is much smaller than the effect of varying the slot length. The best (B%) is somewhere about a value of ($L_S / L_C = 2/3$) at fixed value of ($W_S / W_C = 1/4$), i.e. a slot length of L_S = 24 mm and slot width of W_S = 1.2 mm. These values are adopted for the coupler to be fabricated and measured.

The variation of *S*-parameters of the coupler (Fig. 10) against normalized slot width (W_S / W_C) at fixed ratio of slot length ($L_S / L_C = 2/3$), is shown in Fig. 13. The variations are relatively slight in comparison to those due to slot length variation.

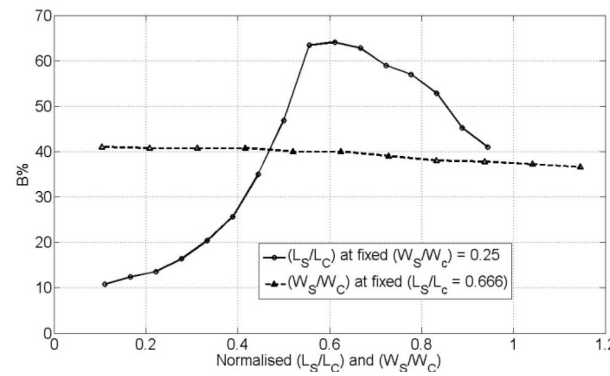

Fig. 12. Variation of (B%) of the coupler (Fig. 10), against (L_S / L_C), and (W_S / W_C) at fixed ratios of ($W_S / W_C = 1/4$), and ($L_S / L_C = 2/3$), respectively.

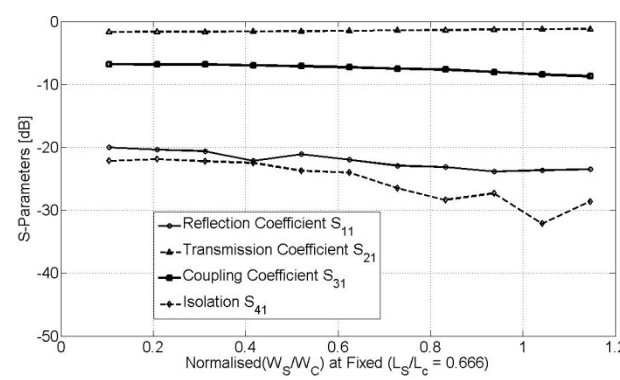

Fig. 13. The S-parameters of the coupler (Fig. 10), against normalized slot width (W_S / W_C) at fixed ratio of slot length ($L_S / L_C = 2/3$).

IV. FABRICATIONS AND MEASUREMENTS

A. Rectangular slot loop example

Following the design considerations in Section II and simulation results, summarized in several useful design curves, the microstrip coupler shown in Fig. 10 was fabricated, using thin film technology and photolithographic techniques. The substrate used is Rogers RT/Duroid 5880 ($\varepsilon_r = 2.2$, h = 1.5748 mm). The photo of the realized coupler (coupler-1) with DGS is shown in Fig. 14. The simulated and measured S-parameters of this coupler are presented in Fig. 15.

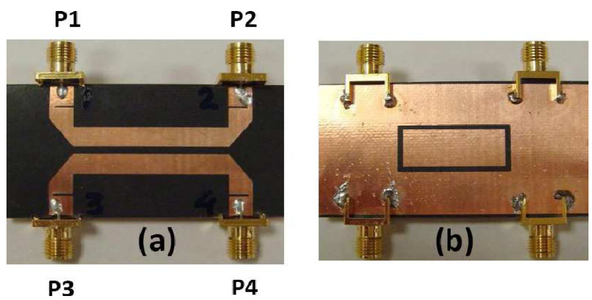

Fig. 14. Photo of the measured example coupler-1. (a) The top layer. (b) The bottom DGS layer.

The simulated and measured S-parameters are in a good agreement. The measured S_{31} is smoother than the simulated response above 3 GHz, which may be due to parasitic radiation effects from the DGS, not taken into account by the simulation tools for the surroundings of the coupler. In addition, there are tolerances between the box shield used in the simulation tools and the microstrip test fixture used in measurements.

The measured S_{11} and S_{41} are all below 20 dB in the coupling bandwidth, and better than the simulated counterparts at certain frequencies. However, the ripple of S_{11} seems stronger than the simulated response.

B. Meandered slot loop example

Meandering the DGS slot loop actually adds more bends in the structure and hence its size can be reduced while maintaining the same total length and area.

More bends, on the other hand, are expected to increase the parasitic capacitances. Reducing the DGS size would allow applying more DGS cells in the available ground area.

Several publications [7, 9, 11] have shown that multiple cells (or periodic DGS structure) are another way to improve the coupling performance. Thus, testing a single cell of such a meandered slot loop is useful to explore such effects on the coupling coefficient S_{31} and its fractional bandwidth (B%), while maintaining acceptable levels of S_{11} and S_{41}. Meandering can, also, be made multiple on all sides of the slot structure if needed.

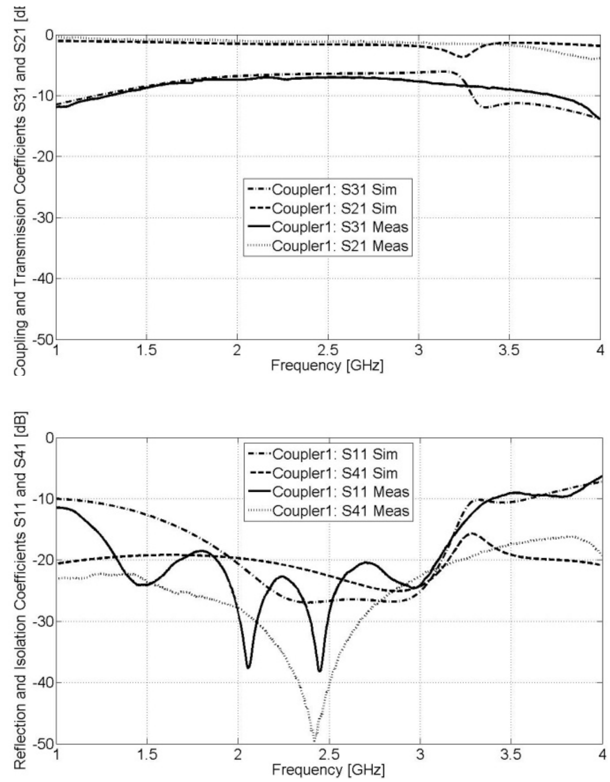

Fig. 15. Simulated and measured S-parameters of DGS coupler (coupler-1).

Two microstrip directional couplers with different meandered slot dimensions were fabricated according to the geometries shown in Fig. 16. The top layer of the initial coupler geometry (Fig. 16 (a)) is used for the two different DGS structures (Fig. 16 (b) and (c)).

Photos of the two fabricated couplers are shown in Fig. 17. For convenience, the top and bottom layers of Fig. 16 (a) and (b) are assigned as coupler-2, while Fig. 16 (a) and (c) as coupler-3. For coupler-2, the simulated and measured frequency responses of S-parameters are compared in Fig. 18, where a good agreement was observed.

The coupler achieves 2.5 GHz bandwidth with a coupling coefficient (S_{31} = -7 ± 1dB). This would correspond to a fractional bandwidth of 125% at a center frequency of 2 GHz. However, if we consider the associated reflection and isolation coefficients S_{11} and S_{41} with acceptable values below -15 dB and -20 dB, respectively, the useful bandwidth would be reduced to around 95%.

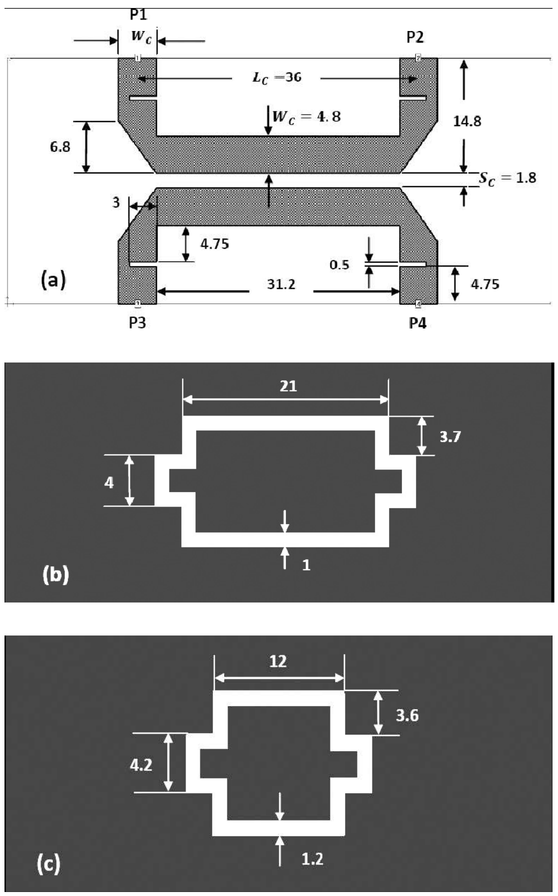

Fig. 16. Geometric dimension of the fabricated meandered DGS couplers 2 and 3. (a) The top layer geometry used for both couplers. (b) DGS geometry of coupler 2. (c) DGS geometry of coupler 3. All dimensions are in mm.

For coupler-3 with smaller DGS meandered slot dimensions, the simulated and measured S-parameters are compared in Fig. 19. Good agreement was observed, but the coupling coefficient for this coupler is slightly weaker (S_{31} = -10 ± 1dB) than in coupler-2. The sharp drop (observed in coupler-2) in the coupling level beyond 4 GHz is not observed for coupler-3.

The measured S_{11} is still below -15 dB in the entire lower frequency region up to 3 GHz, beyond which, a sharp rise is seen. On the other hand, the measured S_{41} is below 25 dB in most of the frequency region, which is better than S_{41} in coupler-2.

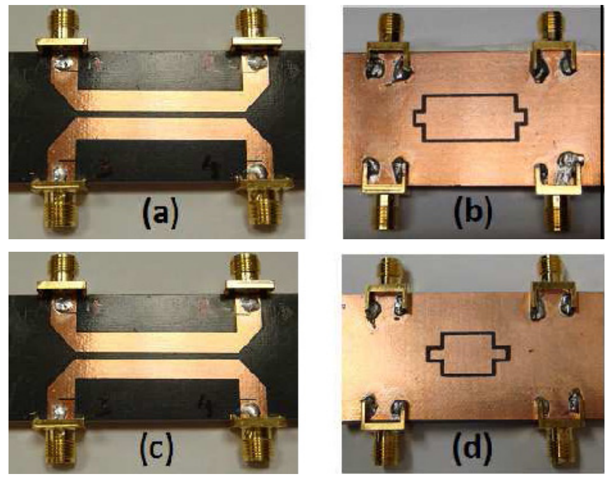

Fig. 17. Photos of the realized and measured couplers, (a) & (b) for coupler-2 while (c) & (d) for coupler-3.

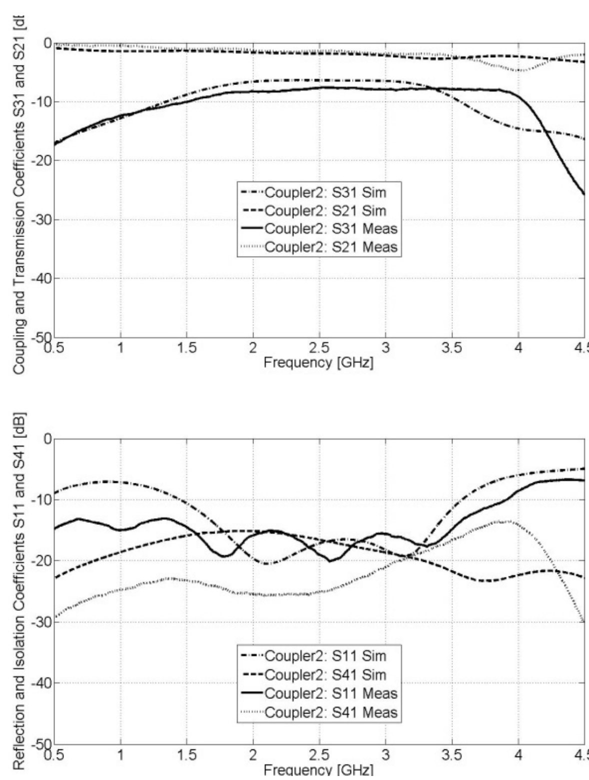

Fig. 18. Measured and simulated S-parameters of the DGS coupler-2.

It can be seen that meandering the DGS slot loop does not show significant effect on the overall performance of the desired parameters, although it affects the reflection and isolation positively and slightly decreases the coupling level.

In general, the measurements confirm the approach undertaken to identify trade-offs in selecting the design geometry, so to achieve the desired coupler response, in terms of the coupling bandwidth, flatness and reasonable levels of reflection and isolation coefficients.

The achieved results for the investigated structures and design curves can be applied to other frequencies of interest, if scaling theory is properly applied to all geometrical and substrate parameters.

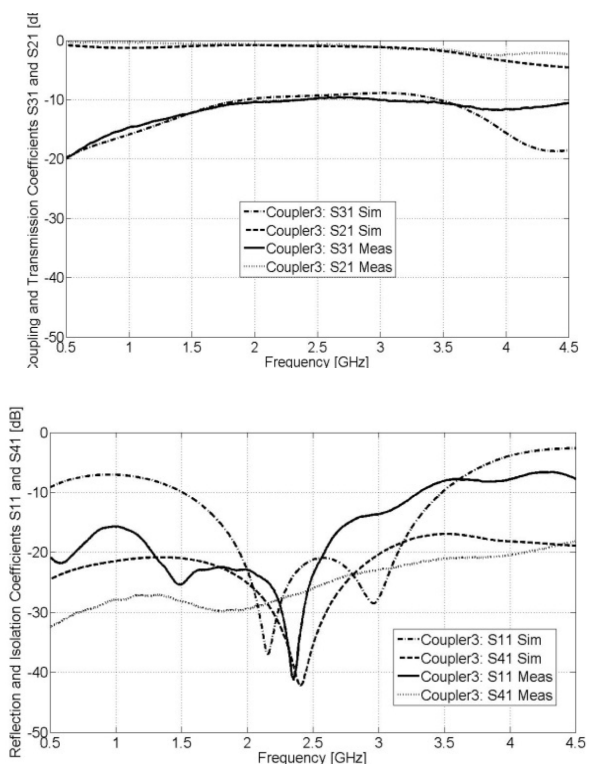

Fig. 19. Simulated and measured S-parameters of the DGS coupler-3.

V. CONCLUSION

Various microstrip directional couplers, composed of DGS shapes, ranging from slot area to slot loop, were studied. Three different samples of DGS couplers were fabricated and measured. The measured responses were in good agreement with the specified parameters and the full-wave simulations. The results showed that the coupling level can be raised from -20 dB to around -8 dB over a relatively wide bandwidth of 3 GHz, which corresponds to more than 95% fractional bandwidth (± 1 dB ripple) and acceptable levels of reflection and isolation below -15 dB and -20 dB, respectively).

Such results are not achievable with a conventional microstrip directional coupler, having a reasonable spacing between the coupled lines, crucial for fabrication lithography techniques. Various effects of the DGS on the coupler performance were investigated and many useful design curves were extracted. The study showed that the coupling bandwidth can be increased significantly, but this is limited by a deterioration of the reflection and isolation coefficients. A well-matched microstrip coupler exhibited a large mismatch when the DGS is present. A method is applied to restore the matching to acceptable levels, but with some reduction in the bandwidth. The unit cell DGS structure may be applied in other shapes or multiples of such a cell for further improvement of the coupling. If the initial coupler is designed with -15 or -10 dB coupling, the described DGS is expected to raise the coupling to much tighter levels.

ACKNOWLEDGMENT

The authors would like to acknowledge the assistance in fabrication and measurement provided by PSATRI (Prince Sultan for Advanced Technology Research Institute), King Saud University, Saudi Arabia.

REFERENCES

[1] Technology report, "Couplers remain important products, using new manufacturing techniques," High Frequency Electronics, Summit Technical Media, LLC, pp. 42−44, January, 2003.

[2] D. Ahn, J. S. Park, C. S. Kim, J. Kim, Y. Qian, and T. Itoh, "A design of the lowpass filter using the novel microstrip defected ground structure," *IEEE Trans. on Microwave Theory and Techniques*, vol. 49, no. 1, pp. 86−93, 2001.

[3] A. B. A. Rahman, A. K. Verma, A. Boutejdar, and A. S. Omar, "Control of bandstop

response of Hi-Lo microstrip low-pass filter using slot in ground plane," *IEEE Trans. on. Microwave. Theory Tech.*, vol. 52, no. 3, pp. 1008−1013, 2004.

[4] J. -X. Chen, J. -L. Li, K. -C. Wan, and Q. Xue, "Compact quasi-elliptic function filter based on defected ground structure," *IEE Proc.-Microwave Antennas propagation*, vol. 153, no. 4, pp. 320− 324, 2006.

[5] P. Vagner and M. Kasal, "Design of novel microstrip low-pass filter usingdefected ground structures," *Microwave and Optical Technology Letter*s, vol. 50, no. 1, pp. 10 − 13, 2007.

[6] A. S. Mohra, "Compact lowpass filter with sharp transition band based on defected ground structures," *Progress In Electromagnetics Research Letters*, vol. 8, pp. 83 − 92, 2009.

[7] S. N. Burokur and M. Latrach, "A novel type of microstrip coupler utilizing a slot split-ring resonators defected ground plane," *Microwave Opt. Technol. Lett.*, vol. 48, no. 1, pp. 138−141, 2006.

[8] K. Y. Liu, C. Li, and F. Li, "A new type of microstrip coupler with complementary split-ring resonator (CSRR)," *PIERS Online*, vol. 3, no. 5, pp. 603-606, 2007.

[9] R.-X. Wu, X.-Y. Ji, R.-F. Chen, and Y. Poo, "A Novel microstrip coupler with EBG structures," *Asia-Pacific Microwave Conference*, *APMC08*, Macau, pp. 1 − 4, 2008.

[10] R. Sharma, T. Chakravarty, and S. Bhooshan, "Design of a novel 3db microstrip backward wave coupler using defected ground structure," *Progress In Electromagnetics Research,* vol. 65, pp. 261− 273, 2006.

[11] J.-S. Hong and B. M. Karyamapudi, "A General circuit model for defected ground structures in planar transmission lines," *IEEE microwave and wireless components letters*, vol. 15, no. 10, pp. 706 − 708, 2005.

[12] S. Lee and Y. Lee, "A design method for microstrip directional couplers loaded with shunt inductors for directivity enhancement," *IEEE Trans. Microw. Theory Tech.*, vol. 58, no. 4, pp. 994− 1002, 2010.

[13] S. Gruszczynski and K. Wincza, "Broadband multisection asymmetric 8.34-dB directional coupler with improved directivity," *Proceedings of Asia-Pacific Microwave Conference*, 2007.

[14] K. Dong-Joo, J. Yongwoo, K. Jung-Hoon, K. Jong-Hwa, K. Chul-Soo, L. Jong-Sik, and A. Dal, "A novel design of high directivity CPW directional coupler design by using DGS," *IEEE, MTT-S Int. Microw. Symp. Dig.*, pp. 1239 − 1243, Long Beach, Ca, USA, 1995.

[15] C. Kuo-Sheng, M. Ming-Chuan, C. Yi-Ping, and C. Yi-Chyun, "Closed-form equations of conventional microstrip couplers applied to design couplers and filters constructed with floating-plate overlay," *IEEE Trans. Microw. Theory Tech.*, vol. 56, no. 5, pp. 1172 − 1179, 2008.

[16] A. M. Abbosh, "Broadband parallel-coupled quadrature coupler with floating-potential ground plane conductor," *Microwave and Optical Technology Letters*, vol. 50, no. 9, pp. 2304 −2307, 2008.

[17] Sonnet suit EM field solver software, Version: 12.56, North Syracuse, NY, www.sonnetsoftware.com.

[18] IE3D EM Simulation and Optimization Package, Version 11.5, CA 94538, U.S.A, www.zeland.com.

[19] UCLA research program in electrical engineering, "Application of defected ground structure in Microstrip line forward coupler," http://www.mwlab.ee.ucla.edu/, 2003.

[20] D. M. Pozar, *Microwave Engineering*, 3rd Ed., Wiley-Interscience, New York, 2005.

[21] T. C. Edwards, *Foundations for Microstrip Circuit Design*, Wiley-Interscience, Chichester, 1981.

[22] A. Eroglu and J. Kyoon Lee, "The complete design of microstrip directional couplers using the synthesis technique," *IEEE Transactions on Instrumentation and Measurement,* vol. 57, no. 12, pp. 2756 − 2761, 2008.

Ayman S. Al-Zayed Received the B.Eng. (Honours) degree in Communication and Electronic Engineering from the University of Northumbria at Newcastle in 1995. In 2000, he obtained the M.S. degree in Electrical Engineering from the University of Hawaii at Manoa. In 2004, he earned the Ph.D.

degree in Electrical Engineering from North Carolina State University. In February, 2004, he joined the Department of Electrical Engineering at Kuwait University where he is currently an Assistant Professor. His research interests include microwave and millimeter-wave active and passive devices, power combining, quasi-optical devices, antennas, phased arrays and radars.

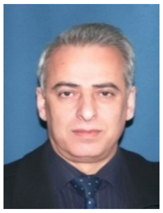

Zuhair M. Hejazi He is an Associate Professor of Telecommunication Engineering. He received the Diploma Degree in Radio Engineering- Radar & Radio Navigation from the Technical University of Sofia in 1981. The M.Phil. and Ph.D. degrees, from Bradford University- UK, in 1995 and 1998, respectively. From 1985 to 1988, he was working in the Quality Control of Digital Radio Link Systems and CAD of Microwave Components for Siemens and two other Companies in Münich, Germany. From 1990 to 1993, he was working as a Research and Teaching Assistant in the Hijjawi Faculty for Engineering Technology, Yarmouk University, Jordan, where he served later as a Faculty Member, Assistant Dean and Chair of the Telecommunications Engineering Department. Recently, he served in Middle East College of Information Technology (MECIT), Muscat-Oman for two years as a faculty and HoD of the Electronics and Telecommunication Department. Currently, he is a faculty with the EE Department, College of Engineering, King Saud University, Riyadh, KSA. His research interests are mainly in microwave devices, planar filters, couplers, and antennas.

Ashraf Shouki Mohra Was born in Cairo, Egypt. Each of M.S. and Ph.D. degree were received in Electronics and Communications from Ain Shams University in 1994 and 2000, respectively. He worked in the Electronics Research Institute, Ministry of scientific research and technology, Cairo, Egypt. He has worked on the analysis and design of microstrip circuits, such as couplers, filters, six-port reflectometers, defected ground structures, metamaterials, etc. He was promoted to associate professor at Electronics Research Institute on March 2006. Now, he is with EE Dept, College of Engineering, King Saud University. His current fields of interests are concerned with the computer aided design of microwave and millimeter-wave wide-band planar circuits and microstrip antennas using photolithographic technique and thin film technology.

Modeling and Simulation of Wilkinson Power Splitter in Suspended Stripline

Sandi Ibrahimpasic [1] and Moamer Hasanovic [2]

[1] Department of Electrical Engineering
University of Sarajevo, Zmaja od Bosne bb, 71000 Sarajevo, Bosnia-Herzegovina
ibrahimpasic.sandi@gmail.com

[2] Faculty of Engineering and Natural Sciences (FENS)
International University of Sarajevo, Hrasnicka Cesta 15, 71000 Sarajevo, Bosnia-Herzegovina
mhasanovic@ius.edu.ba

Abstract **─** This paper offers one possible solution to the problem of different phase velocities in even and odd mode during the design of Wilkinson power splitters. This topic is especially important in the design of modern beamforming networks for military and space applications where low insertion loss is required and obtained through a use of suspended stripline and other extremely (ultra) inhomogeneous platforms. A new approach is proposed where even and odd mode quarter-wave transforming sections of a multi-section Wilkinson splitter do not end at the same locations. The approach has been implemented through an algorithm that calculates all critical parameters of the splitter. In order to confirm the practicality of the proposed solution, various examples of Wilkinson splitters have then been developed through the algorithm and then simulated using SONNET® and other electromagnetic software tools. The developed configurations have, also, been compared to the conventional ones to evaluate the improved performance.

Index Terms **─** Beamforming network, Chebyshev polynomials, even-odd mode, phase velocities, SONNET®, suspended stripline Wilkinson power splitter.

I. INTRODUCTION

Modern radar and satellite systems often require a low insertion loss performance of their integral parts to accommodate for a stringent loss budget and long communication paths. This restriction is imposed on the corresponding beamforming networks, as well. In order to meet this design requirement, the beamformers are very often realized in suspended airline technology (Figure 1) that provides for a low effective dielectric constant and consequently low insertion loss.

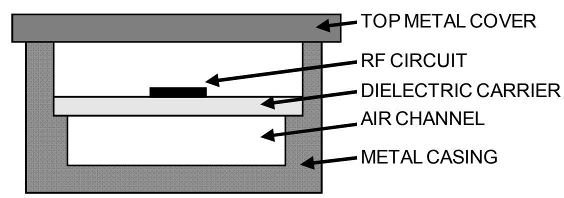

Fig. 1. Cross-section (stack-up) of an RF component realized in suspended airline technology.

II. DESIGN PROBLEM

An important phase in the development of such a beamformer is the design of a corresponding Wilkinson power splitter [1]. Wilkinson power splitters have been treated by many authors and through many different configurations. An overview of these configurations can be found in [2]. Demir et al. for example recently proposed a model of efficient wideband power divider for planar antenna arrays that used Klopfenstein impedance taper for a significant reduction of the physical dimensions of the component [3]. This work as well as many others in the past didn't take into consideration output parameters of the splitter such as output return loss and isolation between the two output ports. Certain applications such as antenna arrays require good isolation between the two output ports of the splitter in order to avoid undesired coupling between the elements of an antenna array. In order to meet this design requirement, odd mode must, also, be considered and resistors must be incorporated into the design of the power splitter. In that case, isolation and output return loss of the power divider is calculated as follows

$$\text{Isolation} = -20\log\left|\Gamma_e - \Gamma_o\right| \quad [\text{dB}] \qquad (1)$$

$$Out\ \text{Re}t\ Loss = -20\log\left|\Gamma_e + \Gamma_o\right| \quad [dB], \qquad (2)$$

where Γ_e and Γ_o represent reflection coefficients in even and odd mode, respectively.

If the splitter consists of coupled quarter-wave impedance transforming sections, then the characteristic impedances of these coupled sections in odd mode would determine the values of the resistors that are to be used in the power splitter design [4]. In addition to that, if the splitter is designed in an inhomogeneous environment such as a suspended stripline then these sections would have different electrical lengths in even and odd modes due to different phase velocities of the two modes. This effect is further strengthened at the chip resistor locations due to a high dielectric constant of the material the chips are built from (usually alumina, BeO, etc).

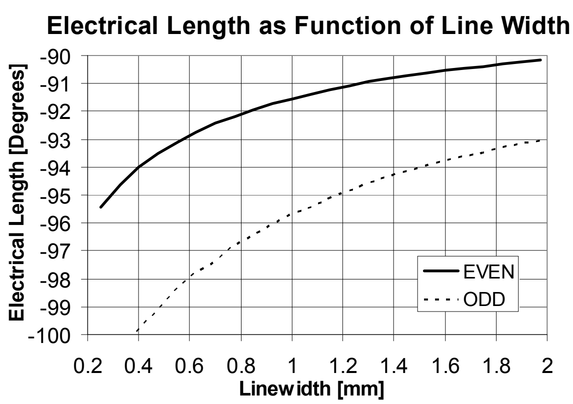

Fig. 2. Electrical lengths of coupling sections in even and odd modes as a function of transmission line width (physical length of the section=7.5mm, coupling gap=0.625mm).

Therefore, if physical lengths of quarter-wave impedance transforming sections are tuned to be equal to quarter-wave lengths in even mode, the same physical lengths would not represent 90^o sections in odd mode. They would most probably be longer than 90^o due to a higher dielectric constant of odd mode. Figure 2 shows electrical lengths of coupling sections of the same physical length (7.5mm) in even and odd modes as a function of transmission line width for a suspended stripline stackup that consists of 0.125mm thick Taconic TLE-95 substrate as a dielectric carrier and two 0.625mm deep air channels on the top and bottom of the carrier (see Figure 1). Significant difference in the length in the two modes is observed (5-8^o).

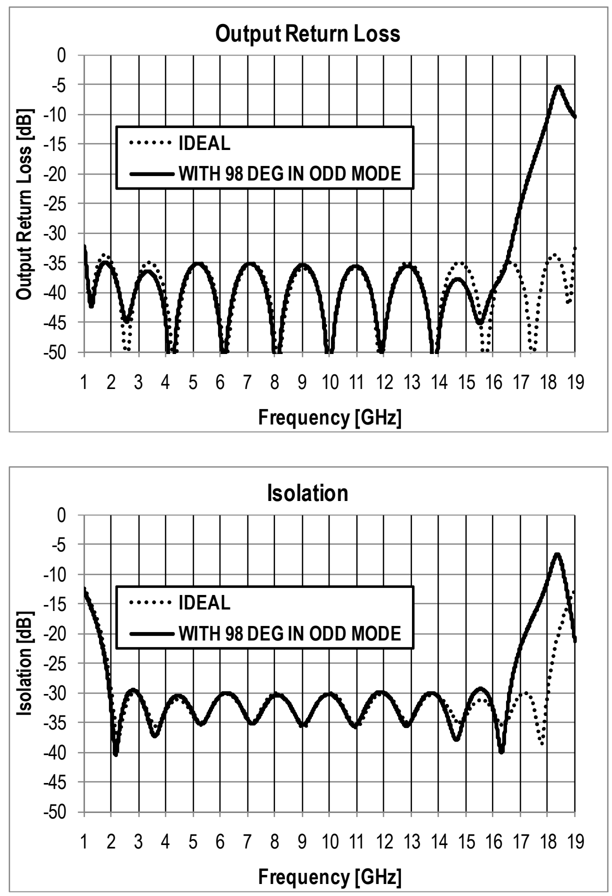

Fig. 3. Performance comparison of the ideal power splitter and splitter with 98^o long transforming sections in odd mode (for a 10-section Wilkinson splitter centered at 10GHz realized in suspended stripline - 0.125mm Taconic TLE-95 dielectric carrier and two 0.625mm deep air channels): analysis done in Ansoft Designer®.

Different electrical lengths of the transforming sections of the power divider affect the performance of the power divider. Figure 3 compares performance of the 10-section power divider in an ideal case (electrical lengths of even and odd mode equal) and a power divider in which transforming sections are 8^{o} longer in odd mode compared to even mode. As a result, a significant deterioration of the output return loss and isolation performance at the higher end of the frequency band may be noticed.

The problem of different lengths for even and odd modes has been treated by many authors in the past. March [5] used lumped elements to achieve phase velocity compensation in the two modes while Podell [6] proposed use of teeth-like or sawcut-like shapes in the "wiggly" coupler for the same purpose. The use of anisotropic substrates [7] or dielectric overlays [8] has also been suggested as a solution to the problem described above. All these solutions are related to specific application and would not be suitable to the case of Wilkinson power splitter in suspended stripline, either because the solution would be too bulky or would not be compatible with the suspended stripline as a choice for the material platform in this particular application.

III. PROPOSED SOLUTION

As a result of this research, an elegant approach has been offered to the problem described above. The main idea used in the proposed solution is to have the quarter-wave transforming sections not necessarily being separated by the shunt resistive elements, as is the case in the conventional Wilkinson power splitter [1], but rather pulled toward the T-junction (Figure 4a).

In even mode (Figure 4b), this technique would still result in a traditional multi-section quarter-wave transforming network optimized through the use of Chebyshev polynomials. In odd mode (Figure 4c), however, each transmission line section between the two consecutive shunt resistors will consist of two elements with different characteristic impedances, but their electrical lengths would add up to a total of 90^{o}.

The values of the shunt resistors then need to be optimized in order to satisfy matching conditions in a newly arisen odd-mode transforming network [9]. This optimization is realized through an algorithm developed for this purpose and tested through multiple examples.

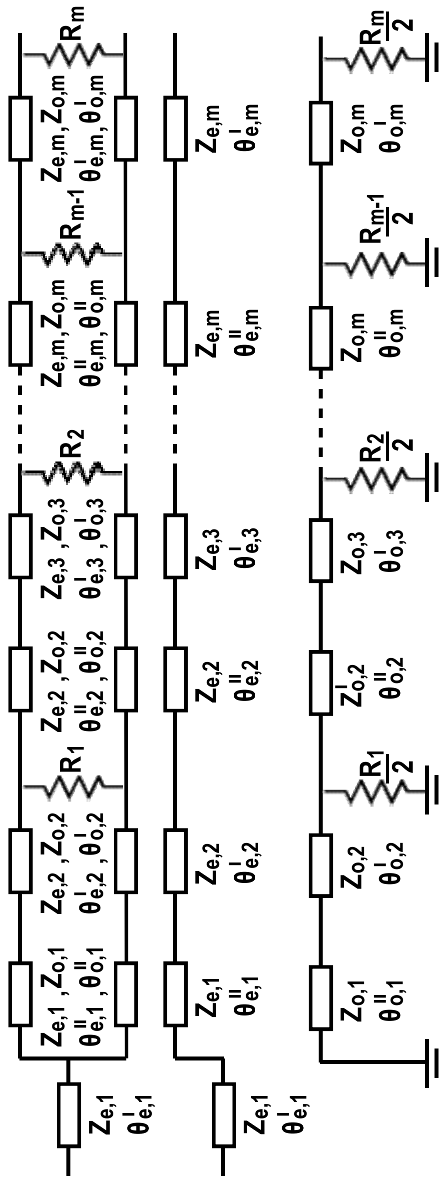

(a) (b) (c)

Fig. 4. (a) The transmission line model of the proposed power splitter, (b) even mode, (c) odd mode.

The desirable performance of the Wilkinson splitter is achieved if reflection coefficients in even and odd mode, Γ_e and Γ_o, have the same zeros. The reflection coefficient in odd mode can be written as a quotient of two polynomials

$$\Gamma_o = -\frac{w^m + c_{m-1} w^{m-1} + \ldots + c_o}{w^m + d_{m-1} w^{m-1} + \ldots + d_o}, \tag{3}$$

where c_i and d_i are determined by the parameters $Z_{o,i}$ and R_i of the odd mode network shown in Figure 4(c). Equation (3) is derived by considering this odd mode network as a cascaded network of *m* two-port elements with the first element being shorted.

Similarly, the reflection coefficient of the even mode network is represented by

$$\Gamma_e = \frac{w^m + a_{m-1} w^{m-1} + \ldots + a_o}{w^m + b_{m-1} w^{m-1} + \ldots + b_o}, \tag{4}$$

where a_i and b_i are determined by the parameters $Z_{e,i}$ of the even mode network shown in Figure 4(b). Values of $Z_{e,i}$ are optimized through the use of Chebyshev polynomials and $Z_{o,i}$ are so determined to satisfy requirements for the desired physical gap between the two branches of the splitter. At last, forcing Γ_o in (3) to have the same zeros as Γ_e in (4) results in a system of *m* equations from which *m* resistances R_i are found.

The values of resistances R_i depend on the coupling between the coupled transforming sections. This coupling tends to increase the values of the resistances towards the outputs of the splitter. If the splitter contains more than five sections and more than five resistances, it is found that some of the resistor values closer to the outputs become so large (several times the characteristic impedance) that they can be entirely removed from the splitter without changing its performance. This has been done with the last resistor of the splitter in Figure 5. This provides an advantage because it reduces the cost associated with the chip resistors and reduces the overall length of the splitter.

Based on the optimized values of the shunt resistors, and previously determined values of characteristic impedances and electrical lengths of transforming sections, various Wilkinson power splitter geometries have been modeled and simulated. Excellent results have been achieved that confirm the novelty and success of the proposed technique.

Figure 5, for example, shows a design of a 10-section, 10-chip equal-split Wilkinson power splitter developed using the proposed technique. As observed in the geometry shown in Figure 5, there is a clear indication of the impedance transformation location shift due to the previously described reasons.

For this design, we have used a 0.125mm thick Taconic TLE-95 substrate as a dielectric carrier, with 0.625mm deep air channels on the top and bottom of the carrier (see Figure 1). Each transforming section has been individually simulated in SONNET® to arrive at the proper values of corresponding even and odd mode impedances as well as physical lengths of quarter-wave impedance transforming sections in even and odd mode.

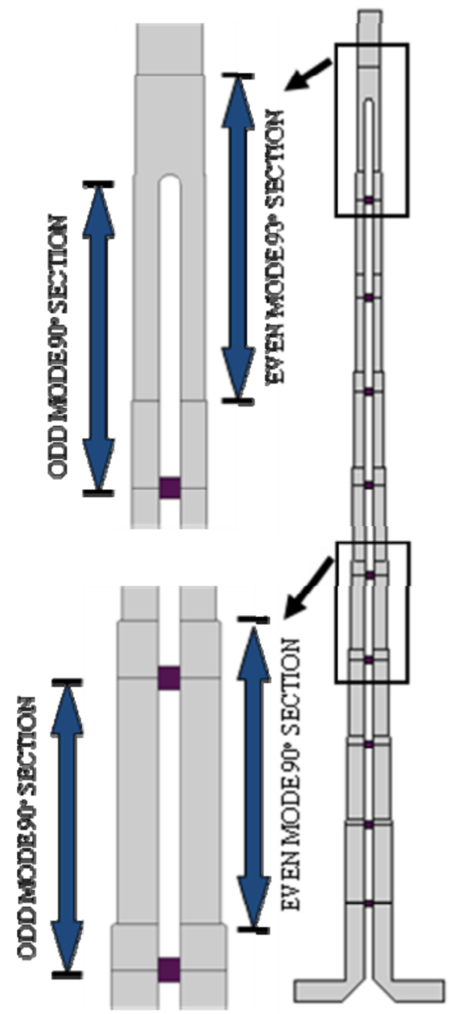

Fig. 5. Geometry of 10-section 10-chip Wilkinson power splitter with tuned quarter-wave transformer lengths.

Figure 6 presents a corresponding SONNET® model of the entire structure. The splitter has been simulated in different ways in SONNET®. It has been broken up into sub-models that have been analyzed with the use of co-calibrated ports.

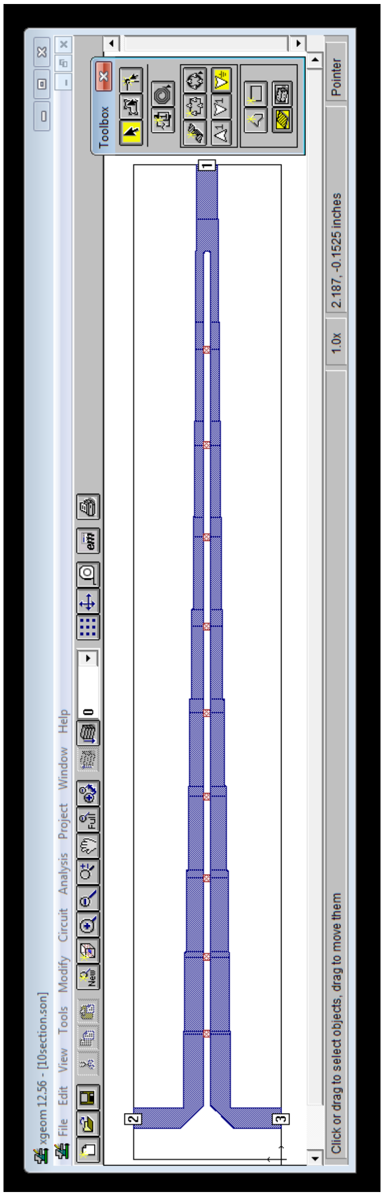

Fig. 6. SONNET® model of the 10-section 10-chip Wilkinson power splitter with tuned quarter-wave transformer lengths shown in Figure 3.

The splitter has then been simulated in its entirety. No significant difference has been observed in the performance of the full model relative to the performance of the combined sub-models. Simulating the splitter through multiple sub-models, however, significantly reduces the computational memory and time.

The simulated performance of this power splitter is shown in Figure 6. Slight asymmetries that can be seen on the performance curves are the result of the effects that are not accounted for in the optimization algorithm (finite size of the resistive elements, minor discontinuities at the impedance transformation locations, etc).

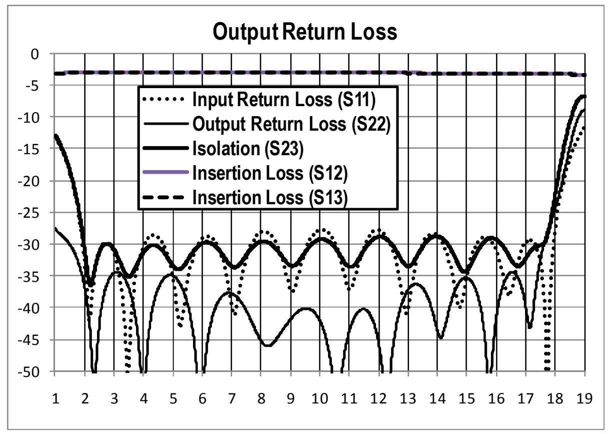

Fig. 7. Simulated performance of the 10-section 10-chip Wilkinson splitter with tuned quarter-wave transformer lengths shown in Figure 5.

IV. CONCLUSION

The proposed algorithm represents an elegant design solution to the problem of different phase velocities in even and odd mode during the Wilkinson splitter design in inhomogeneous stack-ups. It has been tested and confirmed on multiple practical examples. The authors hope that this idea will find successful application by RF engineers who design low loss beamforming networks and other systems on inhomogeneous platforms.

REFERENCES

[1] E. J. Wilkinson, "An n-way hybrid power divider," *IEEE Trans. Microwave Theory and Techniques*, vol. 8, pp. 116–118, Jan. 1960.

[2] M. D. Abouzahra and K. C. Gupta, *Hybrids and power dividers/combiners, Analysis and Design of Planar Microwave Components*, IEEE Press, New York, 1994.

[3] V. Demir, D. A. Elsherbeni, D. Kajfez, and A. Z. Elsherbeni, "Efficient Wideband Power Divider for Planar Antenna Arrays," ACES

Journal, vol. 21, no. 3, pp. 318–324, Nov. 2006.

[4] H. Y. Yee, F. C. Chang, and N. F. Audeh, “N-way TEM-mode broadband power dividers,” *IEEE Trans. Microwave Theory and Techniques*, vol. 18, pp. 682–688, Oct. 1970.

[5] S. L. March, “Phase Velocity Compensation in Parallel-Coupled Microstrip,” 1982 MTT Symposium Digest, pp. 410-412, June 1982.

[6] A. Podell, “A High Directivity Microstrip Coupler Technique,” 1970 MTT Symposium Digest, pp. 33-36, May 1970.

[7] N. G. Alexopoulos and C. M. Krowne, “Characteristics of Single and Coupled Microstrips on Anisotropic Substrates,” *IEEE Trans. Microwave Theory and Techniques*, vol. 26, pp. 387–393, June 1978.

[8] D. D. Paolino, “MIC Overlay Coupler Design Using Spectral Domain Techniques,” *IEEE Trans. Microwave Theory and Techniques*, vol. 26, pp. 646–649, Sep. 1978.

[9] R. B. Ekinge, “A new method of synhesizing matched broadband TEM-mode three-ports,” *IEEE Trans. Microwave Theory and Techniques*, vol. 19, pp. 81–88, Jan. 1971.

Sandi Ibahimpasic received his B.S. from University of Sarajevo in June of 2010. His research interest is in the field of wireless communications, multimedia, and digital signal processing. He took part in a couple of projects in the area of VoIP system development, WiMAX case study, and process simulation in telecommunication channels.

Moamer Hasanovic received his B.S. from University of Sarajevo in 1997 and M.S. and Ph.D. degrees in electrical engineering from Syracuse University, New York, in 2002 and 2006, respectively. He worked as an Electrical Engineer for BH Telecom Sarajevo and as a RF Design Engineer at Anaren Microwave in East Syracuse, New York. In 2010, he joined International University of Sarajevo, Bosnia-Herzegovina, where he is currently a Professor in the Department of Electrical and Electronics Engineering. His research interests are in the area of microwave devices and computational electromagnetics. He is a member of the Applied Computational Electromagnetic Society (ACES).

Microwave Detection of Cracks in Buried Pipes using the Complex Frequency Technique

Fadi Deek and Magda El-Shenawee

Department of Electrical Engineering
University of Arkansas, Fayetteville, AR 72701, USA
eldeek_fadi@yahoo.com, magda@uark.edu

***Abstract*─** This work outlines a new technique for detecting cracks in buried pipes using scattered fields. The matrix pencil method (MPM) is applied on synthetic data to extract the natural frequency poles. A 50 cm long hollow pipe, 2.5 cm in diameter, and 5 mm in thickness is considered. Cracks of arc lengths of 6 cm and 4 cm with a width of 0.5 mm are introduced into the metallic pipes. It is shown that the MPM has the capability to extract distinctive poles associated with these cracks even when the pipe is hidden behind plywood, buried in sand, or when the synthetic data is corrupted with random noise of 10 dB signal to noise ratio.

***Index Terms*─** Complex frequency, crack, GPR, detect, matrix pencil method.

I. INTRODUCTION

Under the effect of pressure, humidity, and other natural or unnatural causes, cracks develop in pipes. The results of such leaks are hazardous to the environment and cause economical losses. Several crack detection techniques have been developed and each serves a specific application [1-5]. Some techniques use trained dogs that can sniff odors of leaking material even from underground [1]. Hardware based techniques include closed-circuit television techniques [2] where a camera is used to record images from the pipes' walls.

In general, non destructive evaluation techniques, NDE, are preferred since they require no excavation. Common NDE techniques use radiography [3] to assess the condition of pipes. An X-ray tube is used to photograph pipes hidden behind walls. The instruments for this method are bulky and hazardous. Also, ultrasonic waves are used to detect cracks on the surfaces of pipes that are partially inaccessible [4]. Such techniques are still inaccurate when detecting corrosion and wall thinning from the inside of the pipe.

Of the many techniques, ground penetrating radars, GPRs, have shown the most flexibility and portability. Ground penetrating radars use electromagnetic waves in order to remotely characterize the physical properties of a media. By doing so, buried targets can be located. For example, Gamba et al. [5] use neural networks to detect hyperbolic signatures of pipes underground. In addition, the media surrounding the defected pipe can be evaluated. As mentioned in [1], the GPR profile is altered whenever a liquid, such as water, leaks into the surrounding.

The method of moments commercial solver was available at our labs, FEKO [6], and was used in this work to simulate cases where a pipe was immersed in free space, hidden behind plywood, or buried underneath sand. The scattered field was solved in the frequency range 50MHz – 10 GHz in steps of 12.5MHz. The present work is not limited to frequency domain solvers, but other time domain software could have been used.

Many available techniques to extract the poles of the complex frequencies such as ESPRIT, Prony and several other singular value decomposition based methods can be found in [7]. Of the many methods, the matrix pencil method (MPM) has shown effectiveness and simplicity [8]. The total least square matrix pencil method (TLSMPM) is the version used in this work. The TLSMPM has shown better performance than other MPM variations when operated under noisy data [9].

A MATLAB algorithm extracts the complex frequencies from the scattered far fields. These frequencies are associated with the cracks on the pipes. This method was inspired by the work in [10] where Blischak et al. used elliptical antennas with different sized notches to generate unique radio frequency identifications (RFIDs). Each RFID is composed of a set of complex frequencies. The method used for extracting the complex frequencies is known as the matrix pencil method (MPM) [7].

II. MATRIX PENCIL METHOD

The time domain transient response of a scattering object can be expressed by a sum of exponentially decaying signals [8]

$$x(kT_s) = \sum_{i=1}^{M} R_i z_i^k \qquad \text{for } k = 0,1,\ldots\ldots N\text{-}1 \;, \tag{1}$$

where x(t) is a vector of size N containing the discrete time points, T_s is the sampling period, $R = A_i e^{-j\varphi_i}$ are the complex residues of the matrix pencil poles composed of the amplitudes A_i's and the phase delays Φ_i's. The poles

$$z_i = e^{s_i T_s} = e^{(-\alpha_i + j\omega_i)T_s} \tag{2}$$

are composed of damping factors α_i and radial frequencies ω_i. The number of poles to be extracted is defined by the parameter M. The first step in extracting the poles is to build the Hankel matrix X_H as [9]:

$$X_H = \begin{vmatrix} x_1 & x_2 & \cdots & x_{L+1} \\ x_2 & x_3 & \cdots & x_{L+2} \\ \vdots & \vdots & \ddots & \vdots \\ x_{N-L} & x_{N-L+1} & \cdots & x_N \end{vmatrix}_{(N-L)x(L+1)} \;, \tag{3}$$

where L is known as the pencil parameter.

The singular value decomposition (SVD) is performed on the matrix as in (4) in order to obtain the eigenvectors and eigenvalues as [9]:

$$U\Sigma V^H = SVD(X_H) \;. \tag{4}$$

The matrices U and V are the left and right unitary matrices, respectively. The matrix U is composed of the eigenvectors of the matrix $X_H X_H^H$ where the *superscript H* denotes the conjugate transpose; whereas, V is composed of the eigenvectors of the matrix $X_H^H X_H$. The diagonal matrix $\sum$ contains the singular values of X_H as in (5) [9]:

$$\Sigma = \begin{vmatrix} \sigma_1 & 0 & \cdots & 0 & 0 \\ 0 & \sigma_2 & \cdots & 0 & 0 \\ \vdots & \vdots & \ddots & \vdots & 0 \\ 0 & 0 & \cdots & \sigma_{N-L} & 0 \end{vmatrix}_{(N-L)xL} \;. \tag{5}$$

Only the first M eigenvectors of either U or V are kept. Considering U, as an example, (6) shows the truncated matrix.

$$U = [\hat{u}_1, \hat{u}_2, \ldots, \hat{u}_M]^T. \tag{6}$$

The complex-frequency poles are the eigenvalues of (7) [9]:

$$[z][I] = \left[U_1^+\right]\left[U_2\right]_{MxM} \;, \tag{7}$$

where z is a vector containing the complex poles and I is the identity matrix, + denotes the Moore-Penrose pseudo inverse $X^+ = [X^H X]^{-1} X^H$ and

$$U_1 = [\hat{u}_1, \hat{u}_2, \ldots, \hat{u}_{M-1}]^T \tag{8}$$

$$U_2 = [\hat{u}_2, \hat{u}_2, \ldots, \hat{u}_M]^T \;. \tag{9}$$

Once the poles are calculated, the residues, R_i, in (10) can be found by solving the least square problem:

$$\begin{vmatrix} x_1 \\ x_2 \\ \vdots \\ x_M \end{vmatrix} = \begin{vmatrix} 1 & 1 & \cdots & 1 \\ z_1 & z_2 & \cdots & z_M \\ \vdots & \vdots & \ddots & \vdots \\ z_1^{N-1} & z_2^{N-1} & \cdots & z_M^{N-1} \end{vmatrix} \begin{vmatrix} R_1 \\ R_2 \\ \vdots \\ R_M \end{vmatrix} . \tag{10}$$

The resulting poles are ordered with respect to the singular value matrix in (5). Thus, σ_1 is the maximum entry and σ_{N-L} is the minimal entry of matrix $\sum$. This, also, means that z_1 corresponds to σ_1 and so on.

There are rules of thumb in the literature to what the best values of the pencil parameter L and the numbers of poles M are [9]. It is recommended that the pencil parameter L have values between $N/3 \leq L \leq 3N/2$ where N is the number of data points. As for M, the ceiling value depends on (11) where σ_{max} is the maximum singular value found in matrix $\sum$ [8]:

$$\frac{\sigma_c}{\sigma_{max}} \approx 10^{-p} , \qquad (11)$$

where σ_c is another singular value entry down the matrix and p is the number of significant figures of the collected data. The equation states that the singular value that is p orders lower than the maximum singular value is the last pole that needs to be considered [8]. The rest of the poles having lower singular values are considered as noise.

For perfect electric conductors (PEC) structures, a minimal value of M is sufficient to reconstruct the signal within a high accuracy [11]. The value of L = 50 was fixed throughout the analysis.

III. NUMERICAL METHODOLOGY

A. Free space reference configuration

A perfect electric conductor, PEC, pipe is used. The pipe types used in this work are only metallic which are very common in the fuel transport industry like iron cast and steel pipes. Pipes made of dielectrics require further investigation. The length of the pipe is 50 cm, has a diameter of 2.5 cm and a thickness of 0.5 cm. In practical settings the length of the pipe could be in kilometres. However, as a proof of concept the size is limited to 50 cm or less due to the excessive CPU time required by the solver to sweep over the frequency range. For example, the described configurations required ~4 days on an AMD Opteron 246 having four 2 GHz processors. Parallel implementation could solve this issue. Two crack sizes were considered, one having an arc length of 6 cm and the other having an arc length of 4 cm. Cracks are placed at the center of the pipe as shown in Fig. 1. The pipe is excited using a plane wave source with the electric field $\hat{E}_x$ parallel to the axis of the pipe and perpendicular to the crack as shown in Fig. 1. As known, the polarization plays an important factor in picking up the crack signature. The model is solved in the frequency range 50 MHz – 10 GHz at a frequency step of 12.5 MHz. The observation point is located at (0, 0, 60 cm) above the midpoint of the pipe's surface, which is the origin as shown in Fig. 1.

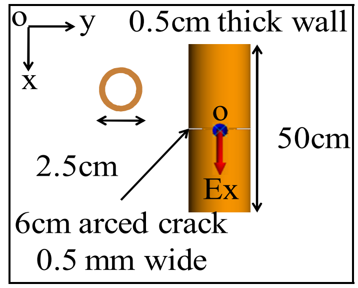

Fig. 1. Pipe configuration and dimensions.

The scattered far field shown in Fig. 2 demonstrates three different cases.

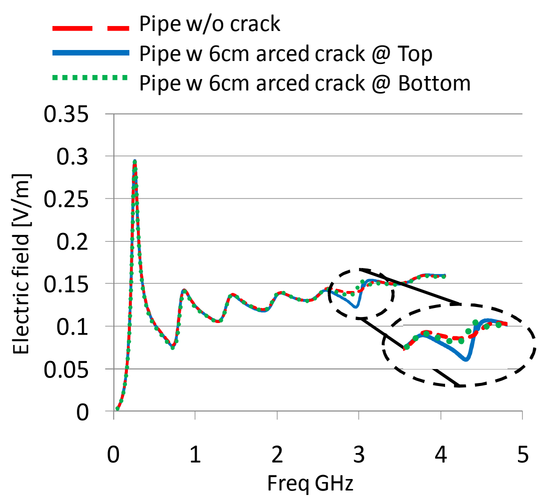

Fig. 2. Scattered fields for pipe in free space.

The dashed line is for a case where a pipe has no cracks. The first resonance of the pipe structure appears as a peak at 260 MHz. The reference resonance of the pipe without a crack stays almost the same when a crack is present due to the miniature size of the crack relative to the pipe. The solid line is the scattered field of the same pipe but with the 6 cm arced crack. The resonance of the pipe appears at 260 MHz and an extra dip appears at 3GHz which is associated with the crack (see the inset). The third case is for the 6 cm arced crack but placed at the bottom side of the pipe, i.e.

on the other side from the illumination source. The dotted line seems to show a small perturbation also at 3 GHz. However, by solely examining the scattered field, no confirmation can be made as to whether a crack exists at the bottom of the pipe or not.

Once the scattered field is collected, a Gaussian filter is applied in order to limit the bandwidth [12] and attenuate residual values of artificial single poles at 0 GHz and 10 GHz. The profile of the filter is shown in Fig. 3.

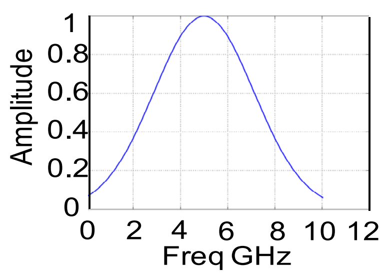

Fig. 3. Gaussian filter profile.

The time domain of the filtered field is obtained using the Fourier transform. The overall time response in Fig. 4a shows a peak at time t=2 ns. This is the time required by the scattered field to propagate from the pipe to the observation point 60 cm away. The matrix pencil method [7-13] is performed on the late time window of the time domain response shown in Fig. 4b. Using the late time response assures removing the illumination effects and makes sure the entire pipe is excited [14].

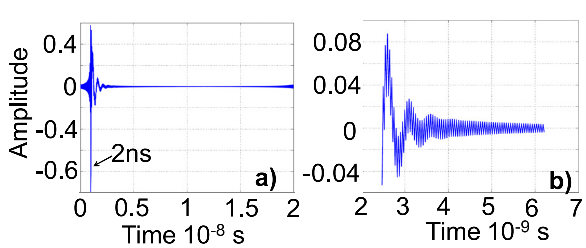

Fig. 4. a) Overall time domain response, b) late time window.

The output of the matrix pencil method is shown in the pole plot of Fig. 5. Only the poles with dominant residues are considered for the three different cases shown in Fig. 2. Consistent with the results of Fig. 2, the resonance of the reference pipe (no cracks) is shown at the pole marked at 260 MHz, which has a dominant residue. The matrix is truncated at M = 4. The pole is indicated by a plus sign in Fig. 5. On the other hand at M = 4, the resonance of the pipe doesn't appear for the case where there was a crack on top or on bottom. Their M was incremented to a value of M = 8 till the main resonance of the reference pipe was extracted. At this value of M, the most dominant pole (largest residue R) appears at a frequency of 2.9 GHz. The 260 MHz reference pole appeared with a significant residue but not the dominant. This signifies the existence of a crack in the pipe. The poles marked with squares and circles in Fig. 5 represent the cases of a crack on the top and on the bottom of the pipe, respectively. Note here that even when a crack was hidden at the bottom of the pipe, a pole associated with the crack appeared as a dominant pole. This was not the case in the far field plot in Fig. 2. This observation confirms that a crack exists in the pipe and shows one of the strengths of the algorithm.

The 4.0 cm arced crack is also introduced at the top of the pipe. A comparison of the scattered field for the pipe is shown in Fig. 6 for the cases with and without the crack. The resonance associated with the crack appears at 6.6 GHz. It was expected that the resonance shifts to a higher frequency compared to the 6.0 cm arced crack since its dimension is smaller.

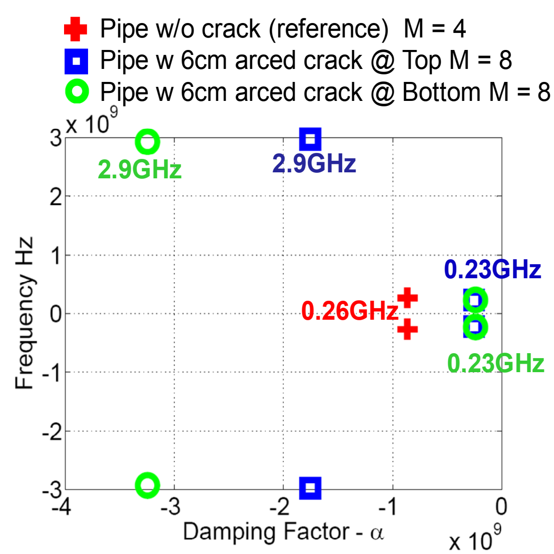

Fig. 5. Pole comparison for reference pipe with no cracks vs. same pipe with 6.0 cm arced crack.

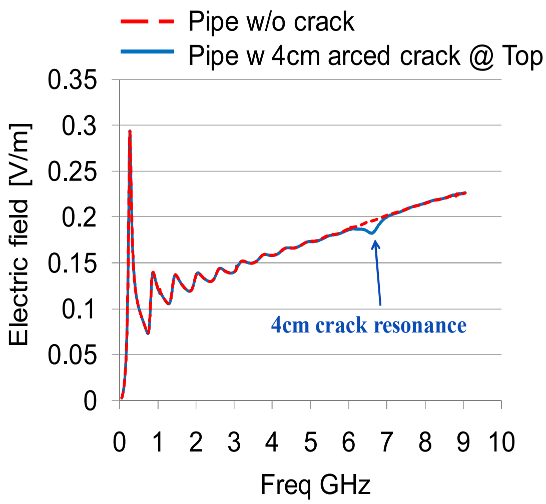

Fig. 6. Scattered field for pipe with a 4.0 cm crack.

The poles of Fig. 6 are plotted in Fig. 7. The algorithm was successful in extracting the reference poles marked as + and the pole associated with a crack marked as a square.

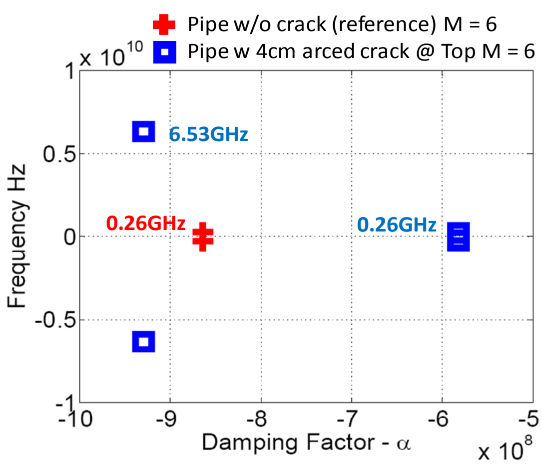

Fig. 7. Pole plot for the reference pipe with and without the 4.0 cm arced crack.

B. Pipe hidden behind plywood

Another case was for a pipe hidden behind a 10.0 cm plywood wall that was infinite in the x-y plane as shown in Fig. 8.

The pipe is located at 5.0 cm away from the wall. Plywood has ε_r = 1.9 and a loss tangent (tanδ) = 0.027. The field is calculated at 60 cm away from the pipe with the origin at the midpoint of the pipe. The illumination was positioned on the opposite side of the pipe.

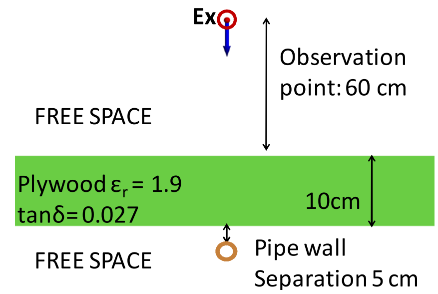

Fig. 8. The configuration of hidden pipe behind plywood wall.

The scattered fields of four scenarios are shown in Fig. 9. The two upper plots of solid and dashed lines represent the pipe in free space without a crack and with a 6.0 cm arced crack, respectively. The bottom two curves are the scattered fields of the hidden pipe with and without the crack. The dotted line is for the pipe with no crack, and the short dashed line is for the same pipe but with the 6.0 cm crack. The magnitude of the scattered field shows attenuation for the hidden case due to the effect of the plywood wall compared with that of free space. However, the scattered fields show that the locations of the resonances are almost the same at 200.0 MHz for the reference pipe and at 3.0 GHz for the hidden pipe with the 6.0 cm crack.

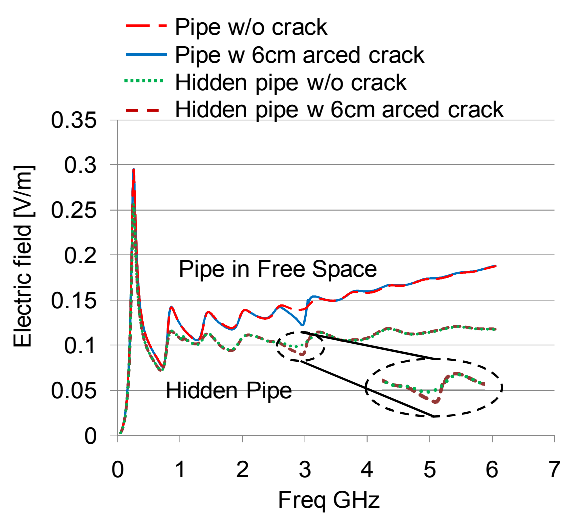

Fig. 9. Comparison of scattered field for pipe in free space vs. pipe hidden behind plywood.

The extracted poles of only the hidden pipe cases are plotted in Fig. 10. Note that the truncation number M is 4 and 10 for the pipe without the crack and with the crack, respectively.

Another common case is for a pipe totally immersed in the plywood wall. The pipe is located at 7.5 cm away from the surface of the plywood interface. The field was computed at the same point as the previous example in Fig. 8. The lower two curves in Fig. 11, where one is dotted and the other is short-dashed, are for an immersed pipe without a crack and a pipe with a crack, respectively. As anticipated, the scattered fields show a shift in the resonance frequency compared with the free space fields due to the contrast between the medium surrounding the pipe in this case.

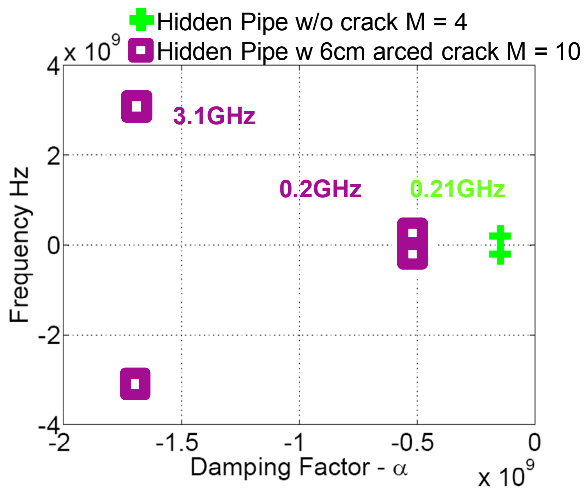

Fig. 10. Pole plot of the hidden pipe with and without the 6cm crack.

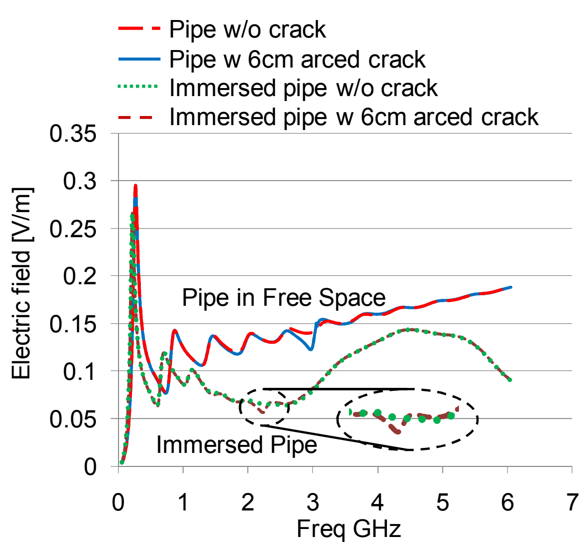

Fig. 11. Comparison of scattered field for the pipe immersed in plywood vs. free space.

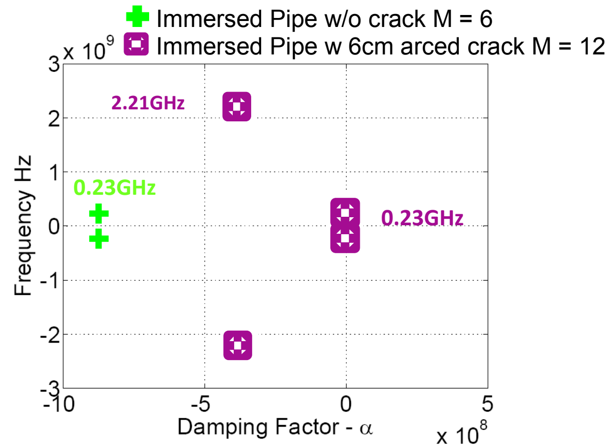

Fig. 12. Pole comparison for immersed pipe cases.

The extracted poles only for the immersed cases are shown in Fig. 12. The reference poles appeared at a frequency of 230 MHz; whereas, the crack pole appeared at a frequency of 2.21 GHz. The pole technique was again successful in detecting the crack in the pipe.

C. Pipe buried underneath sand

A practical case of interest is for a pipe buried underneath sand. The pipe is placed 7.5 cm below the surface of a semi infinite sand plane as shown in Fig. 13. Dry sand has a dielectric constant ε_r = 2.549 and a loss tangent of tanδ = 0.005. Again, the field is calculated at 60 cm away from the pipe with the origin at the midpoint of the pipe as shown in Fig. 1.

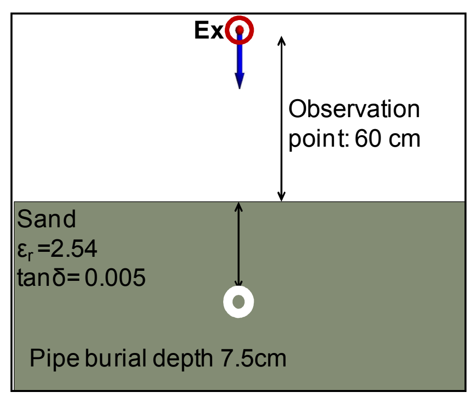

Fig. 13. Configuration of the pipe buried underneath sand.

The four curves in Fig. 14 compare the scattered fields of the buried pipe with that in free space. The lower two curves represent the buried cases for a pipe without a crack in dotted lines and a pipe with a crack in short dashed lines. The scattered fields show a shift in the position of the resonances due to the medium contrast. The extracted poles show the extra resonance at 1.84 GHz which is associated with the presence of the crack as shown in Fig. 15 marked by a square.

D. Pole extraction using noisy data

The synthetic data obtained using FEKO simulations for the pipe in free space was corrupted with random Gaussian noise with signal to noise ratio SNR = 10dB. The pole plot in Fig. 16 shows that, the pipe with no crack and with the 6 cm crack, the reference poles were extracted at 280 MHz and 220 MHz, respectively.

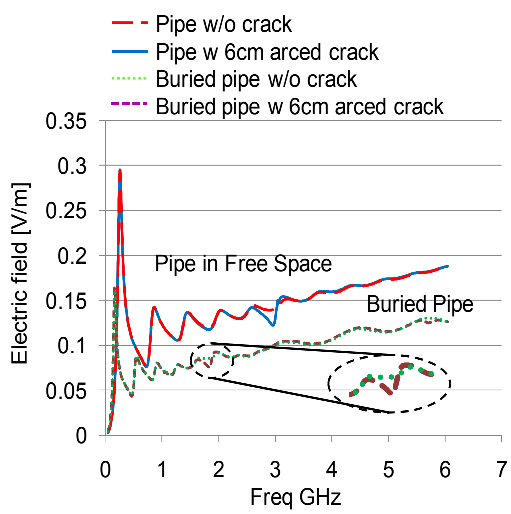

Fig. 14. Comparison of scattered field for pipe in free space vs. pipe immersed in plywood.

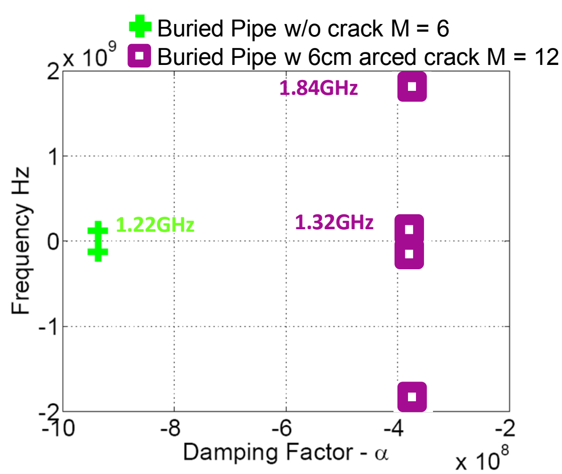

Fig. 15. Pole comparison for immersed pipe cases.

The presence of the noise has caused the reference resonance to shift from 260 MHz for the case of pipe immersed in free space shown in Fig. 2 and in Fig. 5. As well for the case of a pipe with a crack, a dominant pole at 3.24 GHz was extracted as shown in Fig. 16. This shows that the crack detection was successful even with SNR of 10 dB.

As expected, when the SNR is decreased, the pole extraction of the cracks is degraded.

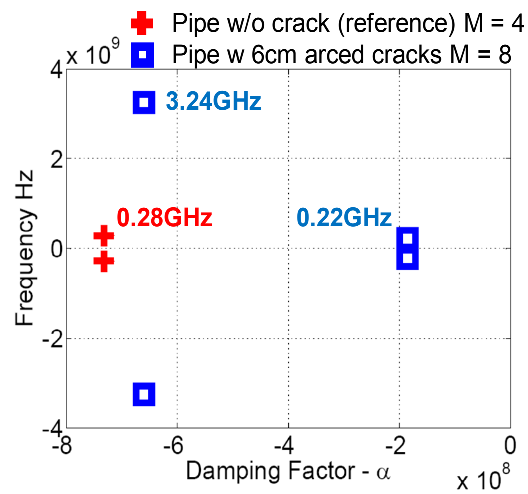

Fig. 16. Poles of the pipe immersed in free space using noisy data of SNR = 10dB.

E. Pole extraction algorithm

The pole extraction algorithm is shown in Fig. 17. Testing the algorithm on buried pipes at larger burial depth with rough interfaces is important for the practical scenario of buried pipes. However, using FEKO, the required CPU time to sweep over the frequency in steps of 12.5MHz was excessive. It is anticipated that the clutter due to the rough surface interface, the attenuation of the soil background, and the larger burial depth of the pipe will affect the sensitivity of the pole extraction. However, the current work has proven the concept of the method in detecting the cracks.

Experiments were conducted inside a custom made $1m^3$ anechoic chamber [15] in order to verify the numerical results. Two Vivaldi antennas, operating between 3 GHz – 10 GHz, were used as transmitters and receivers. The maximum separation distance that can be achieved inside the chamber between the pipe and Vivaldi antennas was 40 cm. The measured SNR was below -5 dB. The transmitted power was -50 dB [16]. Due to these challenges, the extracted poles were erroneous and resulted in random poles that were at frequencies at least 500 MHz higher than the numerical poles. The experimental work needs a larger chamber to assure far field measurements away from absorbing walls of the small chamber in [16]. Also, a power amplifier is needed to increase the transmitted power. More work will be conducted to validate the algorithm on real data.

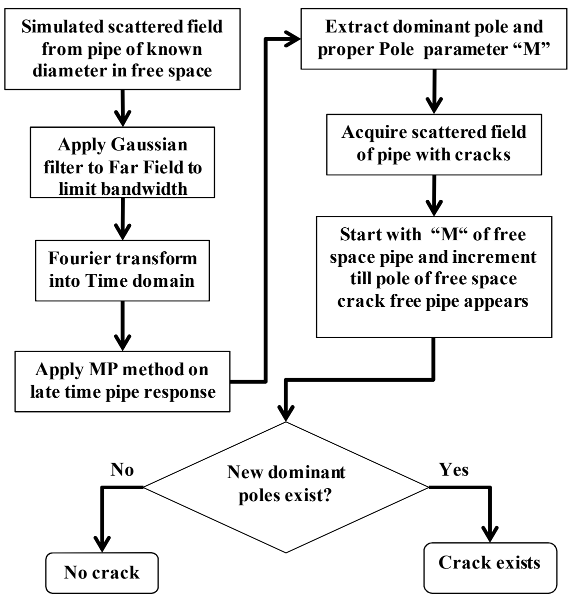

Fig. 17. Pole extraction algorithm.

For a periodically slotted cylinder, the length of the slot is half the wavelength of the resonant frequency [18]. In this work, the length of the crack was observed to be close to half wavelength or multiples as shown in Table 1. Other different lengths of the crack were, also, considered but not included in this work.

Table 1: Crack length versus resonance frequency

Crack lengths (cm)	Resonance frequency (GHz)	Wavelengths of resonance (cm)
6	3.1	9.7
4	6.7	4.5
2	12.7	2.36

IV. CONCLUSION

The numerical algorithm presented here was successful in employing the matrix pencil method for crack detection on the surface of metallic pipes. The algorithm showed success even when noisy data up to SNR of 10 dB was processed for a pipe in free space. However, when the SNR was below 10dB, the extracted poles took random non-resilient values. The susceptibility to noise can be improved by possibly substituting the total least square method by a more noise tolerant approach such as the minimum mean square error [17]. It is possible to integrate the current algorithm with an *inverse scattering algorithm* [15]. This will serve to extract the host's electrical parameters simultaneously with detecting and reconstructing the crack's shape. This is an interesting future research topic.

ACKNOWLEDGMENT

This work was funded by Entergy Incorporation. Special thanks to Electromagnetic Software and Systems Inc. (EMSS USA http://www.emssusa.com) for their technical support and special pricing for FEKO Gold license.

REFERENCES

[1] S. Eyuboglu, H. Mahdi, and H. Al-Shukri, "Detection of water leak using ground penetrating radar," Central Arkansas Water, Little Rock, Arkansas, 2004.

[2] O. Duran, K. Althoefer, and L. D. Seneviratne, "Automated pipe defect detection and categorization using camera/laser-based profiler and artificial neural network," *IEEE Trans. on Automation Science and Engineering,* vol. 4, no. 1, pp. 118-126, January 2007.

[3] Electric Power Research Institute, http://www.epri.com.

[4] M. Silk and K. Bainton, "The propagation in metal tubing of ultrasonic wave modes equivalent to Lamb waves," *Ultrasonics,* vol. 17, no. 1, pp. 11–19, January 1979.

[5] P. Gamba and S. Lossani, "Neural detection of pipe signatures in ground penetrating radar," *IEEE Trans. on Geoscience and Remote Sensing,* vol. 38, no. 2, pp. 790-797, March 2000.

[6] FEKO Field Computations Involving Objects or Arbitrary Shape, http://www.feko.info.

[7] Y. Hua and T. K. Sarkar, "Matrix pencil method for estimating parameters of exponentially damped/undamped sinusoids in noise," *IEEE*

Trans. Acoustic Speech and Signal Processing, vol. 38, no. 5, pp. 814-824, May 1990.
[8] O. M. Pereira-Filho and T. K. Sarkar, "Using the matrix pencil method to estimate the parameters by a sum of complex exponentials," *IEEE Antennas Propagation Magazine*, vol. 37, no. 1, pp. 48–55, February 1995.
[9] Y. Hua and T. K. Sarkar, "Generalized pencil-of-functions method for extracting the poles of an extracting the poles of an electromagnetic system from its transient response," *IEEE Trans. on Antennas Propagation,* vol. 37, no. 2, pp. 229–234, February 1989.
[10] A. T. Blischak and M. Manteghi, "Pole residue techniques for chipless RFID detection," *International Symposium on Antennas and Propagation,* Charleston, SC, pp. 1 - 4, June 2009.
[11] L. Marin and R.W. Latham, "Representation of transient scattered fields in terms of free oscillations of bodies," *Proceedings in IEEE,* vol. 60, no. 5, pp. 640 - 641, May 1972.
[12] R. S. Adve, T. K. Sarkar, O. Maroja, C. Pereira-Filho, and S. M. Rao, "Extrapolation of time-domain responses from three-dimensional conducting objects utilizing the matrix pencil technique," *IEEE Trans. on Antennas and Propagation*, vol. 45, no. 1, pp. 147-156, January 1997.
[13] Y. Hua and T. K. Sarkar, "Matrix pencil and system poles," *Signal Processing,* vol. 21, no. 2, pp. 195-198, October 1990.
[14] J. Chauveau, N. Beaucoudrey, and J. Saillard, "Characterization of perfectly conducting targets in resonance domain with their quality of resonance," *Progress In Electromagnetics Research,* vol. 74, pp. 69–84, 2007.
[15] D. A. Woten, M. R. Hajihashemi, A. M. Hassan, and Magda El-Shenawee, "Experimental microwave validation of level set reconstruction algorithm," *IEEE Trans. on Antennas and Propagation,* vol. 58, no. 1, pp. 230-233, January 2010.
[16] F. Deek, "Microwave detection of cracks in buried pipes using the complex frequency technique," M.S. Thesis, Eleg, U of A, Fayetteville, AR, 2010.
[17] D. Guo, S. Shamai, and S. Verdu, "Estimation of non-Gaussian random variables in Gaussian noise: properties of the MMSE," *International Symposium on Information Theory,* Toronto, Canada, July 6-11, pp. 1083-1087, 2008.
[18] M. Mokhtar, "Analysis of cylindrical frequency selective surfaces," *Proc. of Radio Science Conference,* Helwan, Egypt, pp. B8/1 – B8/8, February 1998.

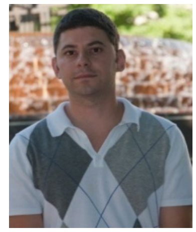

Fadi Deek received his B.S. in Computer and Communications with honors from the American University of Science and Technology, Beirut, Lebanon in 2005. He then worked for three years as an electronic engineer at Fidus Systems. In 2010, he received his M.S. degree in Electrical Engineering from the University of Arkansas, Fayetteville, Arkansas.

Dr. Magda El–Shenawee Dr. El-Shenawee is a Senior member of IEEE since 2002. She received the B.S. and M.S. degrees in electrical engineering from Assiut University, Assiut, Egypt, and the Ph.D. degree in electrical engineering from the University of Nebraska-Lincoln in 1991. In 1992, she worked as a Research Associate in the Center for Electro-Optics at the University of Nebraska where she focused on the problem of enhanced backscatter phenomena. In 1994, she worked as a Research Associate at the National Research Center, Cairo, Egypt, and in 1997, she worked as Visiting Scholar at the University of Illinois at Urbana-Champaign. In 1999, she joined the Multidisciplinary University Research Initiative (MURI) team at Northeastern University, Boston, MA. Dr. El-Shenawee is a member of Eta Kappa Nu electrical engineering honor society.

Currently, Dr. El-Shenawee is a Professor in the Department of Electrical Engineering at the University of Arkansas. Research interests include: biomedical engineering, breast cancer imaging (modeling, detection and treatment), microwave imaging algorithms, anti-personnel mine detection modeling and algorithms, rough surface scattering, subsurface sensing of buried objects, computational electromagnetics, and RF and microwave circuits.

2010 INSTITUTIONAL MEMBERS

DTIC-OCP LIBRARY
8725 John J. Kingman Rd, Ste 0944
Fort Belvoir, VA 22060-6218

AUSTRALIAN DEFENCE LIBRARY
Northcott Drive
Canberra, A.C.T. 2600 Australia

BEIJING BOOK CO, INC
701 E Linden Avenue
Linden, NJ 07036-2495

BUCKNELL UNIVERSITY
69 Coleman Hall Road
Lewisburg, PA 17837

ROBERT J. BURKHOLDER
OHIO STATE UNIVERSITY
1320 Kinnear Road
Columbus, OH 43212

DARTMOUTH COLLEGE
6025 Baker/Berry Library
Hanover, NH 03755-3560

DSTO EDINBURGH
AU/33851-AP, PO Box 830470
Birmingham, AL 35283

SIMEON J. EARL – BAE SYSTEMS
W432A, Warton Aerodome
Preston, Lancs., UK PR4 1AX

ELLEDIEMME
Libri Dal Mondo
PO Box 69/Poste S. Silvestro
Rome, Italy 00187

ENGINEERING INFORMATION, INC
PO Box 543
Amsterdam, Netherlands 1000 Am

ETSE TELECOMUNICACION
Biblioteca, Campus Lagoas
Vigo, 36200 Spain

OLA FORSLUND
SAAB MICROWAVE SYSTEMS
Nettovagen 6
Jarfalla, Sweden SE-17588

GEORGIA TECH LIBRARY
225 North Avenue, NW
Atlanta, GA 30332-0001

HRL LABS, RESEARCH LIBRARY
3011 Malibu Canyon
Malibu, CA 90265

IEE INSPEC
Michael Faraday House
6 Hills Way
Stevenage, Herts UK SG1 2AY

IND CANTABRIA
PO Box 830470
Birmingham, AL 35283

INSTITUTE FOR SCIENTIFIC INFO.
Publication Processing Dept.
3501 Market St.
Philadelphia, PA 19104-3302

KUWAIT UNIVERSITY
Postfach/po box 432
Basel, Switzerland 4900

LIBRARY – DRDC OTTAWA
3701 Carling Avenue
Ottawa, Ontario, Canada K1A OZ4

LIBRARY of CONGRESS
Reg. Of Copyrights
Attn: 407 Deposits
Washington DC, 20559

LINDA HALL LIBRARY
5109 Cherry Street
Kansas City, MO 64110-2498

RAY MCKENZIE – TELESTRA
13/242 Exhibition Street
Melbourne, Vic, Australia 3000

MISSISSIPPI STATE UNIV LIBRARY
PO Box 9570
Mississippi State, MS 39762

MISSOURI S&T
400 W 14th Street
Rolla, MO 56409

MIT LINCOLN LABORATORY
Periodicals Library
244 Wood Street
Lexington, MA 02420

OSAMA MOHAMMED
FLORIDA INTERNATIONAL UNIV
10555 W Flagler Street
Miami, FL 33174

NAVAL POSTGRADUATE SCHOOL
Attn:J. Rozdal/411 Dyer Rd./ Rm 111
Monterey, CA 93943-5101

NDL KAGAKU
C/0 KWE-ACCESS
PO Box 300613 (JFK A/P)
Jamaica, NY 11430-0613

OVIEDO LIBRARY
PO BOX 830679
Birmingham, AL 35283

PENN STATE UNIVERSITY
126 Paterno Library
University Park, PA 16802-1808

DAVID J. PINION
1122 E PIKE STREET #1217
SEATTLE, WA 98122

KATHERINE SIAKAVARA-
ARISTOTLE UNIV OF
THESSALONIKI
Gymnasiou 8
Thessaloniki, Greece 55236

SWETS INFORMATION SERVICES
160 Ninth Avenue, Suite A
Runnemede, NJ 08078

TIB & UNIV. BIB. HANNOVER
DE/5100/G1/0001
Welfengarten 1B
Hannover, Germany 30167

UNIV OF CENTRAL FLORIDA
4000 Central Florida Boulevard
Orlando, FL 32816-8005

UNIVERSITY OF COLORADO
1720 Pleasant Street, 184 UCB
Boulder, CO 80309-0184

UNIVERSITY OF KANSAS –
WATSON
1425 Jayhawk Blvd 210S
Lawrence, KS 66045-7594

UNIVERSITY OF MISSISSIPPI
JD Williams Library
University, MS 38677-1848

UNIVERSITY LIBRARY/HKUST
CLEAR WATER BAY ROAD
KOWLOON, HONG KONG

UNIV POLIT CARTAGENA
Serv Btca Univ,
Paseo Alfonso XIII, 48
Cartagena, Spain 30203

THOMAS WEILAND
TU DARMSTADT
Schlossgartenstrasse 8
Darmstadt, Hessen, Germany 64289

STEVEN WEISS
US ARMY RESEARCH LAB
2800 Powder Mill Road
Adelphi, MD 20783

YOSHIHIDE YAMADA
NATIONAL DEFENSE ACADEMY
1-10-20 Hashirimizu
Yokosuka, Kanagawa,
Japan 239-8686

ACES COPYRIGHT FORM

This form is intended for original, previously unpublished manuscripts submitted to ACES periodicals and conference publications. The signed form, appropriately completed, MUST ACCOMPANY any paper in order to be published by ACES. PLEASE READ REVERSE SIDE OF THIS FORM FOR FURTHER DETAILS.

TITLE OF PAPER:

AUTHORS(S)

PUBLICATION TITLE/DATE:

RETURN FORM TO:

Dr. Atef Z. Elsherbeni
University of Mississippi
Dept. of Electrical Engineering
Anderson Hall Box 13
University, MS 38677 USA

PART A - COPYRIGHT TRANSFER FORM

(NOTE: Company or other forms may not be substituted for this form. U.S. Government employees whose work is not subject to copyright may so certify by signing Part B below. Authors whose work is subject to Crown Copyright may sign Part C overleaf).

The undersigned, desiring to publish the above paper in a publication of ACES, hereby transfer their copyrights in the above paper to The Applied Computational Electromagnetics Society (ACES). The undersigned hereby represents and warrants that the paper is original and that he/she is the author of the paper or otherwise has the power and authority to make and execute this assignment.

Returned Rights: In return for these rights, ACES hereby grants to the above authors, and the employers for whom the work was performed, royalty-free permission to:

1. Retain all proprietary rights other than copyright, such as patent rights.
2. Reuse all or portions of the above paper in other works.
3. Reproduce, or have reproduced, the above paper for the author's personal use or for internal company use provided that (a) the source and ACES copyright are indicated, (b) the copies are not used in a way that implies ACES endorsement of a product or service of an employer, and (c) the copies per se are not offered for sale.
4. Make limited distribution of all or portions of the above paper prior to publication.
5. In the case of work performed under U.S. Government contract, ACES grants the U.S. Government royalty-free permission to reproduce all or portions of the above paper, and to authorize others to do so, for U.S. Government purposes only.

ACES Obligations: In exercising its rights under copyright, ACES will make all reasonable efforts to act in the interests of the authors and employers as well as in its own interest. In particular, ACES REQUIRES that:

1. The consent of the first-named author be sought as a condition in granting re-publication permission to others.
2. The consent of the undersigned employer be obtained as a condition in granting permission to others to reuse all or portions of the paper for promotion or marketing purposes.

In the event the above paper is not accepted and published by ACES or is withdrawn by the author(s) before acceptance by ACES, this agreement becomes null and void.

AUTHORIZED SIGNATURE | TITLE (IF NOT AUTHOR)

EMPLOYER FOR WHOM WORK WAS PERFORMED | DATE FORM SIGNED

Part B - U.S. GOVERNMENT EMPLOYEE CERTIFICATION

(NOTE: if your work was performed under Government contract but you are not a Government employee, sign transfer form above and see item 5 under Returned Rights).

This certifies that all authors of the above paper are employees of the U.S. Government and performed this work as part of their employment and that the paper is therefor not subject to U.S. copyright protection.

AUTHORIZED SIGNATURE | TITLE (IF NOT AUTHOR)

NAME OF GOVERNMENT ORGANIZATION | DATE FORM SIGNED

PART C - CROWN COPYRIGHT

(NOTE: ACES recognizes and will honor Crown Copyright as it does U.S. Copyright. It is understood that, in asserting Crown Copyright, ACES in no way diminishes its rights as publisher. Sign only if *ALL* authors are subject to Crown Copyright).

This certifies that all authors of the above Paper are subject to Crown Copyright. (Appropriate documentation and instructions regarding form of Crown Copyright notice may be attached).

AUTHORIZED SIGNATURE TITLE OF SIGNEE

NAME OF GOVERNMENT BRANCH DATE FORM SIGNED

Information to Authors

ACES POLICY

ACES distributes its technical publications throughout the world, and it may be necessary to translate and abstract its publications, and articles contained therein, for inclusion in various compendiums and similar publications, etc. When an article is submitted for publication by ACES, acceptance of the article implies that ACES has the rights to do all of the things it normally does with such an article.

In connection with its publishing activities, it is the policy of ACES to own the copyrights in its technical publications, and to the contributions contained therein, in order to protect the interests of ACES, its authors and their employers, and at the same time to facilitate the appropriate re-use of this material by others.

The new United States copyright law requires that the transfer of copyrights in each contribution from the author to ACES be confirmed in writing. It is therefore necessary that you execute either Part A-Copyright Transfer Form or Part B-U.S. Government Employee Certification or Part C-Crown Copyright on this sheet and return it to the Managing Editor (or person who supplied this sheet) as promptly as possible.

CLEARANCE OF PAPERS

ACES must of necessity assume that materials presented at its meetings or submitted to its publications is properly available for general dissemination to the audiences these activities are organized to serve. It is the responsibility of the authors, not ACES, to determine whether disclosure of their material requires the prior consent of other parties and if so, to obtain it. Furthermore, ACES must assume that, if an author uses within his/her article previously published and/or copyrighted material that permission has been obtained for such use and that any required credit lines, copyright notices, etc. are duly noted.

AUTHOR/COMPANY RIGHTS

If you are employed and you prepared your paper as a part of your job, the rights to your paper initially rest with your employer. In that case, when you sign the copyright form, we assume you are authorized to do so by your employer and that your employer has consented to all of the terms and conditions of this form. If not, it should be signed by someone so authorized.

NOTE RE RETURNED RIGHTS: Just as ACES now requires a signed copyright transfer form in order to do "business as usual", it is the intent of this form to return rights to the author and employer so that they too may do "business as usual". If further clarification is required, please contact: The Managing Editor, R. W. Adler, Naval Postgraduate School, Code EC/AB, Monterey, CA, 93943, USA (408)656-2352.

Please note that, although authors are permitted to re-use all or portions of their ACES copyrighted material in other works, this does not include granting third party requests for reprinting, republishing, or other types of re-use.

JOINT AUTHORSHIP

For jointly authored papers, only one signature is required, but we assume all authors have been advised and have consented to the terms of this form.

U.S. GOVERNMENT EMPLOYEES

Authors who are U.S. Government employees are not required to sign the Copyright Transfer Form (Part A), but any co-authors outside the Government are.

Part B of the form is to be used instead of Part A only if all authors are U.S. Government employees and prepared the paper as part of their job.

NOTE RE GOVERNMENT CONTRACT WORK: Authors whose work was performed under a U.S. Government contract but who are not Government employees are required so sign Part A-Copyright Transfer Form. However, item 5 of the form returns reproduction rights to the U. S. Government when required, even though ACES copyright policy is in effect with respect to the reuse of material by the general public.

January 2002

APPLIED COMPUTATIONAL ELECTROMAGNETICS SOCIETY JOURNAL
http://aces.ee.olemiss.edu

INFORMATION FOR AUTHORS

PUBLICATION CRITERIA

Each paper is required to manifest some relation to applied computational electromagnetics. **Papers may address general issues in applied computational electromagnetics, or they may focus on specific applications, techniques, codes, or computational issues.** While the following list is not exhaustive, each paper will generally relate to at least one of these areas:

1. **Code validation.** This is done using internal checks or experimental, analytical or other computational data. Measured data of potential utility to code validation efforts will also be considered for publication.

2. **Code performance analysis.** This usually involves identification of numerical accuracy or other limitations, solution convergence, numerical and physical modeling error, and parameter tradeoffs. However, it is also permissible to address issues such as ease-of-use, set-up time, run time, special outputs, or other special features.

3. **Computational studies of basic physics.** This involves using a code, algorithm, or computational technique to simulate reality in such a way that better, or new physical insight or understanding, is achieved.

4. **New computational techniques** or new applications for existing computational techniques or codes.

5. **"Tricks of the trade"** in selecting and applying codes and techniques.

6. **New codes, algorithms, code enhancement, and code fixes.** This category is self-explanatory, but includes significant changes to existing codes, such as applicability extensions, algorithm optimization, problem correction, limitation removal, or other performance improvement. **Note: Code (or algorithm) capability descriptions are not acceptable, unless they contain sufficient technical material to justify consideration.**

7. **Code input/output issues.** This normally involves innovations in input (such as input geometry standardization, automatic mesh generation, or computer-aided design) or in output (whether it be tabular, graphical, statistical, Fourier-transformed, or otherwise signal-processed). Material dealing with input/output database management, output interpretation, or other input/output issues will also be considered for publication.

8. **Computer hardware issues.** This is the category for analysis of hardware capabilities and limitations of various types of electromagnetics computational requirements. Vector and parallel computational techniques and implementation are of particular interest.

Applications of interest include, but are not limited to, antennas (and their electromagnetic environments), networks, static fields, radar cross section, inverse scattering, shielding, radiation hazards, biological effects, biomedical applications, electromagnetic pulse (EMP), electromagnetic interference (EMI), electromagnetic compatibility (EMC), power transmission, charge transport, dielectric, magnetic and nonlinear materials, microwave components, MEMS, RFID, and MMIC technologies, remote sensing and geometrical and physical optics, radar and communications systems, sensors, fiber optics, plasmas, particle accelerators, generators and motors, electromagnetic wave propagation, non-destructive evaluation, eddy currents, and inverse scattering.

Techniques of interest include but not limited to frequency-domain and time-domain techniques, integral equation and differential equation techniques, diffraction theories, physical and geometrical optics, method of moments, finite differences and finite element techniques, transmission line method, modal expansions, perturbation methods, and hybrid methods.

Where possible and appropriate, authors are required to provide statements of quantitative accuracy for measured and/or computed data. This issue is discussed in "Accuracy & Publication: Requiring, quantitative accuracy statements to accompany data," by E. K. Miller, *ACES Newsletter,* Vol. 9, No. 3, pp. 23-29, 1994, ISBN 1056-9170.

SUBMITTAL PROCEDURE

All submissions should be uploaded to ACES server through ACES web site (http://aces.ee.olemiss.edu) by using the upload button, journal section. Only pdf files are accepted for submission. The file size should not be larger than 5MB, otherwise permission from the Editor-in-Chief should be obtained first. Automated acknowledgment of the electronic submission, after the upload process is successfully completed, will be sent to the corresponding author only. It is the responsibility of the corresponding author to keep the remaining authors, if applicable, informed. Email submission is not accepted and will not be processed.

PAPER FORMAT (INITIAL SUBMISSION)

The preferred format for initial submission manuscripts is 12 point Times Roman font, single line spacing and single column format, with 1 inch for top, bottom, left, and right margins. Manuscripts should be prepared for standard 8.5x11 inch paper.

EDITORIAL REVIEW

In order to ensure an appropriate level of quality control, papers are peer reviewed. They are reviewed both for technical correctness and for adherence to the listed guidelines regarding information content and format.

PAPER FORMAT (FINAL SUBMISSION)

Only camera-ready electronic files are accepted for publication. The term **"camera-ready" means that the material is neat, legible, reproducible, and in accordance with the final version format listed below.**

The following requirements are in effect for the final version of an ACES Journal paper:

1. The paper title should not be placed on a separate page. The title, author(s), abstract, and (space permitting) beginning of the paper itself should all be on the first page. The title, author(s), and author affiliations should be centered (center-justified) on the first page. The title should be of font size 16 and bolded, the author names should be of font size 12 and bolded, and the author affiliation should be of font size 12 (regular font, neither italic nor bolded).

2. An abstract is required. The abstract should be a brief summary of the work described in the paper. It should state the computer codes, computational techniques, and applications discussed in the paper (as applicable) and should otherwise be usable by technical abstracting and indexing services. The word "Abstract" has to be placed at the left margin of the paper, and should be bolded and italic. It also should be followed by a hyphen (—) with the main text of the abstract starting on the same line.

3. All section titles have to be centered and all the title letters should be written in caps. The section titles need to be numbered using roman numbering (I. II. ….)

4. Either British English or American English spellings may be used, provided that each word is spelled consistently throughout the paper.

5. Internal consistency of references format should be maintained. As a guideline for authors, we recommend that references be given using numerical numbering in the body of the paper (with numerical listing of all references at the end of the paper). The first letter of the authors' first name should be listed followed by a period, which in turn, followed by the authors' complete last name. Use a coma (,) to separate between the authors' names. Titles of papers or articles should be in quotation marks (" "), followed by the title of journal, which should be in italic font. The journal volume (vol.), issue number (no.), page numbering (pp.), month and year of publication should come after the journal title in the sequence listed here.

6. Internal consistency shall also be maintained for other elements of style, such as equation numbering. As a guideline for authors who have no other preference, we suggest that equation numbers be placed in parentheses at the right column margin.

7. The intent and meaning of all text must be clear. For authors who are not masters of the English language, the ACES Editorial Staff will provide assistance with grammar (subject to clarity of intent and meaning). However, this may delay the scheduled publication date.

8. Unused space should be minimized. Sections and subsections should not normally begin on a new page.

ACES reserves the right to edit any uploaded material, however, this is not generally done. It is the author(s) responsibility to provide acceptable camera-ready pdf files. Incompatible or incomplete pdf files will not be processed for publication, and authors will be requested to re-upload a revised acceptable version.

COPYRIGHTS AND RELEASES

Each primary author must sign a copyright form and obtain a release from his/her organization vesting the copyright with ACES. Copyright forms are available at ACES, web site (http://aces.ee.olemiss.edu). To shorten the review process time, the executed copyright form should be forwarded to the Editor-in-Chief immediately after the completion of the upload (electronic submission) process. Both the author and his/her organization are allowed to use the copyrighted material freely for their own private purposes.

Permission is granted to quote short passages and reproduce figures and tables from and ACES Journal issue provided the source is cited. Copies of ACES Journal articles may be made in accordance with usage permitted by Sections 107 or 108 of the U.S. Copyright Law. This consent does not extend to other kinds of copying, such as for general distribution, for advertising or promotional purposes, for creating new collective works, or for resale. The reproduction of multiple copies and the use of articles or extracts for commercial purposes require the consent of the author and specific permission from ACES. Institutional members are allowed to copy any ACES Journal issue for their internal distribution only.

PUBLICATION CHARGES

All authors are allowed for 8 printed pages per paper without charge. Mandatory page charges of $75 a page apply to all pages in excess of 8 printed pages. Authors are entitled to one, free of charge, copy of the journal issue in which their paper was published. Additional reprints are available for a nominal fee by submitting a request to the managing editor or ACES Secretary.

Authors are subject to fill out a one page over-page charge form and submit it online along with the copyright form before publication of their manuscript.

ACES Journal is abstracted in INSPEC, in Engineering Index, DTIC, Science Citation Index Expanded, the Research Alert, and to Current Contents/Engineering, Computing & Technology.